Operational Space and Characterization of a Rotating Detonation Engine Using Hydrogen and Air

THESIS

Presented in Partial Fulfillment of the Requirements for the Degree Master of Science in the Graduate School of The Ohio State University

By

James Alexander Suchocki, B.S.

Graduate Program in Mechanical Engineering

The Ohio State University

2012

Master's Examination Committee:

Dr. Sheng-Tao John Yu, Advisor

Dr. Frederick R. Schauer

Dr. Michael George Dunn

Abstract

An experimental study was performed on a rotating detonation engine originally designed by Pratt and Whitney's Seattle Aerosciences Center. The engine was tested with a hydrogen-air mixture in order to determine the range of operation of the device. After an operating region was found with hydrogen-air, additional oxygen was added to the air in order to expand the engine's range of operability and thrust output. A number of measurements such as the speed of the detonation wave, the steadiness of the detonation wave, the channel pressure, the thrust output, and the fuel and oxidizer mass flows were measured in order to characterize the operation of the engine. In addition to the increased operability with greater oxygen content, the higher oxygen concentration enabled the engine to detonate at high enough air mass flows to contain two detonation waves during operation. The detonation wave activity before, during, and after the transition from one to two detonation waves was analyzed in order to gain a deeper understanding of the transition phenomenon.

Dedication

To my parents, grandparents, and siblings, who have always encouraged and supported me; and to my fiancée, who has been there for me every step of the way.

Acknowledgments

I would like to thank Dr. John Yu who has been an excellent advisor by providing the right advice and asking the right questions to make sure my research went as smoothly as possible. Through the years of my Master's degree, Dr. John Yu has become a trusted friend in addition to being my graduate advisor.

I would also like to thank Dr. John Hoke and Dr. Frederick Schauer at the Detonation Engine Research Facility at Wright-Patterson Air Force Base. Their leadership, advice, and encouragement fostered an environment where I could lean and explore.

I would also like to thank Curtis Rice for answering the endless number of questions I had regarding the operation of the machinery, instrumentation, and control systems in the lab. He was great to work with and laugh with, and always treated me with respect.

Vita

May, 1988 ....Born in Highland Park, Illinois

June, 2006 ....Padua Franciscan High School, Parma, Ohio

June, 2010 ....B.S. Mechanical Engineering, The Ohio State University

2010 to present ....Graduate Research Associate, Department of Mechanical and Aerospace Engineering, The Ohio State University

Fields of Study

Major Field: Mechanical Engineering

Table of Contents

List of Figures

List of Tables

Chapter 1: Introduction

1.1: RDE History

The Rotating Detonation Engine (RDE), which is also known as a Rotary Detonation Engine or Continuous Detonation Engine, is a new engine concept that seeks to harness the power of detonation. Research in RDEs and other detonation concepts has greatly increased in recent years, as is evidenced by the first manned flight of an aircraft powered by a Pulsed-Detonation Engine (PDE) in 2008 (Thomas et al, 2011) and the successful operation of numerous RDEs around the world in the last decade (Kailasanath, 2011).

The RDE was designed to improve upon some of the shortcomings that exist in a PDE. A PDE operates by filling a tube or tubes with a detonable mixture, initiating a detonation in the tube, exhausting the products, then repeating the process. Although PDEs have been operated reliably enough to power manned flight, the PDE still has a number of drawbacks (Schauer, et al. 2001). Two of the drawbacks of the PDE are (i) the detonation must be re-initiated for each cycle, and (ii) the cyclical operation causes the flow downstream of the PDE to be extremely unsteady. The RDE concept eliminates these shortcomings because it only requires one initiation and the downstream flow is much more steady.

An RDE engine operates by flowing a detonable mixture of fuel and air axially into a cylindrical channel, then tangentially exhausting a detonation into the channel to detonate the mixture. The detonation is sustained by the continuous flow of the fuel and air axially into the channel while the detonation propagates circumferentially in the channel. As the detonation runs around the channel, a sufficient amount of fuel and air must refill the channel by the time the detonation returns to the same point in the channel. If the mass flow of fuel and air into the channel is too low, then the detonation will decay into a deflagration or the combustion process will stop completely.

Although an RDE has the aforementioned advantages over a PDE in ignition energy and steady exit flow, these advantages still come with their own drawbacks. The single ignition makes an RDE more efficient than a PDE, but makes the operation more difficult since the energy from a single ignition must be able initiate and propagate a detonation for the entire operating time of the engine, instead of just down a single tube for about a thousandth of a second. The continuous detonation of an RDE makes the downstream flow much more steady than the pulsed flow of a PDE, but causes the engine to rise to extremely high temperatures. This amount of heat can cause damage and destroy engine parts and the instrumentation.

1.2: Research Motivation

Research is being conducted in detonation engines because the thermodynamics of detonation engines promise higher efficiency than engines that utilize deflagration combustion. In detonation combustion, the products of the reaction are at a greater pressure than the reactants, and in deflagration combustion, the products of the reaction are at a slightly lower pressure than the reactants. The pressure gain caused by detonation combustion allows for more work to be extracted from the fuel than what can be extracted from the products of deflagration combustion.

Although the thermodynamics are promising, research must be performed in order to realize the efficiencies promised by detonation theory. The first step in discovering if detonation combustion provides improved efficiency is creating an engine that produces detonations. Therefore, the focus of the beginning of the research conducted on the RDE is finding a condition where the engine produced a continuous detonation. After the RDE can produce a continuous detonation, then a great number of possible research avenues can be pursued. The most logical area to be researched after a continuous detonation has been produced is determining what other oxidizer-fuel combinations produce a continuous detonation. The resulting detonation wave speed, detonation wave steadiness, specific impulse and other characteristics produced by different oxidizer-fuel combinations can be compared and more fully understood by performing these tests.

Another motivation for RDE research is to determine how the extraordinary amount of heat that is produced by detonation combustion effects the engine parts and instrumentation. Heat is a much greater concern in an RDE than a PDE because the PDE has fill and purge periods during which there are no detonations present in any portion of the engine. On the other hand, a detonation is always present in the channel during the entire operation of the RDE because it does not have fill or purge periods. Clever part design, heat-resistant materials and coatings, and a cooling system may all be necessary in order to operate an RDE long enough for the engine to be useful in practical applications.

1.3: Thesis Layout

This thesis is organized into 5 chapters. The first chapter is the introduction, which begins the discussion of rotating detonation engines and the motivation for their study. The second chapter, the background, provides information about detonation combustion and its properties. An explanation of the facility and experimental setup follows in the third chapter. This chapter describes the facility where the research was performed, how the engine that was tested and controlled, and how the data was collected from the tests. The fourth chapter shows what calculations and procedures were performed in order to transform the raw data into meaningful results. The fourth chapter discusses the errors and uncertainties involved in the data collection and reduction. The final chapter presents the results along with what information can be concluded the rotating detonation engine that was tested.

Chapter 2: Background

2.1: Combustion Theory

Combustion reactions are categorized as either a deflagration or a detonation. A deflagration is primarily characterized by subsonic flame propagation and a slight pressure drop from reactants to products. On the other hand, a detonation is primarily characterized by supersonic flame propagation and a pressure increase from reactants to products. These properties, as well as many others, have been determined by theoretical analysis beginning with Chapman and Jouget in the late 19th century (Glassman, 2008).

The analysis of combustion phenomena begins by considering mass, momentum, and energy all to be conserved quantities during the reaction. The equations mathematically describing these conserved quantities are shown in their respective order as Equations (2.1), (2.2), and (2.3). In these equations ρ is the density, u is the velocity, P is the pressure, c_p is the specific heat, T is the temperature, and q is the heat release from the system. The velocities used in these equations are defined in Figure 2.1 (Glassman, 2008).

$$\rho_1 u_1 = \rho_2 u_2 \tag{2.1}$$

$$P_1 + \rho_1 u_1^2 = P_2 + \rho_2 u_2^2 \tag{2.2}$$

$$c_p T_1 + \frac{1}{2} u_1^2 + q = c_p T_2 + \frac{1}{2} u_2^2 \tag{2.3}$$

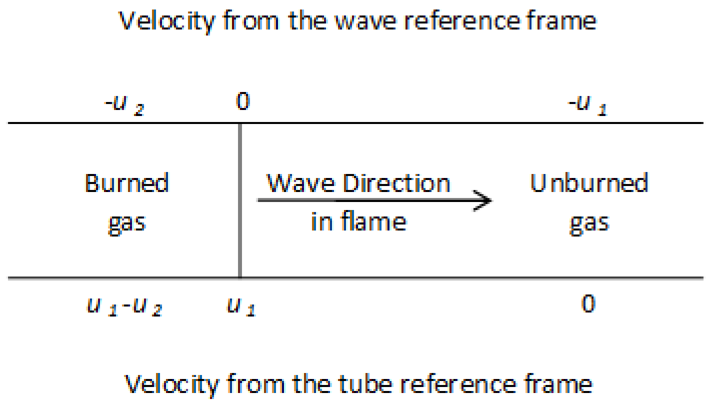

Figure 2.1: Velocity definitions for combustion analysis

The conservation of mass equation (Equation (2.1)) and the conservation of momentum equation (Equation (2.2)) can be combined in order to form Equation (2.4). Equation (2.4) forms the Rayleigh line, which describes the pressures and densities of the products and reactants for a combustion reaction at a given mass flow (Turns, 2006).

$$P_2 = P_1 + \rho_1^2 u_1^2 \left(\frac{1}{\rho_1} - \frac{1}{\rho_2}\right) \tag{2.4}$$

If the combustion gases are considered ideal and with constant specific heats and specific heat ratios, the three conservation equations (Equations (2.1), (2.2), and (2.3)) can be combined into the Hugoniot relation shown in Equation (2.5). The Hugoniot relation describes the heat release from the system as a function of the pressures, densities, and specific heat ratio of the products and reactants (Glassman, 2008).

$$q = \frac{\gamma}{\gamma - 1}\left(\frac{P_2}{\rho_2} - \frac{P_1}{\rho_1}\right) - \frac{1}{2}(P_2 - P_1)\left(\frac{1}{\rho_1} + \frac{1}{\rho_2}\right) \tag{2.5}$$

It is easily seen from Equation (2.5) that if there is no heat release (q=0), then a point exists on the curve of P_2 vs $1/\rho_2$ where $P_1 = P_2$ and $1/\rho_1 = 1/\rho_2$. However, if heat is released, (q>0) then the curve will shift up and to the right of the original curve, as shown in Figure 2.2.

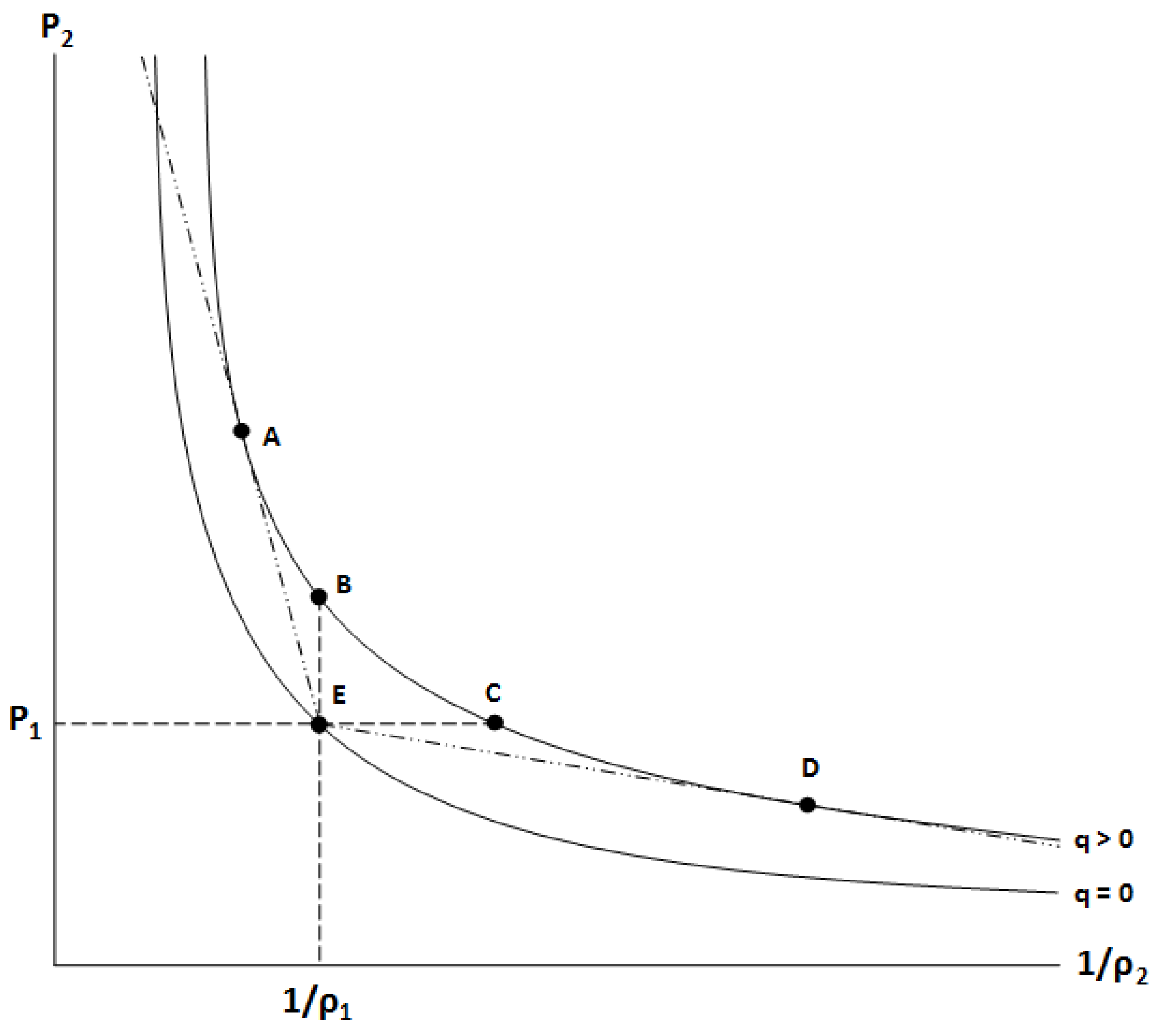

Figure 2.2: Hugoniot curves and various Rayleigh lines with Chapman-Jouget points.

The process of combustion and subsequent heat release causes the properties of the reactants to lie along the curve with no heat release and the properties of the products to lie along the curve with heat release. In fact, the properties of the reactants are always at P_1 and $1/\rho_1$ on the curve with no heat release (point E). However, the properties of the products only lie along the points on the heat release Hugoniot curve that comply with the Rayleigh line (Equation (2.4)) in addition to the Hugoniot curve (Equation (2.5)) (Turns, 2006). Since the Rayleigh line equation (Equation (2.4)) only produces lines with a negative slope and must pass through point E, the products of the combustion reaction must fall above point B or below point C on the heat release Hugoniot curve in order to satisfy both equations. The points A and D are the two points where the Rayleigh line is tangent to the Hugoniot heat release curve and are known as the Chapman-Jouget points. Point C describes the products of the combustion reaction if the reaction is performed under constant pressure conditions, and Point B describes the products of the combustion reaction if the reaction is performed under constant volume conditions. These four points A-D on the heat release Hugoniot curve break the curve into 5 separate sections where the properties of the products could lie.

The section of the curve above point B is the detonation region, the section below point C is the deflagration region, and the section between points B and C is the invalid solution region. In addition to not satisfying the Rayleigh line equation, the section between points B and C gives invalid solutions because it requires the products to have a greater pressure and a lower density than the reactants. This change can only occur if an increase in mass or temperature occurred in the system. Since the system is closed and mass is conserved in the process, an increase in mass is not possible. Also, the temperature of the system cannot increase since the movement from point E on the first curve to the second curve is the result of heat release from the system. In addition to the analysis from gas properties, the region between points B and C is invalid because of conservation of mass and momentum. This invalid can be derived from manipulating the equations describing conservation of mass and momentum in Equations (2.1) and (2.2). If these two equations are combined in order to eliminate the quantity u_2, then the velocity of the wave can be expressed solely in terms of the pressures and densities.

$$u_1 = \frac{1}{\rho_1}\sqrt{\left[\frac{P_2 - P_1}{\left(\frac{1}{\rho_1} - \frac{1}{\rho_2}\right)}\right]} \tag{2.6}$$

If Equation (2.6) is used to calculate the wave velocity for a point along the curve between points B and C, P_2 will be greater than P_1 and $1/\rho_2$ will be greater than $1/\rho_1$, which will always result in the velocity being an unreal number. This analysis proves that this section of the curve does not yield valid solutions since it is impossible for the wave velocity of a propagating flame to be an unreal number.

The removal of the curve between points B and C leaves two separate sections of the curve remaining for possible solutions. In order to examine the properties of the combustion reaction in each of these two regions, the analysis once again begins with the conservation of mass and momentum described in Equations (2.1) and (2.2). If these two equations are combined in a similar way to Equation (2.6), but instead in order to eliminate the quantity u_1, then the velocity of the burned gases in the reference frame of the flame front can be expressed solely in terms of the pressures and densities.

$$u_2 = \frac{1}{\rho_2}\sqrt{\left[\frac{P_2 - P_1}{\left(\frac{1}{\rho_1} - \frac{1}{\rho_2}\right)}\right]} \tag{2.7}$$

The equations describing both u_1 and u_2 can be used to describe two important relations. The first is the velocity of the burned gases in the reference frame of the combustion tube, shown in Equation (2.8). Equation (2.8) is formed by subtracting Equation (2.7) from Equation (2.6).

$$\Delta u = u_1 - u_2 = \sqrt{(P_2 - P_1)\left(\frac{1}{\rho_1} - \frac{1}{\rho_2}\right)} \tag{2.8}$$

The second relation is the ratio of the velocity of the burned gases to the velocity of the flame front in the reference frame of the combustion tube, shown in Equation (2.9). Equation (2.9) is formed by dividing Equation (2.8) by Equation (2.6).

$$\frac{\Delta u}{u_1} = 1 - \frac{1/\rho_2}{1/\rho_1} \tag{2.9}$$

Equation (2.9) yields a very important result. For the portion of the curve above point B, the ratio of the burned gases to the velocity of the flame front is greater than zero, and for the portion of the curve below point C, the ratio is less than zero. This result means that above point B the burned gases flow in the same direction as the flame front with respect to the tube, and below point C the burned gases flow in the opposite direction as the flame front with respect to the tube. Therefore, combustion reactions that are above point B create compression waves and a pressure gain, while combustion reactions that are below point C create expansion waves and a pressure loss.

Another characteristic that varies between these two sections of the curve is the Mach number of the combustion wave, M_1. The expression for this quantity is derived from combining the equation of the definition of the speed of sound (Equation (2.10)) and the equation of the definition of the Mach number (Equation (2.11)) into Equation (2.6). The result, Equation (2.12), expresses the Mach number of the combustion wave in terms of the pressures, densities, and the ratio of specific heats.

$$c = \sqrt{\gamma R T} \tag{2.10}$$

$$M = \frac{u}{c} \tag{2.11}$$

$$M_1 = \sqrt{\frac{1}{\gamma}\left[\frac{\left(\frac{P_2}{P_1}\right) - 1}{1 - \left(\frac{1/\rho_2}{1/\rho_1}\right)}\right]} \tag{2.12}$$

The results of Equation (2.12) for a particular point on the curve can be determined by examining Figure 2.2. If the point in question is above point B, then every small decrease in $1/\rho_2$ causes a great increase in P_2. This relationship between the pressure and the density will cause the ratio inside the brackets to be much greater than the value of γ, which is typically near 1.4, and result in M_1 being greater than 1. On the other hand, if the point in question is below point C, then every small decrease in P_2 causes a great increase in $1/\rho_2$. This relationship will cause the ratio inside the brackets to be much less than 1, which results in M_1 being less than 1.

This analysis shows that the Rankine-Hugoniot curve is split into two distinct regions. The first region is above point B and is characterized by an increase in pressure as a result of the combustion and a supersonic propagating combustion wave. The second region is below point C is characterized by a decrease in pressure as a result of the combustion and a subsonic propagating combustion wave. A supersonic combustion reaction that results in a pressure rise is known as detonation combustion, and a subsonic combustion reaction that results in a pressure loss is known as a deflagration. Although the combustion wave speed and pressure change are the primary characteristics that distinguish a combustion reaction as detonation or deflagration, Table 2.1 shows how several other properties vary as well (Glassman 2008, 262).

	Typical Magnitude of Ratio	
Ratio	**Detonation**	**Deflagration**
u_u/c_u	5-10	0.0001-0.03
u_b/u_u	0.4-0.7	4-16
P_b/P_u	13-55	0.98-0.976
T_b/T_u	8-21	4-16
ρ_b/ρ_u	1.4-2.6	0.06-0.25

Table 2.1: Qualitative differences between detonations and deflagration in gases

2.2: Comparison of Deflagration and Detonation Thermodynamic Cycles

As mentioned previously, the deflagration combustion process involves nearly constant pressure combustion, and the detonation combustion process involves pressure gain combustion. The ideal constant pressure combustion process is modeled by the Brayton cycle and the ideal constant volume combustion process is modeled by the Humphrey cycle. The thermodynamic differences in these two cycles are presented in the pressure versus specific volume and the temperature versus entropy plots shown in Figure 2.3. All of the combustion processes shown in the cycles of Figure 2.3 are conducted with the same amount of heat addition.

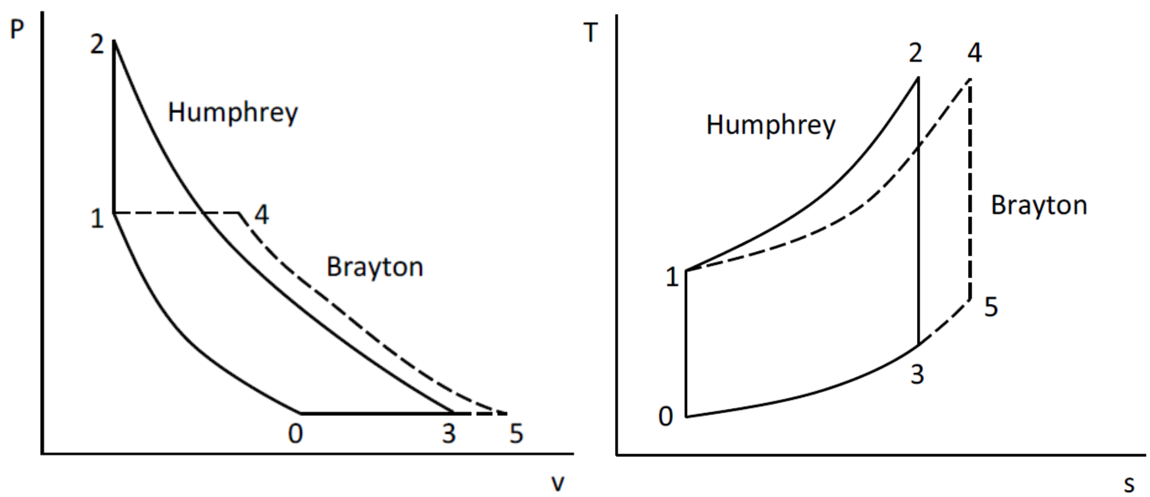

Figure 2.3: Thermodynamic cycles of constant volume and constant pressure combustion

The constant pressure combustion process takes place for the Brayton cycle on the pressure versus specific volume plot during the transition from state 1 to state 4. This process line is horizontal since it is a constant pressure process and the pressure is represented by the y-axis. In contrast, the constant volume combustion process for the Humphrey cycle on the pressure versus specific volume plot is the transition from state 1 to state 2. This process line is vertical since the volume remains constant during this process and the specific volume is represented by the x-axis. In a similar way, the constant volume combustion process of the Brayton cycle is shown as the process line from state 1 to state 4 on the temperature versus entropy diagram. This process line falls along one of the constant pressure lines in the temperature-entropy space. Once again the combustion process of the Humphrey cycle is shown as a pressure gain process from state 1 to state 2 in the temperature versus entropy plot. This process line begins at the same point as the Brayton cycle process, but finishes along a higher constant pressure line at the same temperature in the temperature-entropy space.

The pressure versus specific volume diagram shows that more work can be obtained by expanding the combustion products of the Humphrey cycle (point 2 to point 3) to their initial pressure than the combustion products of the Brayton cycle (point 4 to point 5) since the area of the pressure versus specific volume plot enclosed by the shape 1234 is larger than the area enclosed by the shape 0145. A similar result is seen in the temperature versus entropy diagram since the expansion of the combustion products of the Humphrey cycle (point 2 to point 3) to their initial pressure covers a greater temperature range than the combustion products of the Brayton cycle (point 4 to point 5). The temperature versus entropy diagram also shows that the Humphrey cycle combustion process (state 1 to state 2) creates less entropy than the Brayton cycle combustion process (state 1 to state 4). The lower amount of entropy produced by combusting the same reactants with the same amount of heat addition demonstrates that the Humphrey cycle is more efficient when compared to the Brayton cycle. It is important to note that the detonation cycle is not exactly modeled by the Humphrey cycle, but it is similar enough to use in the comparison of the thermodynamic efficiencies of detonation combustion engines to deflagration combustion engines (Kailasanath, 2000).

2.3: Previous RDE Work

The earliest RDE work was performed by the Russian scientist B. V. Voitsekhovskii, as well as J. A. Nicholls in the United States in the 1960s. This research investigated the feasibility of an RDE, but only detonated fuels with gaseous oxygen or an oxygen-inert gas mixture with much greater percentages of oxygen than atmospheric air. The next two decades passed without much research in the field of rotating detonation engines until the work of Bykovskii in the 1990s. Bykovskii performed continuous detonations with a number of gaseous and liquid fuels with gaseous and liquid fuels that generated wave speeds of 1680 to 2000 m/s depending on the mixture. In addition to the detonation wave speed, Bykovskii also compared detonations performed with air and oxygen enriched air. He observed that the detonation wave formed from the oxygen enriched air increased the luminosity and the wave speed when compared to the detonation wave formed from the atmospheric air (Bykovskii et al, 1997).

In addition to Bykovskii's work in Russia, the increased demand for a more efficient combustion processes near the end of the 20th century has rekindled interest in detonation combustion in China, France, Japan, Poland, Singapore, and the United States

(Davidenko, 2011). The Chinese efforts have focused on creating numerical simulations in order to perform analyses on topics such as the performance of an RDE (Shao et al, 2010), and the effect of the altering the injection pressure (Liu et al, 2011) or the nozzle (Shao et al, 2010). In France, a number of theoretical and numerical studies are being developed by the research group ICARE in order to gain a better understanding of RDEs, especially in the area of comparing the performance of an RDE to a conventional rocket engine (CRE) (Davidenko, 2011). The ICARE team is also coordinating with the French division of MBDA, a missile system and technologies company. MBDA has designed an RDE to combust a mixture of liquid oxygen and liquid hydrogen in order to experimentally compare the performance characteristics of an RDE to a conventional rocket engine (Falempin et al, 2009).

Japanese efforts have primarily investigated the theoretical and numerical aspect of RDEs. Some of the research topics that have been studied are the limits of detonation operation (Yamada et al, 2010), and the structure of the detonation and its attached shock in an RDE (Hishinda et al, 2009). In addition to these numerical studies, some collaborative work has also been performed to compare numerical results with the experimental results of RDE operation performed by the Polish researchers Kindracki and Wolanski (Hayashi, 2009). Other Polish experiments have investigated the rocket applications for RDEs (Kindracki et al, 2011) and the formation and stability of multiple detonation waves (Wolanski, 2011). In addition to the experimental tests, some Polish efforts have focused on the numerical analysis of the RDE in areas such as the prevalence of deflagration combustion in an RDE (Folusiak, 2010). Singapore has also conducted

RDE research through numerical methods. These numerical studies have investigated aspects of RDE operation such as the characterizing the flow field in the engine (Yi et al, 2009) and the effects of various nozzle designs (Yi et al, 2010).

Lastly, a variety of groups in the United States have been conducting research in the RDEs field as well. Numerical research has been performed on areas such as flow propagation upstream into the mixture plenum (Schwer et al, 2012) and the thermodynamics of the detonation wave in an RDE (Nordeen et al, 2011). In addition to these numerical investigations, a number of experimental groups are studying RDEs as well. The Detonation Engine Research Facility at Wright-Patterson Air Force Base has successfully tested rotating detonation engines with diameters of 3 inches (Suchocki et al, 2012), 6 inches (Shank et al, 2012), and 20 inches (Dyer et al, 2012). RDE testing has also been performed at the University of Texas at Arlington (Braun et al, 2010) and at Pennsylvania State University.

Chapter 3: Facility and Experimental Setup

3.1: The Detonation Engine Research Facility

The experiments for this research were performed in the Air Force Research Laboratory's Detonation Engine Research Facility at Wright-Patterson Air Force Base. The testing area for this facility is a 750,000 cubic foot test cell. The roof of the cell is designed to rise into the air if pressure builds inside the cell in order to allow any excess pressure to escape the cell and avert an explosion. All tests in the cell are remotely controlled and performed on the opposite side of reinforced concrete walls that are at a minimum two feet thick. No fuel will run to any of the test rigs if the six inch thick steel door to the cell is not closed and latched. In order to make sure that no one is present inside the cell before the door is closed, all personnel are required to activate a ~100 dB train horn as a warning to others to vacate the cell before they are permitted to close the door. The two foot thick reinforced concrete walls provide both a physical barrier in the case of debris from a catastrophic failure and a sound barrier to the up to 200 dB sound waves emanating from the detonation engines. In case of a fire inside the cell, the facility is equipped with a carbon dioxide fire suppressant system that is capable of filling the entire 750,000 cubic foot cell with carbon dioxide in four seconds.

The facility is equipped with feed lines rated at or above 2,000 psi for both the fuel and oxidizer lines. The facility has a wide variety of fuels available, such as hydrogen, ethylene, methane, ethanol, JP fuels, gasoline, Avgas, and others. The facility also is equipped to run compressed atmospheric air, oxygen enriched air, nitrous oxide, and oxygen as oxidizers. The diagram of the layout for the fuel and oxidizer lines is shown in Figure 3.1. The oxidizer lines are shown in blue and the fuel lines are shown in red.

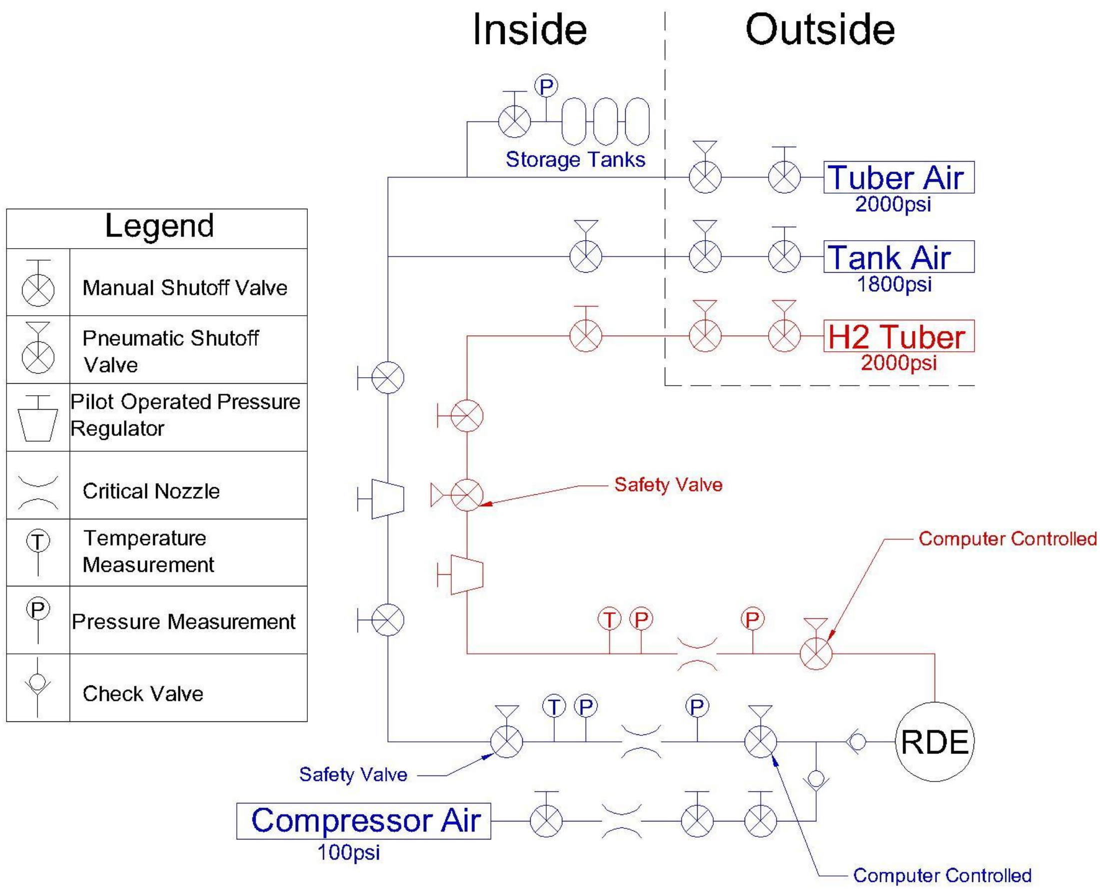

Figure 3.1: Facility fuel and oxidizer supply lines

Figure 3.1 also shows the cooling system for the Pratt RDE, which is shown at the compressed air tank at the bottom of the diagram. The supply line for the cooling air is fed from a 100 psi tank that is primarily used for operating PDEs in the lab with atmospheric air for the oxidizer. A check valve blocks the cooling air from mixing with the engine's oxidizer supply while the engine is running, but will allow the cooling air to run through the engine once the flow of the oxidizer into the flow is discontinued. This cooling air setup allows many more tests to be performed in a given time frame while greatly reducing the possibility of excessive heat damaging the engine parts.

3.2: The Pratt & Whitney SAC Rotating Detonation Engine

The engine used in all of the experiments presented in this document is a rotating detonation engine designed by Pratt & Whitney's Seattle Aerosciences Center, which was loaned to the Air Force Research Laboratory. The engine was initially designed to combust ethylene and oxygen through either premixing or separate injection into the detonation channel. However, when the rig was loaned to the Air Force Research Laboratory for further development and testing, it was redesigned to detonate hydrogen and air, which were only used through separate injection into the detonation channel (Thomas et al, 2011). The engine features an annular combustor with an outer diameter of 3 inches and an inner diameter of 2.84, 2.53, or 2.21 inches, depending on the diameter of the centerbody placed in the middle of the detonation annulus. The combustor extends to an axial height of 4 inches. The lower 2 inches of the combustor outer shell has 0.8

inch thick copper walls, which interfaces with 0.5 inch steel walls for the upper 2 inches of the outer shell.

In addition to the ability to vary the width of the detonation channel by varying the diameter of the centerbody, the entry point of the fuel and air into the detonation channel can also be customized by using alternative injection parts. Along with the entry point of fuel and air into the channel, the gross injection area of the oxidizer and the fuel could be changed as well. The engine was tested with oxidizer gross injection areas of 0.123 in^2 and 0.227 in^2. The gross injection area of the fuel was kept constant at 0.038 in^2, but could be altered by machining new injection parts.

The engine features no moving parts, as the fuel and oxidizer flows into the engine are driven by pressure gradients. Because of this, the operating conditions of the engine were modified by changing the upstream pressures of the fuel and air by use of pressure regulators. The mass flows of the fuel and the oxidizer into the engine were determined through the use of sonic nozzles. As shown in Figure 3.1, both the fuel and air flow system incorporated sonic nozzles, with pressure readings taken upstream and downstream of the nozzles. If the ratio of upstream to downstream pressure met or exceeded 1.2, then the flow through the critical nozzles was considered choked (Flowmaxx Engineering). After each test, the pressure upstream and downstream of both the fuel and air sonic nozzles was checked to ensure that the nozzles were choked. This choked condition allowed the mass flow through the sonic nozzle to be computed from the upstream pressure of the sonic nozzle through gas dynamic relations.

The engine was mounted to a test stand with the axis oriented vertically, as shown in Figure 3.2. The flow of fuel and air entered from below the engine and the exhaust exited from the top of the engine. The engine was mounted with three pillow blocks on three surrounding poles in order to allow the engine to move vertically during operation. Six flexible steel braided hoses carried the air from a manifold below the engine out and around the poles supporting the engine to the air manifold.

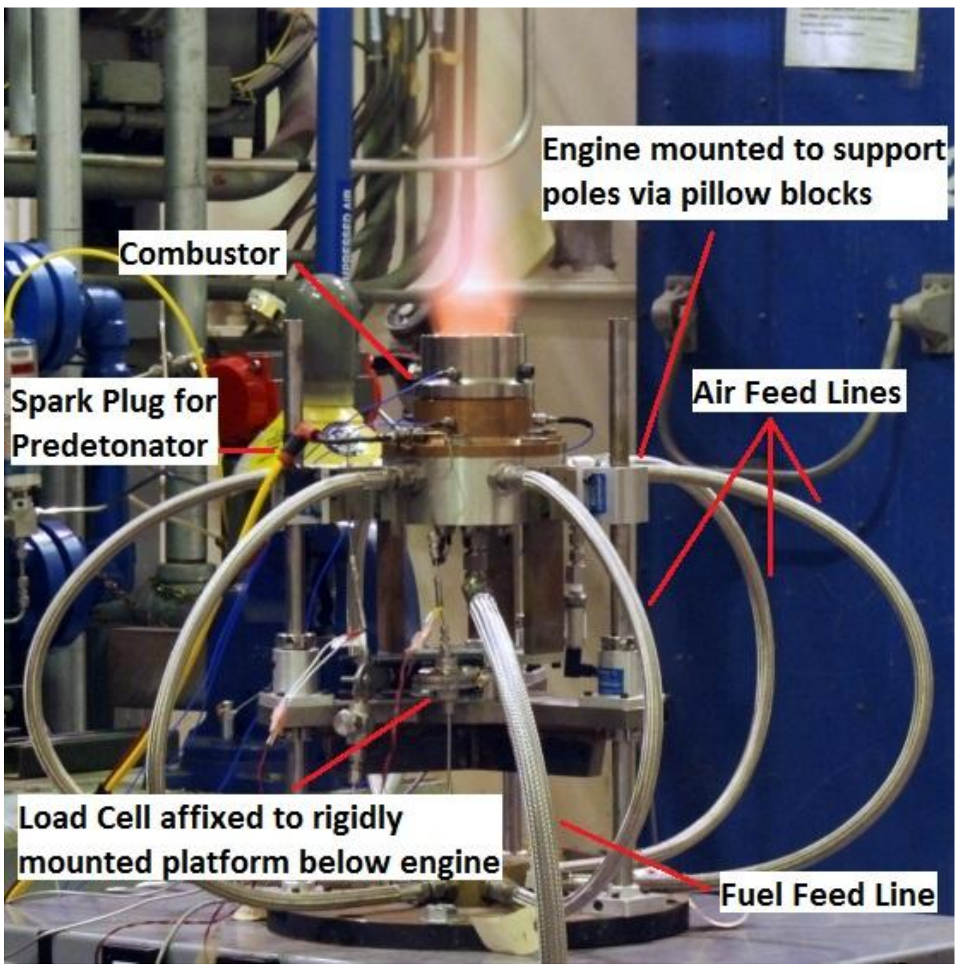

Figure 3.2: Pratt & Whitney experimental RDE with component labels

One flexible braided steel hose carried hydrogen to the fuel manifold. Since the exhaust exited the engine in the positive vertical direction, a 2,000 pound load cell was affixed to a rigidly mounted surface below the engine in order to measure the thrust from the engine. The pre-detonator used for initiating the detonation combustion reaction in the engine was ignited by a Multiple Spark Discharge (MSD) system. The pre-detonator uses two micro-solenoids to inject 0.5-1.0 cubic centimeters of hydrogen and oxygen into the body of the pre-detonator at a stoichiometric ratio of 2.0 prior to ignition from the spark plug (Thomas et al, 2011). After ignition, the detonation propagates along a tube tangentially connected to the pre-detonator through the outer combustion shell, where it will ignite the engine by propagating into a detonable mixture that is continuously flowing in the combustion channel.

In order to characterize the combustion reaction occurring inside the detonation channel, a number of radial holes were made in the combustor outer shell for the use of high sampling rate pressure sensors. These pressure sensors were either piezoelectric pressure sensors (PCBs) to measure the dynamic pressure or Kulite pressure sensors to measure absolute pressure. Although both sensors were used during testing, the vast majority of the pressure measurements were performed by the PCBs. The PCBs were used to indicate if the combustion was a detonation, how fast the combustion wave was travelling, and how steady the combustion was travelling.

PCB Hole #	Radial Position (deg)	Height above Channel Bottom (in)
1	0	2.60
2	30	0.75
3	90	0.75
4	90	1.30
5	90	2.60
6	110	0.28
7	128	0.38
8	150	0.75
9	180	2.60
10	270	2.60
11	270	2.60

Table 3.1: Locations of PCB ports in the outer combustor shell of the RDE

The outer combustor shell has eleven holes for PCB sensors at various radial positions and heights. When a PCB hole was not used for a test, it was plugged with a bolt with the same thread as a PCB. All of the PCB holes in the combustor outer shell are shown in Table 3.1, along with their radial location and distance from the bottom of the detonation channel to the center of the hole.

In addition to the PCB ports in the combustor outer shell, a thermal well was also placed in the combustor outer shell of the engine, at a radial position of 126° and 2.60 inches above the bottom of the detonation channel. This well left a 0.05 inch thick region of steel between the bottom of the well and the detonation channel. During some tests, a thermocouple was inserted into this well and made contact with the surface of the 0.05 inch thick barrier to the detonation channel in order to measure the temperature of the combustor outer shell. This temperature was used as a primary indicator to determine if the combustion that occurred during a test was inside the channel. If the majority of the combustion took place inside channel during a test run, the thermocouple in the thermal well would increase by 25, 50, or even 100 degrees Fahrenheit by the end of a one second test run. If the temperature inside the well increased by 5 degrees Fahrenheit or less, this indicated that the majority of the combustion was not inside the channel. The thermocouple in the thermal well also monitored the temperature during cooling and was used to indicate when the body of the engine was near enough to ambient temperature to perform another test run. In order to obtain visual evidence of the detonation combustion wave in the engine, a high speed camera was used to visually record the combustion inside the engine by viewing directly into the detonation channel from above. The video recording was accomplished by erecting a mirror about ten feet directly above the engine to provide the high speed camera with a line of sight into the detonation channel without requiring the camera to be physically located directly above the engine. Using a mirror system kept the camera on the ground, which greatly reduced the likelihood of damaging the camera from the heat of the engine exhaust, debris, or falling.

3.3: Controlling the Engine

The operation of the engine was operated through a LabVIEW interface that controlled the timing of air and fuel flow, the upstream pressure of the fuel and air feed lines, and the collection of some experimental data. This program allowed the user to adjust a number of variables of the test run in order to accomplish the desired run conditions. A list of these variables with their descriptions is provided in Table 3.2.

Controlled Variable Name	Description
Rate	Sampling rate frequency for data acquisition
Samples	Number of samples to be collected
Operating Fuel Time	Amount of time fuel is on after ignition
Fuel Establishing Time	Amount of time prior to ignition that fuel is turned on
Injector Pulse Width	Amount of time the predet injectors flow the reactants
Predet Spark Wait	Amount of time between predet injectors closing and spark
Air Establishing Time	Amount of time prior to ignition that air is turned on
Operating Air Time	Amount of time air is on after ignition
Predet Test Cycles	Number of times the predet is fired during a predet test
Air Pressure	Sets the upstream pressure of the air feed line
Fuel Pressure	Sets the upstream pressure of the fuel feed line

Table 3.2: Variables controlled by the LabVIEW RDE control program

The LabVIEW program controlled the variables in Table 3.2 in various ways. The inputs to the Sampling Rate and Samples variables were executed by the program adjusting the frequency and duration of the data collection performed by the control computer. The inputs to the Fuel and Air Establishing and Operating Time fields were carried out by the control computer sending a voltage to a power relay, which controlled the flow of nitrogen pressure to a pneumatic solenoid valve, which would either open or close the feed line. These pneumatically actuated solenoid valves are the pneumatic valves in Figure 3.1 that are labeled as “Computer Controlled”. The Predet Spark Wait adjusted the amount of time between firing signals sent by the control computer to the spark plug, and the Number of Predet Test Cycles varied the number of times the control computer carried out the pre-detonator firing sequence during a pre-detonator test. A pre-detonator test involved the control computer sending voltages to the micro-solenoids on the hydrogen and oxygen pre-detonator lines for the amount of time necessary to allow

0.5-1.0 cubic centimeters of reactants into the body of the pre-detonator at an equivalence ratio of 2, then sending a number of pulses at the specified amount of time between pulses to the spark plug. The Air and Fuel Upstream Pressures were set by the control computer sending the upstream pressure inputs to a TESCOM electronic pressure regulator.

All of the variables described in Table 3.2 are controlled on the main screen of the program shown in

Figure 3.3 except for the air and fuel upstream pressures, which are adjusted on the Flow Control screen.

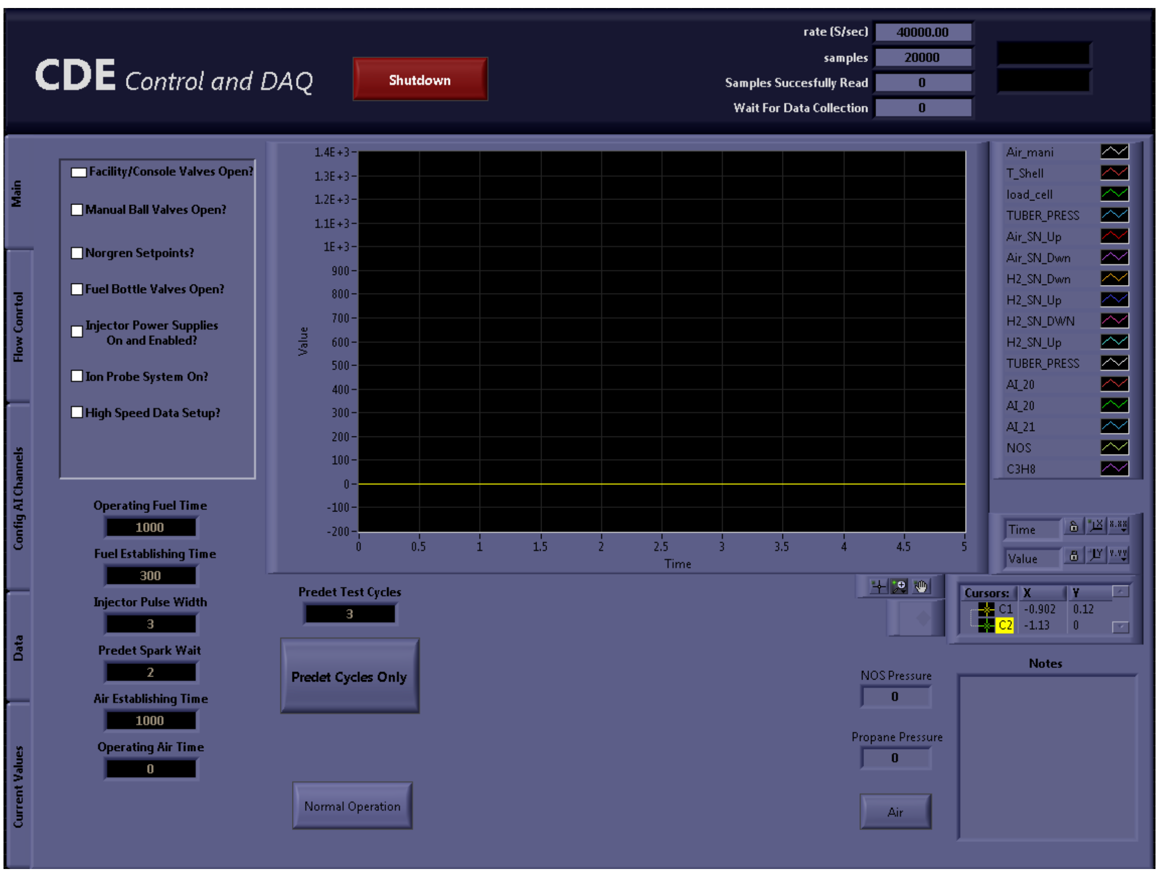

Figure 3.3: LabVIEW control program for the Pratt & Whitney RDE

Before the engine could be operated, each item on the check list in the upper left corner of the main screen had to be checked. The program would not allow the engine to fire until this check list was completed. After a run was completed, a plot of all of the measured quantities the program was collecting during the run was displayed in the graph window of the main screen. The computer automatically saved a file containing all the data points collected during the run with the date and time of the run in the file name.

The total time for data collection was determined by dividing the number of samples by the sampling rate, and the amount of time that the engine combusted fuel and air was determined by the value of the Operating Fuel Time, as the engine was shut off by stopping the flow of fuel into the combustor. In the case of ignition failure, blowout, or other event that resulted in no combustion, the non-combusting fuel and air flows into the engine could be stopped by turning off the buttons allowing fuel and air flow into the rig on the control console in the control room. In the case of emergency or catastrophic failure, a large emergency stop button on the control console in the control room could be pushed to close all fuel and air supply lines and shut off all power sources inside the test bay.

3.4: Data Collection

The LabVIEW control program acquired a large number of measurements during the test runs at a sampling frequency of 1 kHz. Most of these measurements indicated the operating point of the engine such as the mass flows, equivalence ratio, and injection pressures. A list of the quantities collected by the LabVIEW control program is listed in Table 3.3 with their description and purpose.

Description	Purpose
Air Sonic Nozzle Upstream Pressure	Ensure choked flow, mass flow
Air Sonic Nozzle Downstream Pressure	Ensure choked flow, mass flow
Fuel Sonic Nozzle Upstream Pressure	Ensure choked flow, mass flow
Fuel Sonic Nozzle Downstream Pressure	Ensure choked flow, mass flow
Air Manifold Pressure	Injection pressure
Fuel Manifold Pressure	Injection pressure
Air Supply Pressure	Available pressure
Channel Pressure	Combustion environment
Load Cell	Thrust
Shell Temperature	Engine temperature

Table 3.3: Measurements raken by the LabVIEW engine control program

Not all of these measurements were taken for every test, as some engine configurations and operating conditions dictated otherwise. However, the pressure readings upstream and downstream of both the air and fuel sonic nozzles were taken for every run in order to ensure that the flow was choked and the mass flow and equivalence ratio of the run could be determined. These quantities were taken at a sampling rate of 1 kHz in order to adequately capture variations during a test run, but none of the measured quantities varied on short enough time scales to warrant a higher sampling frequency.

The high speed camera that viewed the detonation wave propagating inside the engine recorded at a sampling frequency in the 50 kHz region. The sampling frequency of the camera was bound by the frequency of the detonation in the channel and the exposure time. Since the frequency of the detonation propagation was normally in the range of 5-10 kHz, the sampling frequency could not be reduced much below 50 kHz and still produce a relatively smooth video of the detonation wave propagating around the detonation channel. On the other hand, raising the sampling frequency above 50 kHz limited the exposure time to the extent that the light from the detonation began to be difficult to discern in the images. Therefore, for most of the tests performed, the high speed camera collected images of the detonation propagating inside the engine at a sampling rate of 50 kHz.

The last data collection method was for collecting the pressure data from the PCBs or Kulites positioned in the combustor outer shell. The sampling frequency of these sensors was 1-2 MHz, which was much greater than the 50 kHz sampling rate of the high speed camera. The PCB sampling frequency was much greater due to the finite area of the detonation channel that could be measured by the PCB and the desire to record the pressure profile of the combustion wave as it passes the sensor. Since each PCB was fixed to a certain point in the combustor outer shell, each sensor could only record the pressure at any given time at the location where it was placed. Therefore, the PCBs did not have the luxury of measuring the pressure of the entire channel at any given time, unlike the high speed camera that could take a picture of the entire channel to determine the brightest point. Having this fixed location required a much higher sampling rate than the high speed camera so that the detonation wave of finite width would not be missed when it passed caused the sensor. In addition to the finite area of measurement, the MHz sampling frequency for the PCBs was used in order to observe the pressure profile of the combustion wave as it passed the sensor. Without such a high sampling frequency, the pressure of the combustion at various parts of the wave could not have been determined.

3.5: Operating Procedure

The testing procedure began by following a setup procedure that indicated which valves needed to be opened or closed, and what safeties needed to be engaged. During this setup, the oxidizer and fuel that would be combusted in the engine during that testing sequence would be connected to appropriate feed lines for the engine. The oxidizers that were used for the test runs were either atmospheric air with 21% oxygen, or enriched air with either 23% oxygen and 77% nitrogen or 24.8% oxygen and 75.2% nitrogen. Hydrogen was used as the fuel for all of the engine tests that were performed.

After the setup procedure was completed, the bay was cleared and the steel door to the bay was closed. If the testing schedule called for the tests to be in quick succession, then the cooling air system was turned on. A computer inside the control room remotely connected to the control computer in the lab in order to use the Pratt RDE LabVIEW control program. After the check list in the upper left of the main tab of the program was completed, the pre-detonator was tested by firing the number of tests shots specified in the "Predet Test Cycles" field. Immediately following the pre-detonator test, the high speed camera and the wave speed data were set to record on a trigger, which would be sent from the control computer when the command was given to fire the spark plug. Once the high speed camera and the wave speed data were ready, the engine was fired. When the control computer finished its data collection time, the pressures upstream and downstream of the sonic nozzles were checked to ensure that the flow through the nozzles was choked. If the flow was choked, the pressures upstream of the sonic nozzles were used to determine the mass flows and equivalence ratio, which were recorded in the lab record book. If the high speed data or the PCB data showed useful results, these files were saved and the file names associated with the appropriate run in the lab record book. Once the data was saved and the engine had cooled near enough to ambient temperature, which was typically 90° Fahrenheit, then the next test could be run.

Chapter 4: Calculations and Uncertainty

4.1: Calculations of Engine Performance

A large amount of the data collected from the experiments had to be used in part of a calculation in order to obtain useful information about the conditions of the run or the performance of the engine. One of these calculations was the mass flow of oxidizer and fuel into the engine. These mass flows were determined by flowing the fuel and air through sonic nozzles of known diameters and ensuring that the upstream pressure was at least a factor of 1.2 greater than the downstream pressure. If this sufficient drop in pressure was seen across the sonic nozzle, then the flow in the nozzle had achieved a sonic velocity. The mass flow through a nozzle that is sonic or choked can be determined by using the relation shown in Equation (4.1), which can be obtained by the manipulation of gas dynamics equations (Anderson, 2003).

$$\dot{m} = \frac{p_0 A^*}{\sqrt{T_0}} \sqrt{\frac{\gamma}{R}\left(\frac{2}{\gamma + 1}\right)^{(\gamma+1)/(\gamma-1)}} \tag{4.1}$$

The specific heats ratio γ, the specific gas constant R, and the upstream temperature of the gas all remain fairly constant for the fuel or oxidizer tested, and the critical area of the sonic nozzle A^* is constant for the size of the sonic nozzle placed in the line. Since the only remaining variable is the upstream pressure of the gas P_o, the mass flows of the fuel or the oxidizer could be determined for a given test by using the properties of the present engine configuration along with the upstream nozzle pressure measurement. The value for the upstream pressure was obtained by calculating the average value of the upstream air or fuel sonic nozzle pressure during the combustion period of the test run. This measurement was obtained by the data collected by the Pratt RDE control program.

Another calculation important for determining the conditions of a test run was the gross equivalence ratio of the fuel and air flowing into the engine. The equivalence ratio was determined by dividing the ratio of fuel mass flow to air mass flow for the run by the ratio of fuel mass flow to air mass flow at stochiometric conditions. This definition is shown mathematically in Equation (4.2).

$$\Phi = \frac{\dot{m}_{fuel}/\dot{m}_{air}}{\left(\dot{m}_{fuel}/\dot{m}_{air}\right)_{stoichiometric}} \tag{4.2}$$

The values of the numerator in Equation (4.2) are easily obtained by using experimental pressure data in Equation (4.1). However, the value of the denominator remains constant for a particular fuel and oxidizer combination. Since every experiment used hydrogen for the fuel and an oxygen-nitrogen mixture for the oxidizer, the formula presented in Equation (4.3) was used to calculate the stoichiometric fuel/air ratio for each particular fuel and oxidizer combination.

$$\left(\frac{\dot{m}_{fuel}}{\dot{m}_{air}}\right)_{stoichiometric} = \frac{2MW_{H_2}}{MW_{O_2} + \left(\frac{1}{O_2\%} - 1\right) MW_{N_2}} \tag{4.3}$$

Equation (4.3) calculates the stoichiometric fuel/air ratio by using the molecular weight *MW* of each species and the percentage of the oxidizer that is oxygen by mass.

The amount of thrust generated by the engine is very important for determining how well the engine is performing. Although the thrust generated by the detonation combustion was able to be measured by the load cell, the physical setup and testing procedure required the raw data to be properly reduced before useful results could be extracted. During the run, the load cell had four distinct regions of data that are shown in Figure 4.1 on a plot of the load cell reading in pounds as a function of time in seconds.

The first region was at the beginning and the end of the run when no fuel or air was flowing through the engine. In this region the load cell only read the weight of the engine. The second region covered from the onset of air flow through the engine to the onset of fuel flow through the engine. The third region began at the onset of fuel flow into the engine and ended at ignition. Finally, the fourth region was from ignition to shutdown, where the detonation was propagating through the mixture of fuel and air flowing into the engine. These regions are shown on a plot of the load cell reading as a function of time for a detonating run in Figure 4.1.

The gross thrust, the thrust from the combustion reaction, and the fuel and air flow thrust were all determined from analyzing the data in these four regions.

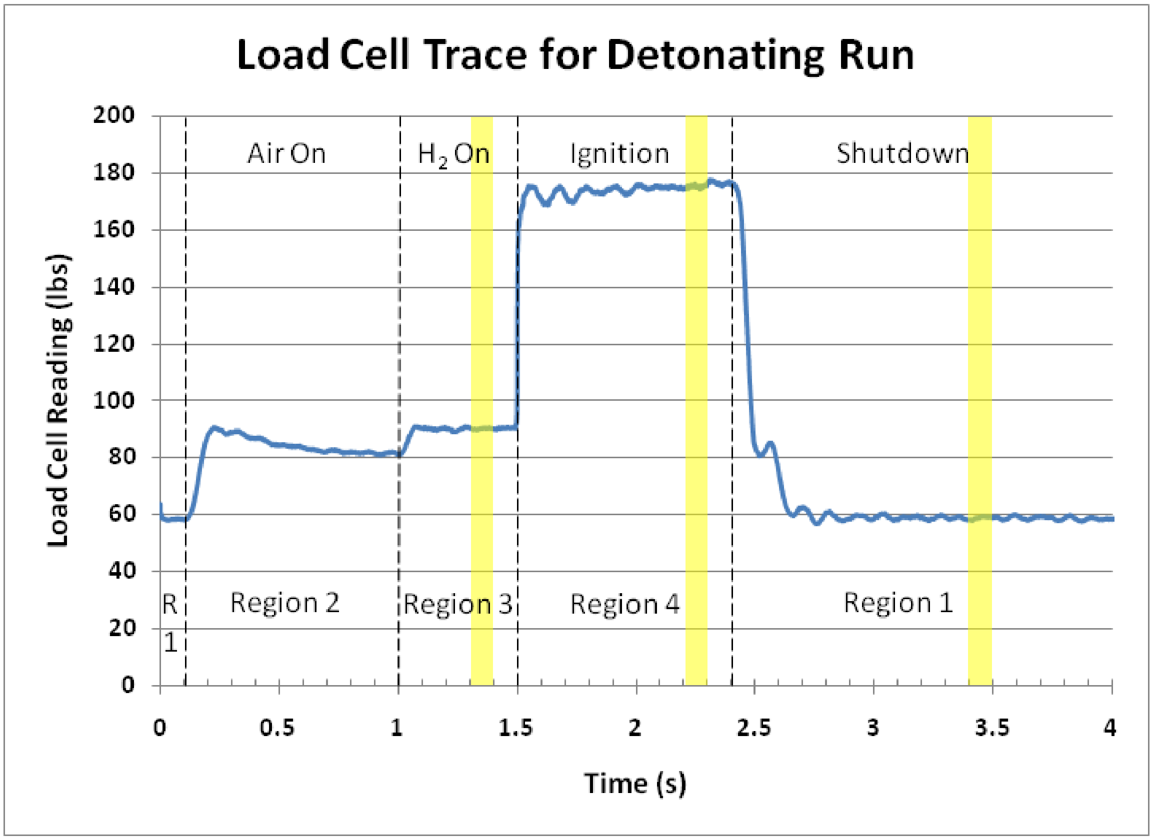

Figure 4.1: Load cell response for a detonation run

The load cell value from each region was determined by averaging the reading 0.2 to 0.1 seconds before the ending of the region, where an event took place. The regions of the load cell trace used form thrust measurements are highlighted in Figure 4.1. The average reading was taken 0.2 to 0.1 seconds before the end of the region in order to allow the transient effects from an event to diminish as much as possible before the average was taken, and to make sure none of the transient effects from the next event affected the measurement. Since there was not another event after the shutdown to use for this method, the Region 1 reading was taken 1.0 to 1.1 seconds after the shutdown event. The equations used to calculate these thrusts are shown respectively in Equations (4.4), (4.5), and (4.6).

$$Gross\ Thrust = \overline{Region\ 4} - \overline{Region\ 1} \tag{4.4}$$

$$Combustion\ Thrust = \overline{Region\ 4} - \overline{Region\ 3} \tag{4.5}$$

$$Flow\ Thrust = \overline{Region\ 3} - \overline{Region\ 1} \tag{4.6}$$

After the calculations for the mass flow of fuel and oxidizer and the calculations for gross thrust, thrust from the combustion, and fuel and air flow thrust were made, the specific impulse and specific thrust could be calculated. The specific impulse was defined as the thrust generated by the combustion divided by the mass flow of fuel into the engine. The specific thrust is defined as the thrust generated by the combustion divided by the mass flow of air into the engine. The specific impulse equation is shown in Equation (4.7) and the specific thrust equation is shown in Equation (4.8).

$$Specific\ Impulse = \frac{Thrust}{\dot{m}_{fuel}} \tag{4.7}$$

$$Specific\ Thrust = \frac{Thrust}{\dot{m}_{air}} \tag{4.8}$$

4.2: Calculations of Combustion Characteristics

The velocity and unsteadiness of the combustion wave as it propagated around the detonation channel in the engine were important metrics used to evaluate each run.

These measurements were obtained by one or more PCBs that collected pressure data during the run, which recorded the rise in pressure from each time the combustion wave passed the sensor. A sample of the data collected from a PCB while a detonation wave was propagating through the engine is shown in Figure 4.2.

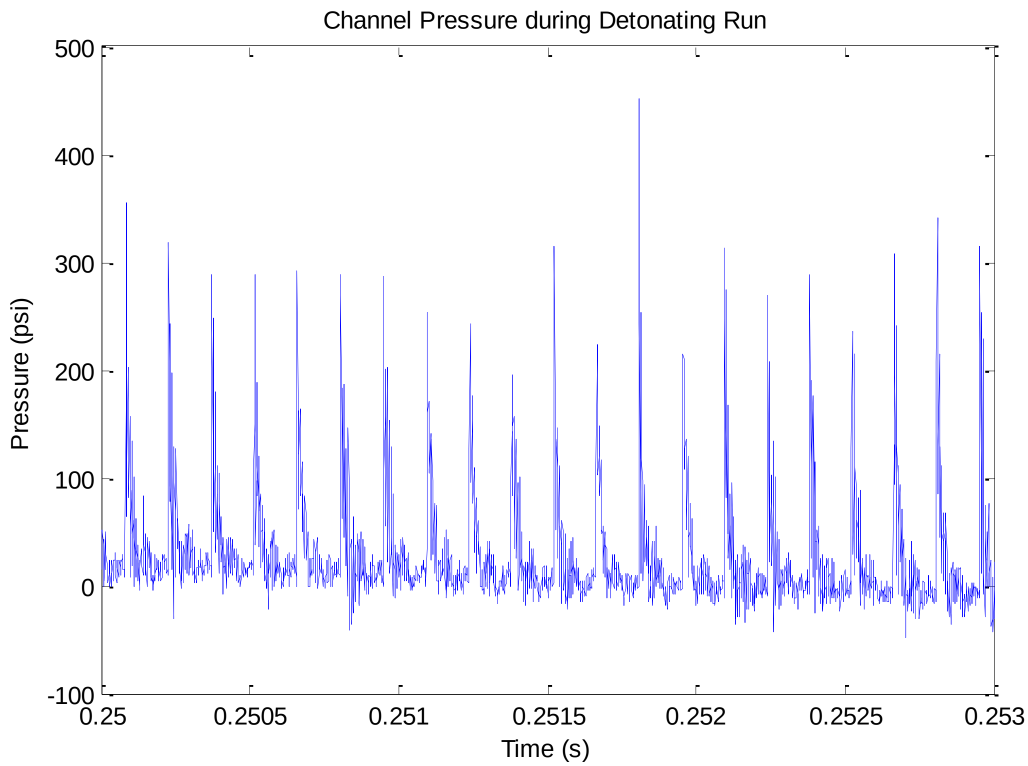

Figure 4.2: Pressure trace in the channel for a detonating run

Since the detonation travelled around the channel thousands of times per approximately one second run, a computer program was used in order to analyze the detonation wave data for the entire run. The analysis did not begin until 0.05 seconds into the run in order to allow time for the engine to ignite and establish a detonation. In addition, the analysis for some of the runs had to be ended prematurely when a PCB's signal decayed during the run or drifted below the voltage threshold due to excessive heating. These potential PCB failures made it necessary to visually inspect the pressure data from each run to identify the timing range of the analysis before any method for determining the combustion wave velocity could be conducted.

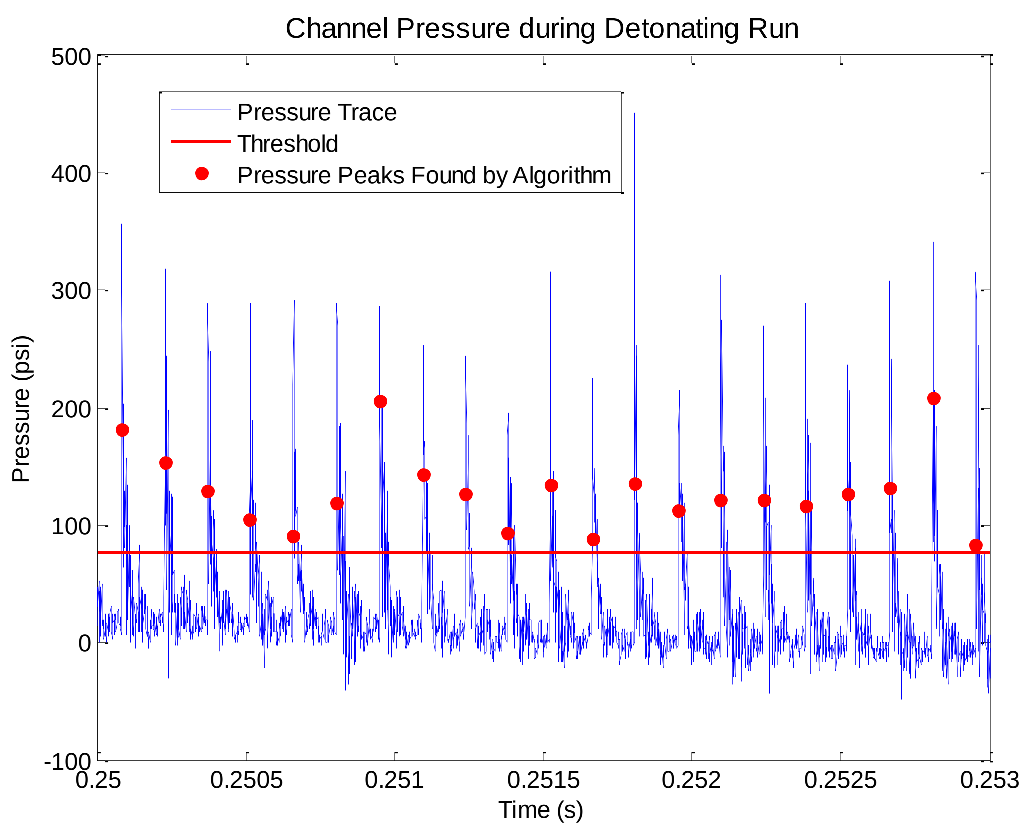

Figure 4.3: Pressure trace in the channel for a detonating run with pressure peaks found by the peak finding algorithm

The first method used to determine the velocity and unsteadiness of the combustion wave was by finding when each pressure peak occurred during a test run. This method began by running a peak finding algorithm to locate the thousands of pressure spikes in the data set. Figure 4.3 shows the same pressure data shown in Figure 4.2 in blue with red points for each time the peak finding algorithm identified a pressure spike, along with the threshold line used by the algorithm for peak detection. Every time the algorithm identified a pressure spike, the timestamp of that point was recorded, resulting in an array of the timestamps of every pressure peak found by the program. This array of the pressure peak times was used to calculate the average period, the average velocity, and the unsteadiness of the combustion wave. The equations for these calculations are shown in Equations (4.9), (4.10), and (4.11), respectively.

$$Avg\ Period = \frac{t_{final\ peak} - t_{first\ peak}}{Total\ Peaks - 1} \tag{4.9}$$

$$Avg\ Velocity = \frac{\pi d_{channel}^2}{4(Avg\ Period)} \tag{4.10}$$

$$Wave\ Unsteadiness = StDev\left(t_{p2} - t_{p1}, t_{p3} - t_{p2,}\ t_{p4} - t_{p3}, \dots\right) \tag{4.11}$$

The average period calculation in Equation (4.9) calculates the average amount of time between pressure peaks for the entire run by finding the difference between the time elapsed from the last peak found by the program $t_{final\ peak}$ and the first peak found by the program $t_{first\ peak}$. This difference is divided by one less than the number of peaks found in order to yield the average period of the combustion wave. The average velocity calculation in Equation (4.10) calculates the average velocity of the combustion wave by dividing the circumference of the channel by the average time the wave takes to complete a revolution of the channel, which is the average period. The wave unsteadiness calculation in Equation (4.11) began by calculating the difference in the time stamps between every set of adjacent pressure peaks. These differences were then stored in an array of time values one less in number than the array of the timestamps of the peaks themselves.

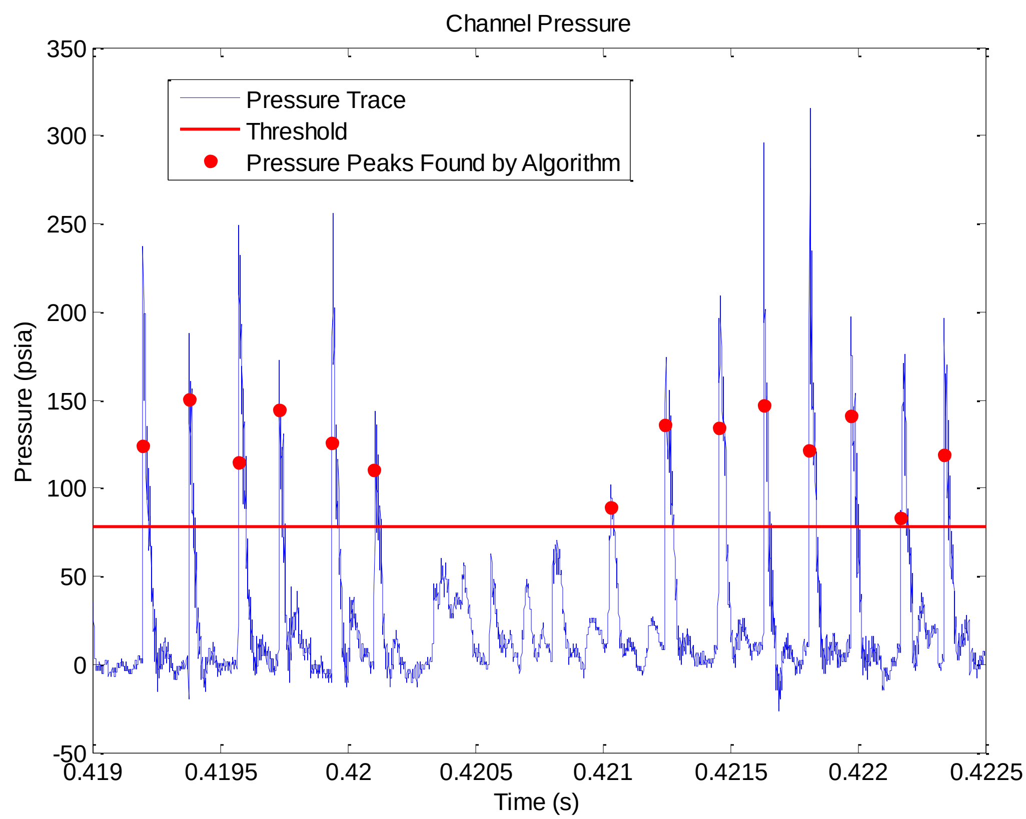

Figure 4.4: Pressure trace in the channel for an inconsistent detonating run with pressure peaks found by the peak finding algorithm

Finally, the standard deviation of this array of peak time differences was calculated in order to determine the unsteadiness of the wave. If the pressure peaks from the data were spaced relatively evenly, then each amount of time that elapsed between the pairs of pressure peaks would be very similar throughout the run, resulting in a low standard deviation and low wave unsteadiness. Alternatively, if the pressure peaks were erratically spaced in the pressure data, then the amount of time between different pairs of pressure peaks would vary widely throughout the run, resulting in a high standard deviation and high wave unsteadiness.

Although these calculations were very useful in determining the desired properties of the combustion wave propagating through the engine, the peak finding method for calculating the average velocity of the combustion wave had some problems. The method worked very well when the combustion wave propagated continuously during the entire run, but some of the runs on the edge of the operational space had constant degradation and re-ignition of the propagating combustion wave. When a wave eroded and later reestablished, the resulting pressure trace had a large stretch without any pressure peaks, as shown in Figure 4.4. These lull periods where the combustion activity in the channel was too unsteady or did not have strong enough pressure rises to be detected by the peak finding algorithm, the total number of peaks found by the algorithm decreased. Since the velocity of the combustion wave was dependent on the number of total peaks found, the average velocity calculation for a run with inconsistent detonations would be lower than the actual velocity of the combustion wave.

In order to avoid this problem, the pressure data was analyzed with a Fast Fourier Transform (FFT) in order to determine what wave frequency was most prevalent during the run. This wave frequency was easily converted to the most common velocity for the run without being effected by the intermittent wave activity, which made it the primary method of determining the velocity of the combustion wave. However, the peak finding method was still necessary for determining the wave velocity of the multimodal runs since the non-predominant wave form was very difficult to determine in the FFT plot.

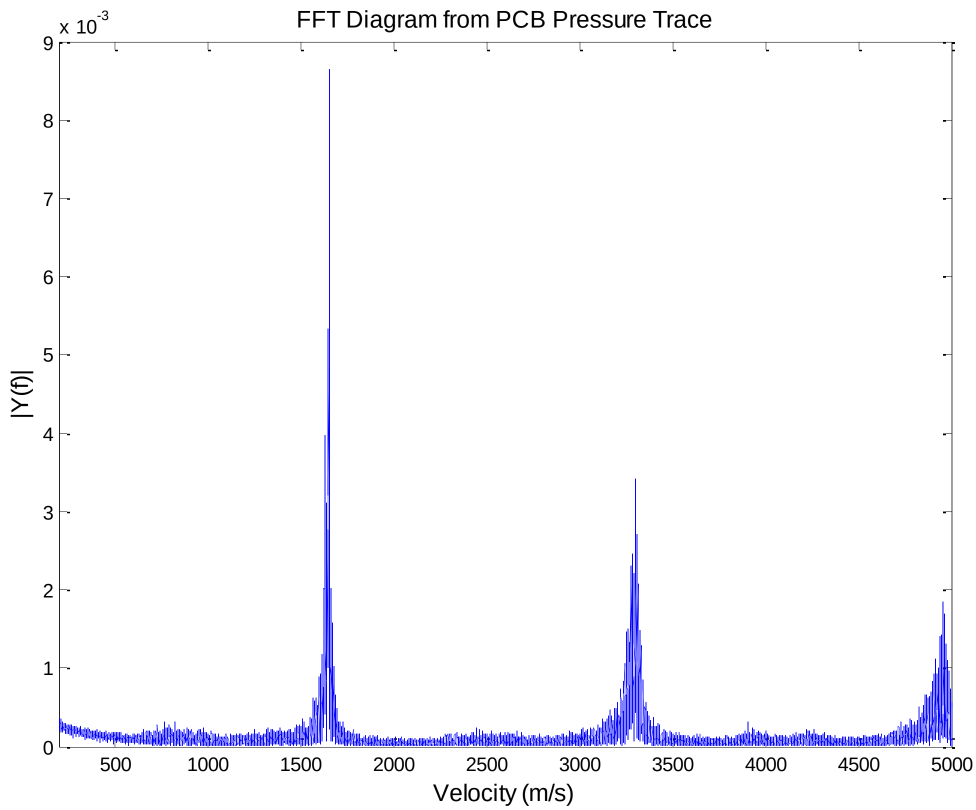

Figure 4.5: FFT plot of the pressure trace inside the detonation channel

Although the FFT proved to be a more accurate method for measuring the combustion wave speed, it only offered a significant improvement on a low percentage of the runs. This is demonstrated by the peak finding velocity being within 10% of the FFT velocity for 83% of the exclusively one wave runs. An example of an FFT plot for a typical run is shown in FIG. The magnitude of the frequency is located on the y-axis while the frequency on the x-axis has already been converted to the wave velocity from the engine's geometry. The primary frequency of the pressure trace is very clearly displayed at about 1650 meters per second, along with two of its harmonics at higher frequencies.

4.3: Uncertainty

Every measurement taken in an experiment has a certain level of uncertainty that affects the values reported from the experiment. The uncertainty of experimental values calculated from various experimental readings was determined by using Equation (4.12) (Figlioloa, 2006).

$$u_R = \pm\sqrt{\sum_{i=1}^{L}\left(\frac{\partial R}{\partial x_i}u_{x_i}\right)^2} \tag{4.12}$$

As mentioned previously, the mass flow of air and fuel into the engine were calculated by using Equation (4.1). Since the specific heats ratio γ and the specific gas constant R are constants, Equation (4.1) can be reduced to what is shown in Equation (4.13).

$$\dot{m} = \frac{p_0 A^*}{\sqrt{T_0}} c \tag{4.13}$$

The uncertainty in using Equation (4.13) to calculate the mass flow of air and fuel was determined by applying Equation (4.13) to Equation (4.12). Equation (4.14) is the result after the summation, and Equation (4.15) is the result after both the summation and the derivation.

$$u_{\dot{m}} = \sqrt{\left(\frac{\partial \dot{m}}{\partial p_0} u_{p_0}\right)^2 + \left(\frac{\partial \dot{m}}{\partial A} u_A\right)^2 + \left(\frac{\partial \dot{m}}{\partial T_0} u_{T_0}\right)^2} \tag{4.14}$$

$$u_{\dot{m}} = \sqrt{\left(\frac{Ac}{\sqrt{T_0}} u_{p_0}\right)^2 + \left(\frac{p_0 c}{\sqrt{T_0}} u_A\right)^2 + \left(-\frac{\mathrm{p_0 Ac}}{2\mathrm{T}_0^{1.5}} u_{T_0}\right)^2} \tag{4.15}$$

The uncertainty in the pressure measurements was ±2.0% of the full scale output of the pressure transducer (Omega Engineering). Since the pressure transducer for both the air and the fuel upstream of the sonic nozzles had full scale outputs of 2000 psig, a ±40 psi error was present on every pressure measurement. Since the average upstream air pressure was near 700 psig and the average upstream fuel pressure was near 500 psig, a ±40 psi error was usually the most significant error in the mass flow calculation. The uncertainty in the critical area of the sonic nozzle was calculated from Equation (4.16).

$$u_A = 1 - \frac{0.25\pi(d_{SN} - resolution)^2}{0.25\pi(d_{SN})^2} = 1 - \frac{(d_{SN} - resolution)^2}{(d_{SN})^2} \tag{4.16}$$

Equation (4.16) calculates the percent change in area from decreasing the nozzle diameter by the resolution of the diameter measurement. This uncertainty calculation uses a conservative approach by decreasing the nozzle diameter by the resolution, which gives a slightly larger uncertainty than increasing the nozzle diameter by a resolution. The inputs and results of Equation (4.16) are summarized in Table 4.1.

Supply Line	d_{SN} ***(in.)***	d_{SN} ***– resolution (in.)***	u_A
Fuel	0.125	0.124	1.594%
Air	0.252	0.254	0.792%
Air	0.315	0.314	0.634%

Table 4.1: Uncertainty of the sonic nozzle areas

A temperature of 290 K was used for all mass flow calculations since it was the ambient temperature in the test cell for the majority of the tests. The uncertainty for this value was set at 5% since the ambient temperature inside the cell was sometimes affected by unseasonably warm or cold weather days.

The experimental value of the pressure upstream of the sonic nozzle, the sonic nozzle area, and the temperature of the fluid were combined with their uncertainties and the constant in Equation (4.15) for each run. The uncertainty in the air mass flow reading ranged from 3.2% - 12.0%, and the uncertainty in the fuel mass flow reading ranged from 3.5% - 19.6%.

Once the uncertainty in the air mass flow and the fuel mass flow was determined for each run, the uncertainty of the total mass flow and the stoichiometric mixture could be determined as well. Since the total mass flow is equal to the summation of the air flow and the fuel flow, the uncertainty in the measurement of the total mass flow is the square root of the summation of the uncertainty in the air mass flow squared and the uncertainty in the fuel mass flow squared, as shown in Equation (4.17). The uncertainty in the total mass flow ranged from 3.1% - 11.4%.

$$u_{\dot{m}_{total}} = \sqrt{\left(u_{\dot{m}_{air}}\right)^2 + \left(u_{\dot{m}_{fuel}}\right)^2} \tag{4.17}$$

The equivalence ratio was calculated by using Equation (4.2). Since the denominator of the equation is a constant based on the fuel and oxidizer used in the experiment, it can be expressed as a constant. The uncertainty in the equivalence ratio calculation was determined by applying Equation (4.2) to Equation (4.12), which results in Equation (4.18). The uncertainty in the stoichiometric ratio ranged from 5.2% - 22.3%.

$$u_\phi = \sqrt{\left(\frac{1}{\dot{m}_{air}c} u_{\dot{m}_{fuel}}\right)^2 + \left(-\frac{\dot{m}_{fuel}}{\dot{m}_{air}^2 c} u_{\dot{m}_{air}}\right)^2} \tag{4.18}$$

The air and fuel flow thrust, the detonation thrust, and the gross thrust were all measured by the load cell. Since the uncertainty in the load cell's measurement was very low at 0.14% (Honeywell International), only the error from the averaging process shown in Figure 4.1 was used for determining the uncertainty in the thrust results. The equation for the uncertainty in the thrust measurement was also found by applying Equations (4.4), (4.5), and (4.6), to Equation (4.12). The resulting uncertainty equations are shown in Equations (4.19), (4.20), and (4.21).

$$u_{Gross\ Thrust} = \sqrt{\left(u_{\overline{Region\ 4}}\right)^2 + \left(-u_{\overline{Region\ 1}}\right)^2} \tag{4.19}$$

$$u_{Det\ Thrust} = \sqrt{\left(u_{\overline{Region\ 4}}\right)^2 + \left(-u_{\overline{Region\ 3}}\right)^2} \tag{4.20}$$

$$u_{Flow\ Thrust} = \sqrt{\left(u_{\overline{Region\ 3}}\right)^2 + \left(-u_{\overline{Region\ 1}}\right)^2} \tag{4.21}$$

The uncertainty for each load cell region was determined by applying a 95% confidence interval to the data. This confidence interval was found by calculating the standard deviation of the averaged data, then adding and subtracting two times the standard deviation from the average value. (Figlioloa, 2006). Although this method is a very conservative approach since it is intended for determining the how far from the original average 95% of any additional points will fall instead of how far the average of any additional points will be from the original average, it provides an uncertainty for a worst-case scenario. The uncertainty in the detonation thrust ranged from 8.1% - 139.3%. The extremely high uncertainties were observed for runs that had very low thrust, and the low uncertainties were observed for runs that had high thrust, as shown in Figure 4.6. This trend occurred because the thrust was determined by subtracting two average values of the load cell, and the difference in the two average values decreased much more rapidly than the magnitude (and therefore the uncertainty) of the two averages.

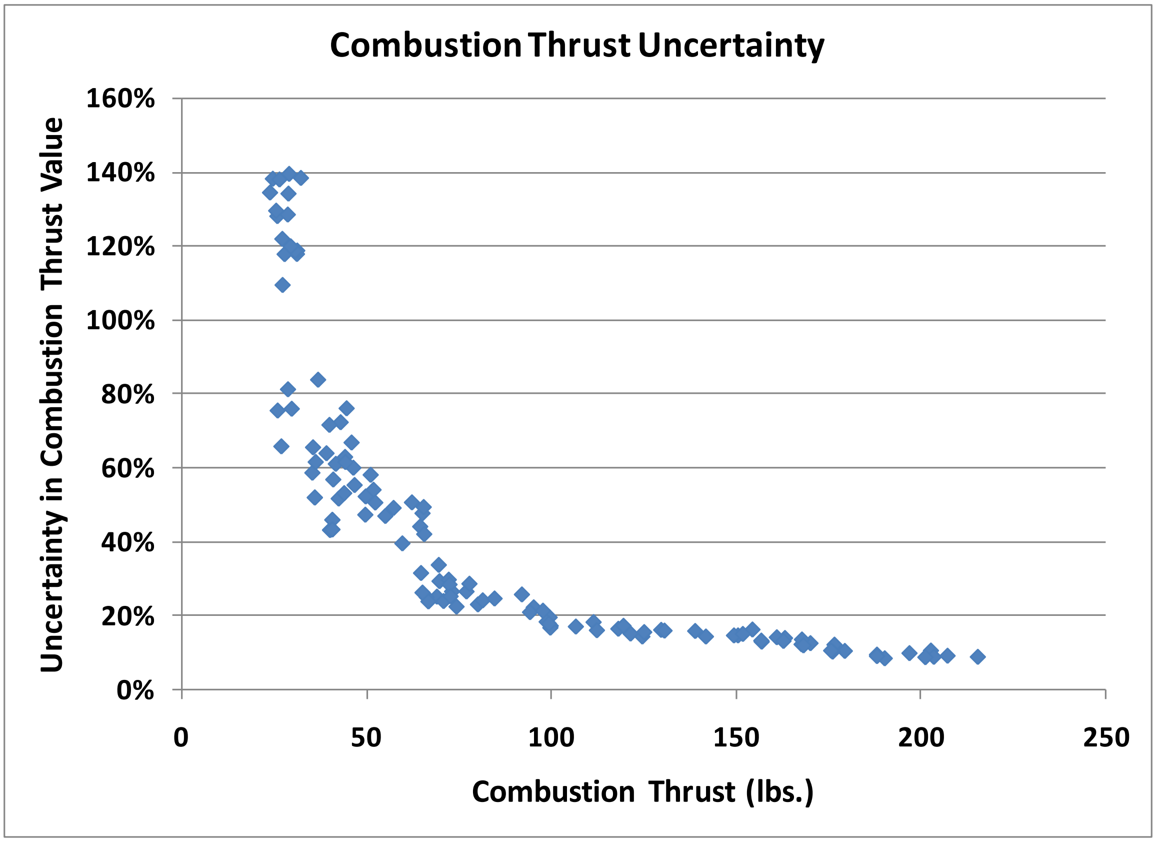

Figure 4.6: Combustion thrust uncertainty

Chapter 5: Results and Conclusions

5.1: Operating Space

The first step in the study of any novel engine is to determine at which conditions the engine operates. Unfortunately, an operational run is not simple to define for a rotating detonation engine. This definition is difficult because the engine experienced a slow degradation of the detonation wave as it reached the fringe of the operating region, as will be shown in the following results. In order to define the operating space properly, a certain criterion had to be in place to separate detonating, non-detonating, and non-operational runs. The criterion used for a successful detonation run was having the engine contain a combustion wave front from ignition to fuel shutoff with a velocity greater than 1,100 m/s. This wave speed was shown to be the minimum velocity of detonations inside an RDE by Bykovskii's studies on hydrogen-air mixtures (Bykovskii, 2006). A non-detonating run was defined as a combustion wave that propagated through the engine during the entire run, but did not meet the wave velocity requirement. The last run type was a non-operational run. A non-operational run either combusted almost exclusively outside of the engine's detonation channel, or did not combust at all. A combusting non-operational run was easily detected by the height of the exhaust plume exiting the RDE. When the ratio of the height of the exhaust plume to the diameter of the engine was approximately 3:1, as shown in Figure 5.1, this indicated that the combustion of the fuel-air mixture was primarily occurring inside of the engine. When the ratio of the exhaust plume to the diameter of the engine was 10:1 or more, this indicated that the combustion of the fuel-air mixture was almost exclusively occurring outside of the engine. Although the tester always used pressure transducers placed in the detonation channel to ensure if the run combusted externally or internally, this simple visual test was a very helpful indicator.

Figure 5.1: Side view image of the exhaust plume of a successful detonating run without any external light sources

The detonating and non-detonating test runs of hydrogen and atmospheric air (21% $O2$, 78% $N2$, 1% Ar) that used PCB pressure sensors to measure the wave activity for a given engine configuration (6mm detonation channel width and 0.123 in^2 gross oxidizer injector area) are shown in Figure 5.2. Figure 5.2 shows the test runs by displaying the air mass flow into the engine in pounds per minute on the y-axis and the equivalence ratio on the x-axis.

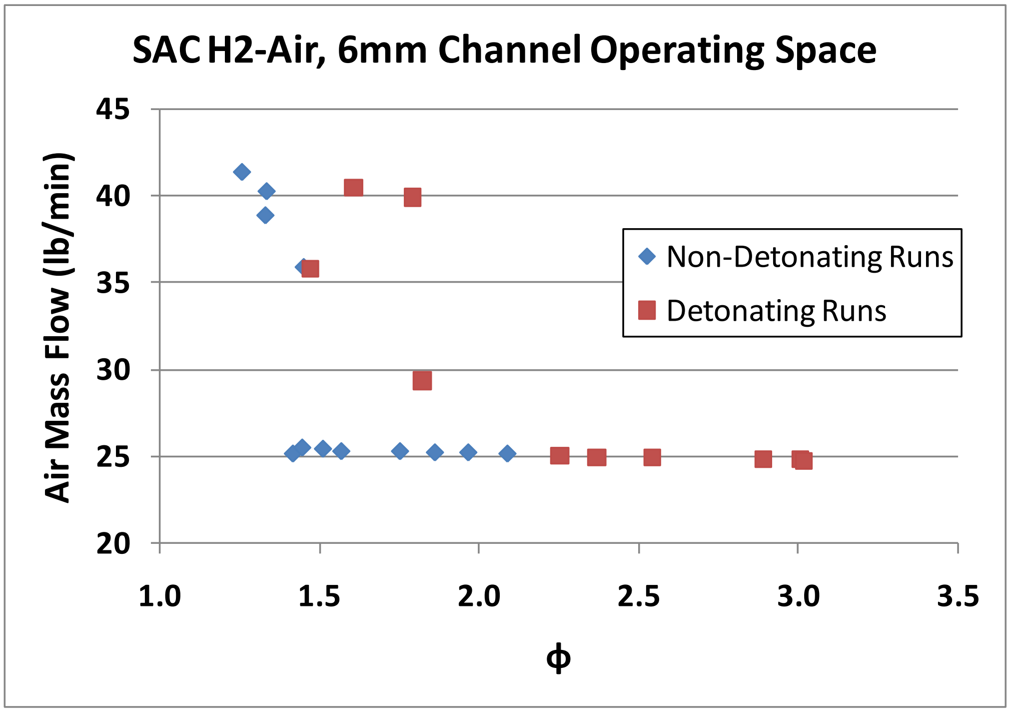

Figure 5.2: RDE operating range for hydrogen-air with 6mm channel and 0.123 in^2 gross oxidizer injection area

Although Figure 5.2 presents the operational space for the given engine configuration in a typical format, these data sets present a much more interesting trend when they are plotted with air mass flow in pounds per minute as a function of fuel mass flow in pounds per minute. This representation of the data is shown in Figure 5.3. Figure

5.3 shows that a hydrogen mass flow rate of 1.55 pounds per minute separates the non-detonating runs with lower hydrogen mass flow rates from the detonating runs with higher hydrogen mass flow rates.

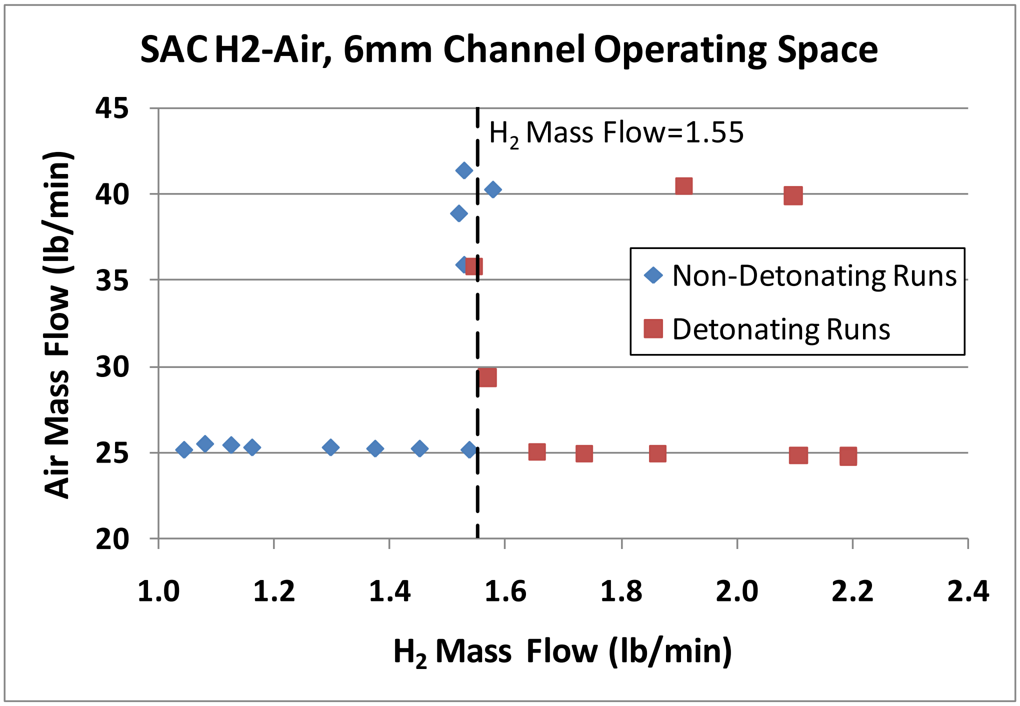

Figure 5.3: RDE operating range for hydrogen-air with 6mm channel and 0.123 in^2 gross oxidizer injection area with a defined transition

This result of a hydrogen flow rate value that separates non-detonating runs from detonating runs was very important for obtaining additional data points for the operating space of the RDE on hydrogen-air. The transition hydrogen flow rate was used to determine if the hydrogen-air tests that contained mass flow measurements but not pressure measurements in the detonation channel were non-detonating or detonating runs.

The visual inspection method and the overhead camera were used to ensure that the combustion process for these runs was predominantly inside the channel, but without channel pressure measurements the velocity of the run could not be determined through an FFT or peak finding processes.

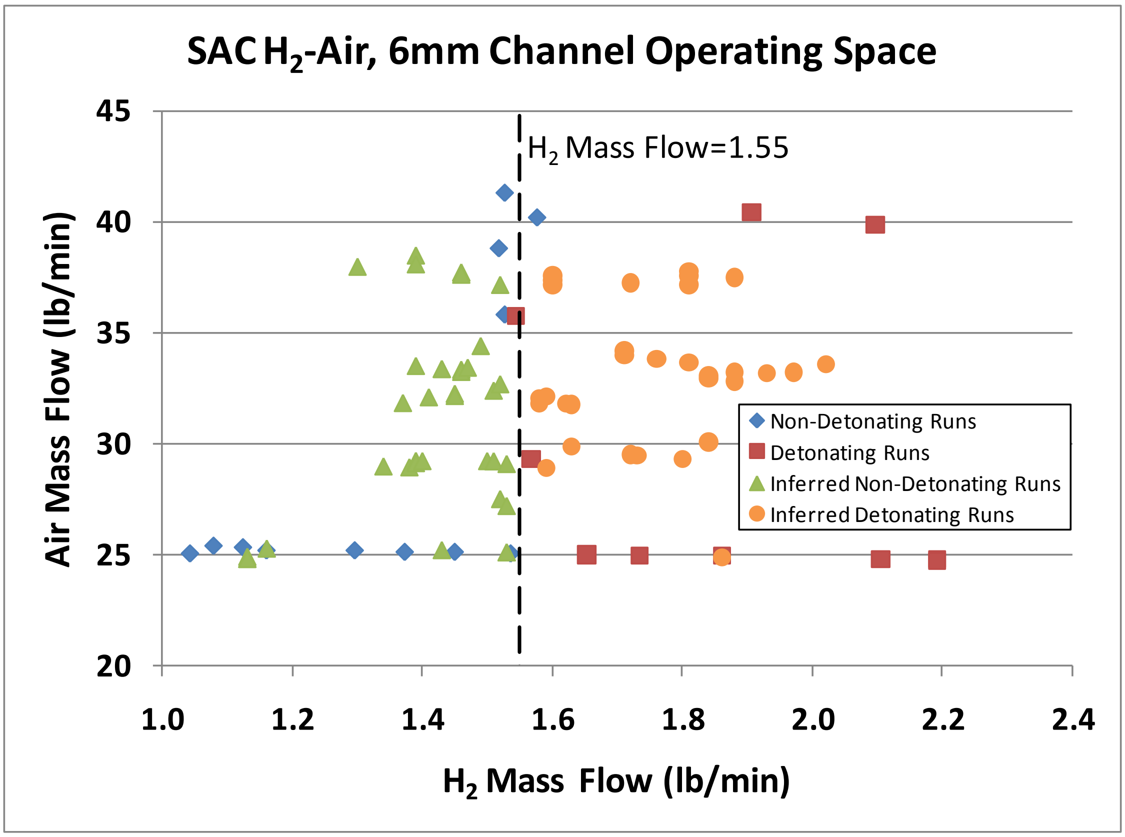

Figure 5.4: RDE operating range for hydrogen-air with 6mm channel and 0.123 in^2 gross oxidizer injection area with a defined transition and inferred runs

However, as is shown in the plot of air mass flow in pounds per minute as a function of hydrogen mass flow in pounds per minute in Figure 5.4, the hydrogen flow rate value obtained by the results of Figure 5.3 was used to separate the runs without channel pressure data into non-detonating and detonating runs. All of these runs that had a fuel mass flow rate of less than 1.55 lb/min were considered "Inferred Non-Detonating Runs" and all of these runs that had a fuel mass flow rate above 1.55 lb/min were considered "Inferred Detonating Runs." This procedure culminates in a final plot of air mass flow in pounds per minute as a function of the equivalence ratio of all the hydrogen-air detonating runs in Figure 5.5.

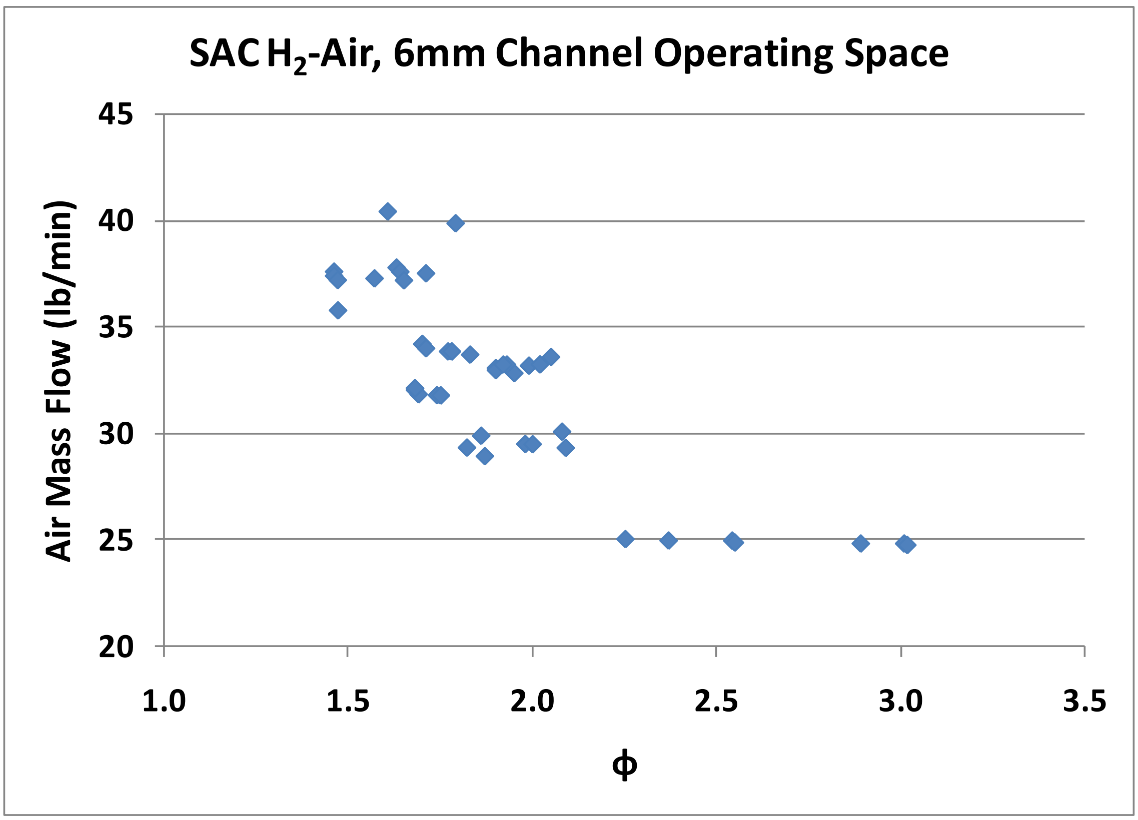

Figure 5.5: Final RDE operating range for hydrogen-air with 6mm channel and 0.123 in^2 gross oxidizer injection area

The method used for adding runs without channel pressure data to the hydrogen-air operating space was also used for the operating spaces of the two other hydrogen-oxidizer combinations. The operating spaces of the three oxidizers are shown together on a plot of air mass flow in pounds per minute as a function of the equivalence ratio in Figure 5.6.

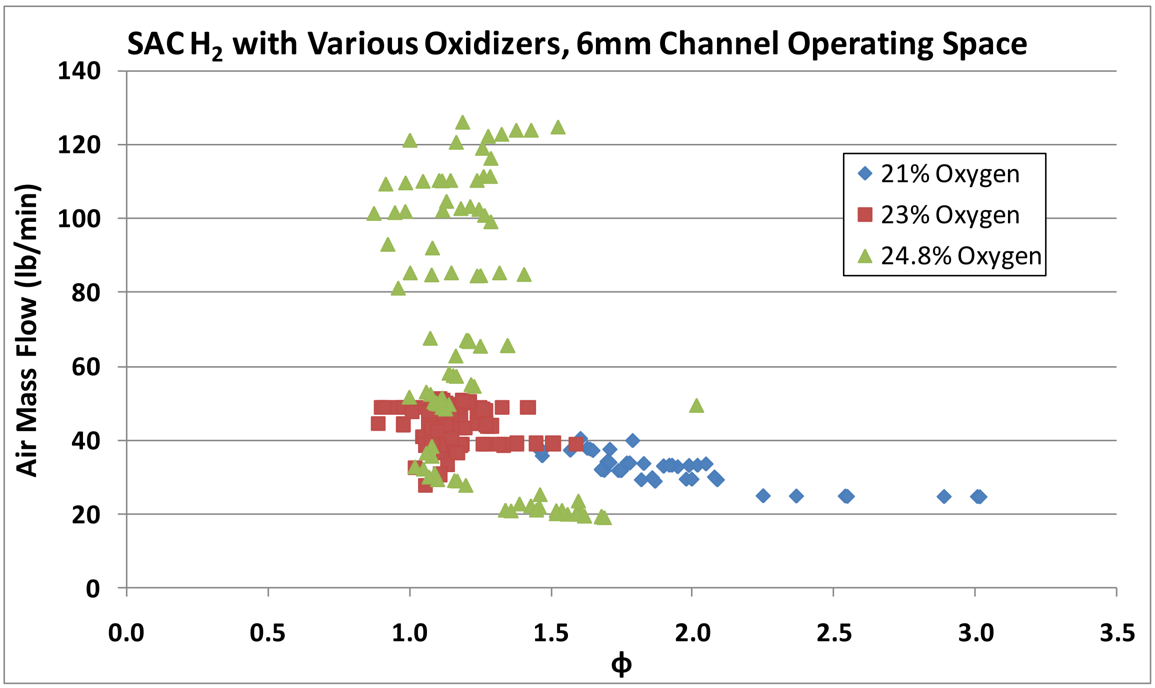

Figure 5.6: RDE operating space for hydrogen and various oxidizers with a 6mm channel

The most obvious and important aspect of Figure 5.6 is the large increase in the greatest air mass flow rate that could successfully detonate as the oxygen concentration in the oxidizer increased. This increase in the upper air mass flow limit allows for more thrust to be generated by the engine, and allows for a wider range of thrust output for throttling. Although the upper air mass flow limit and its effect on the thrust output was the largest change to the operating space with more oxygen in the oxidizer, the engine was able to detonate at lower air mass flow rates and leaner mixtures as well. It is important to note that the richest runs conducted with 23% and 24.8% oxygen were not the rich limit of these oxidizers, these were just the richest mixtures that were tested since the rich limit was not determined for these oxidizers. It is probable that the rich limits would increase with oxygen concentration along with the other limits of the operational space, but this was not determined during the scope of the experiments. Overall, the increase in oxygen in the oxidizer created a more reactive mixture in the engine that greatly increased the operating range of the RDE.

5.2: Thrust

The thrust generated by the engine was determined by a load cell mounted under the bottom of the engine. The thrust generated by the detonation was measured by subtracting the difference between the average reading of the load cell with both the fuel and the air flowing through the engine prior to ignition, and the average reading of the load cell while the engine was operating, as was shown in Figure 4.1.

The amount of thrust generated by the engine generally increased as the amount reactants flowing into the engine increased. Since this engine always used hydrogen for fuel and 21%O_2-78%N_2-1%Ar, 23%O_2-77%N_2, or 24.8%O_2-75.2%N_2 for the oxidizer, in order to achieve a stoichiometric mixture of fuel and air, the ratio of air mass flow to fuel mass flow needed to be 34, 31, and 29, respectively. Due to the air mass flow being such a great percentage of the total mass flow, the performance of the engine as the total mass flow varied was almost identical to the performance of the engine as the air mass flow was varied.

One of the most interesting thrust relationships observed during testing was the thrust output of the engine for detonating and non-detonating runs. Figure 5.7 plots the thrust in pounds as a function of the air mass flow rate in pounds per minute for both detonating and non-detonating runs conducted with a hydrogen-air mixture. The data in this plot show a linear increase in thrust output with an increase in air mass flow, regardless of the type of combustion wave that is propagating through the engine.

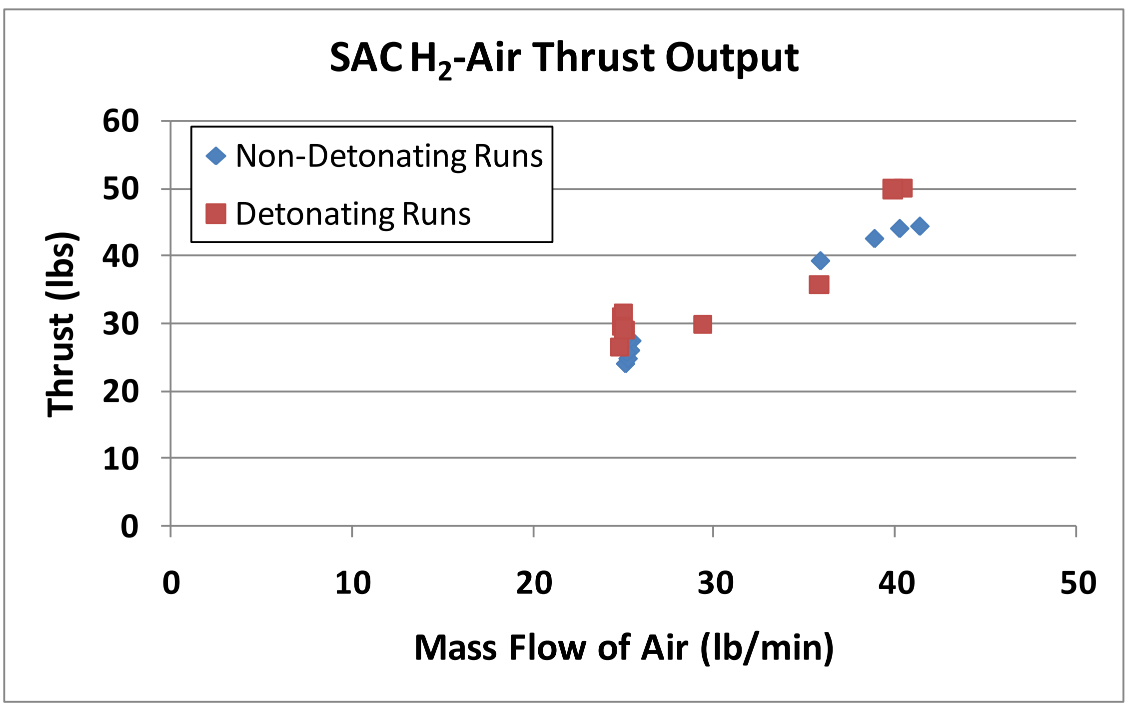

Figure 5.7: Thrust of detonating and non-detonating runs

Since the increase in the flow of air shown in Figure 5.7 was accomplished by increasing the upstream pressure of the air and therefore the pressure in the oxidizer manifold, it was important to investigate if the increase in the thrust from the combustion process was due to the increase in air flow or the increase in the oxidizer manifold pressure. This question is addressed by the data in Figure 5.8, which shows the thrust in pounds and the oxidizer injection pressure in absolute pounds per square inch as a function of air mass flow into the engine in pounds per minute.

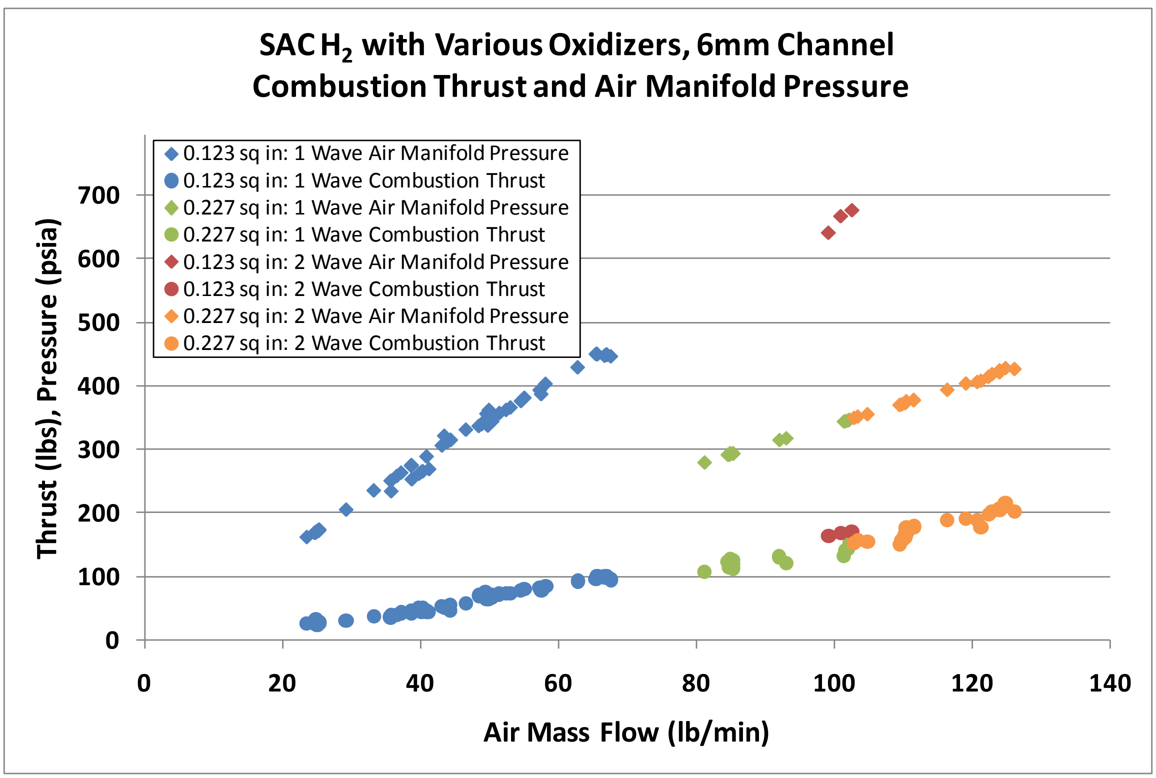

Figure 5.8: Combustion thrust for varying air injection pressures

Figure 5.8 shows that when the air mass flow into the engine was maintained (the fuel mass flow and equivalence ratio were kept within 5%) but the gross oxidizer injector area was roughly halved from 0.227 in^2 to 0.123 in^2, the oxidizer injection pressure increased by 80-90%, but only resulted in 10-15% greater thrust output from the combustion process. This result shows that the increased injection pressures seen at higher flow rates from increasing the upstream pressure do not significantly contribute to the increase in thrust. This result is important for engine analysis because it shows that the thrust output of the RDE is only weakly dependent on the injection pressure, and much more strongly dependent on the flows of the reactants. This result is also very important to laboratory work as it is much easier to change the amount of flow into the engine by varying the upstream pressures with the same area restrictions between tests than maintaining the upstream pressures and varying the area restrictions in the flow path between tests.

Although the thrust increases with air mass flow, it appears that the exclusively one wave data just prior to the establishment of two waves underperforms in thrust output. This result could have occurred from the engine containing less stable combustion wave fronts in the region just prior to the onset of two wave activity. If this is the case, then the thrust generated during the steady one wave region could anticipate the thrust during the two wave region. A plot of the combustion thrust in pounds as a function of the air mass flow rate in pounds per minute is shown in Figure 5.9, where a number of different types of curve fits were applied to the steady one wave data and extrapolated so they could be compared to the two wave data.

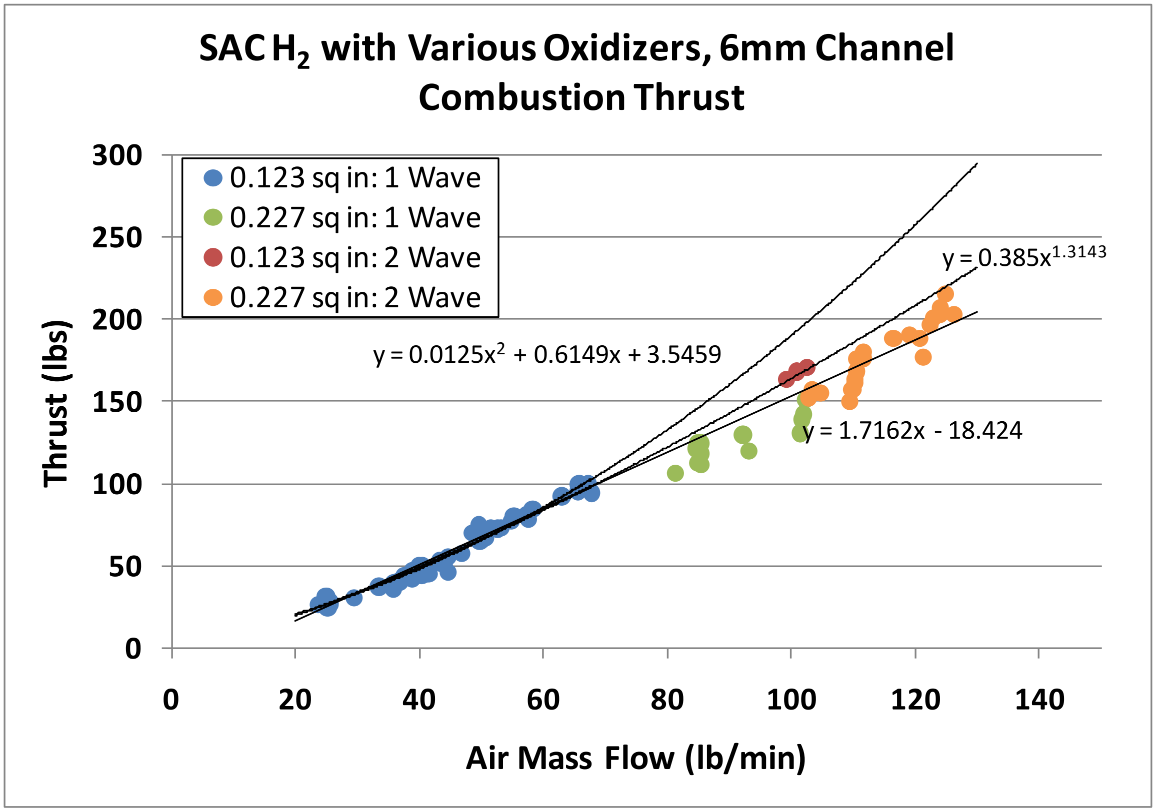

Figure 5.9: Various curve fits for detonation thrust data

The linear trendline in Figure 5.9 estimates thrust values far below the experimental values for the 0.123 in^2 two wave data, then intersects and falls below the thrust values for the 0.227 in^2 two wave data. The linear trendline does not appear to grow quickly enough to accurately model the data. The second order polynomial trendline estimates greater thrust than the experimental value for the 0.123 in^2 two wave data and overall appears to grow too quickly. However, the power trend passes within 3% of all 0.123 in^2 two wave data points and remains about 10% above the experimental thrust for the 0.227 in^2 data, which is almost the identical percentage difference between the experimental 0.123 in^2 and 0.227 in^2 data shown in Figure 5.8.

Now that the thrust has been shown to increase with the mass flow rate of air, the next step is to investigate how the thrust changes with the mass flow of fuel. In Figure 5.10 the thrust output of the engine is plotted as a function of the mass flow of fuel.

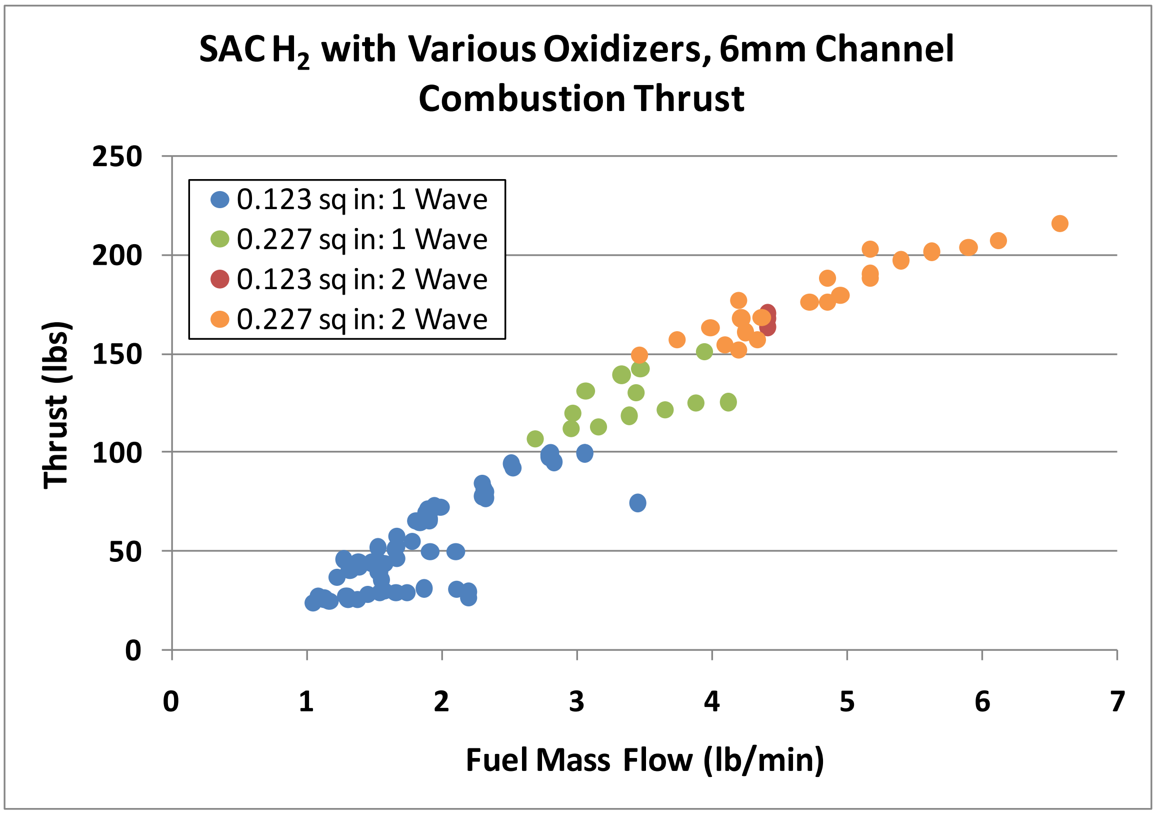

Figure 5.10: Thrust as a function of fuel mass flow

Although Figure 5.10 shows an increase in thrust as the fuel flow is increased, most of this increase is due to the increased air flow that is necessary at the higher fuel flows to achieve a detonable mixture. This is particularly noticeable where the data points form very slightly positive sloped lines. These lines are groups of data where the air mass flow was held relatively constant but the fuel mass flow was increased, resulting in very modest gains in thrust. Therefore, in order to determine the effect of increased fuel flow on the thrust, a plot of thrust as a function of fuel flow while holding air flow constant must be used. In the thrust versus fuel flow graph shown in Figure 5.11, each series is grouped by the oxidizer used, and then by runs where the range of air mass flows had less than a 5% change from the minimum to maximum air flow.

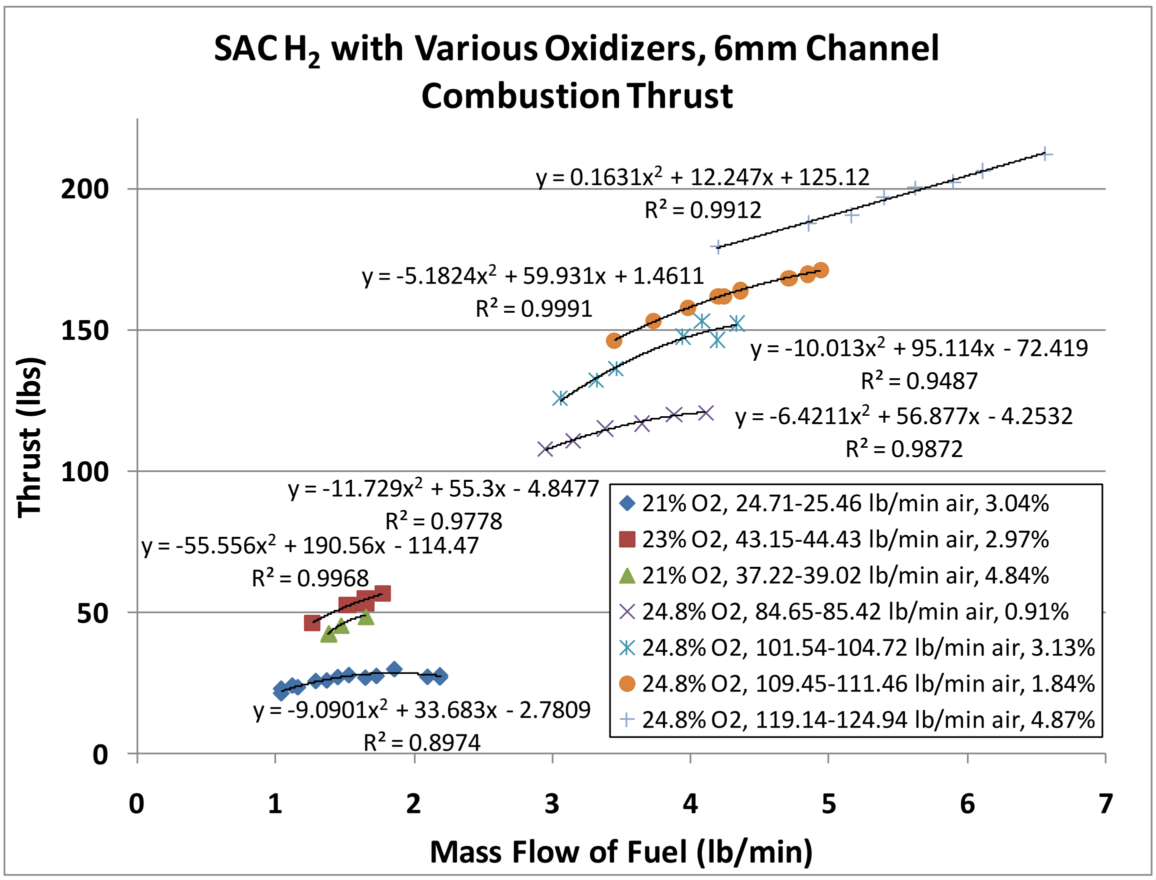

Figure 5.11: Thrust as a function of fuel mass flow at constant air mass flows

Each group is identified by the oxidizer used, the range of air mass flows used in the group, and the percentage difference in the air mass flow range. A minimum of three data points were required to make a data set. The data in Figure 5.11 show that the thrust of the engine increases with increases in fuel mass flow, but with diminishing returns. This is evident in each data set as they each follow a second order polynomial trend with a negative second derivative, with the exception of the 24.8% oxygen, 119.14-124.94 lb/min air, 4.87% data set. In particular, the thrust of the 21% oxygen, 24.71-25.46 lb/min air, 3.04% data set reaches a fuel flow rate where the thrust begins to decrease as more fuel is added. However, the three runs beyond this fuel flow rate had extremely rich equivalence ratios of 2.89, 3.01, and 3.01. These three runs appear to be past the region where the extra thrust provided by additional fuel could make up for the decrease in combustion efficiency that occurs in non-stoichiometric mixtures. The average thrust per pound of fuel added was found by averaging the average slope of each second order polynomial curve fit over the range of fuel flows tested. This calculation yielded an average increase of 15.6 lbs of thrust for an additional lb/min of fuel added.

After the relationship of thrust to fuel flow with relatively constant air flow has been established, the relationship of thrust to air flow with relatively constant fuel flow was investigated. The analysis was done is a similar way to the fuel flow; groups of thrust data for a given oxidizer where the fuel mass flow varied less than 5% from the minimum to the maximum value were used, with a minimum of three points needed to make a data set. The groups were identified by the oxidizer used, the range of fuel mass flows in the group, and the percentage difference in the fuel mass flow range. In order to make the multiple series of data easier to visualize, the plots were broken up into air flows less than 75 lb/min in Figure 5.12 and greater than 75 lb/min in Figure 5.13.

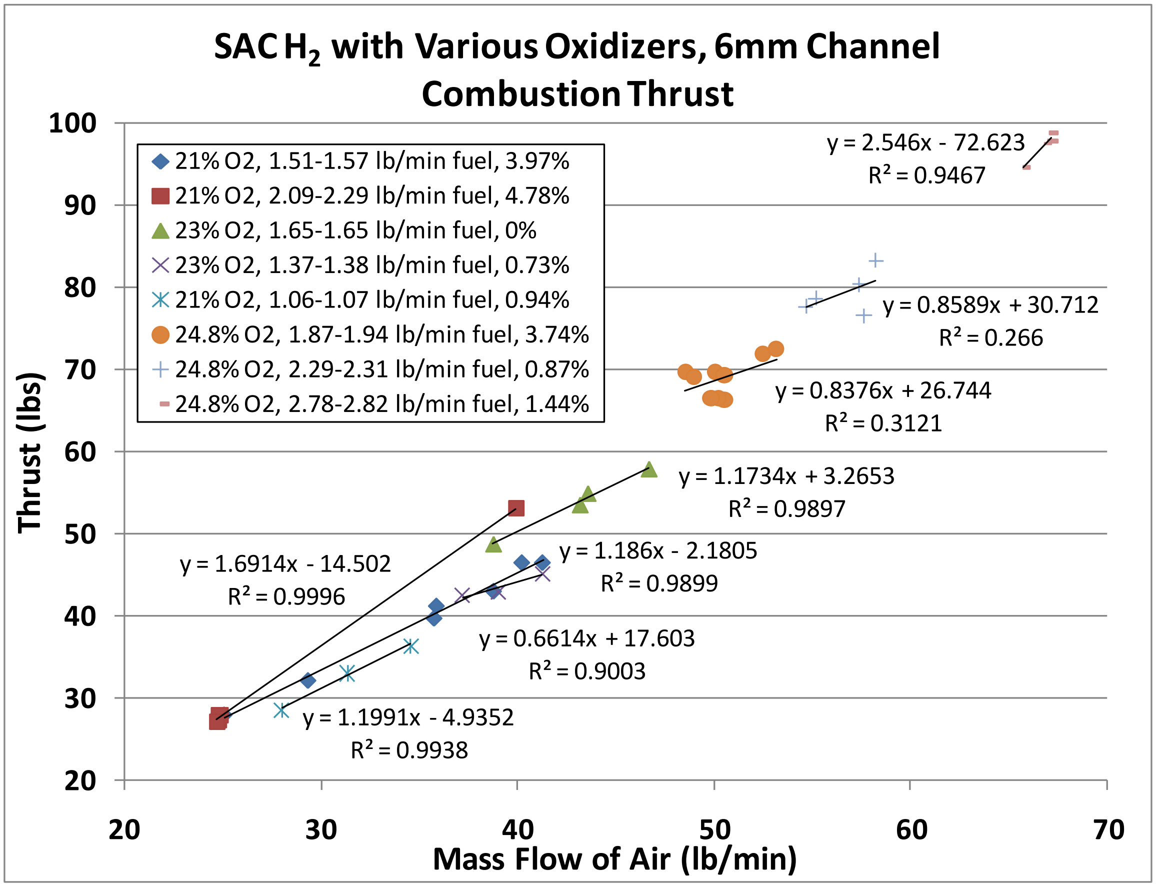

Figure 5.12: Thrust vs air mass flows less than 75 lb/min at constant fuel mass flows

Most of the trends in Figure 5.12 and Figure 5.13 did not contain enough data points to determine if they followed a second order polynomial trend, but the slopes of the linear fits of the points still provide insight into the relationship between the thrust and the mass flow of air. The average additional thrust per pound of air added was calculated by taking the average of the slopes of the linear fits of each data series. This calculation yielded an average increase of 1.5 lbs of thrust for an additional lb/min of air added. Although each additional lb/min of air added to the engine had only 10% of the increase in thrust as each additional lb/min of fuel added, with the stoichiometric air/fuel mass ratios between 29 and 34 for the configurations tested, if greater total mass flow mixtures are nearly stoichiometric, then the increase in air mass flow would account for 65-70% of the increased thrust.

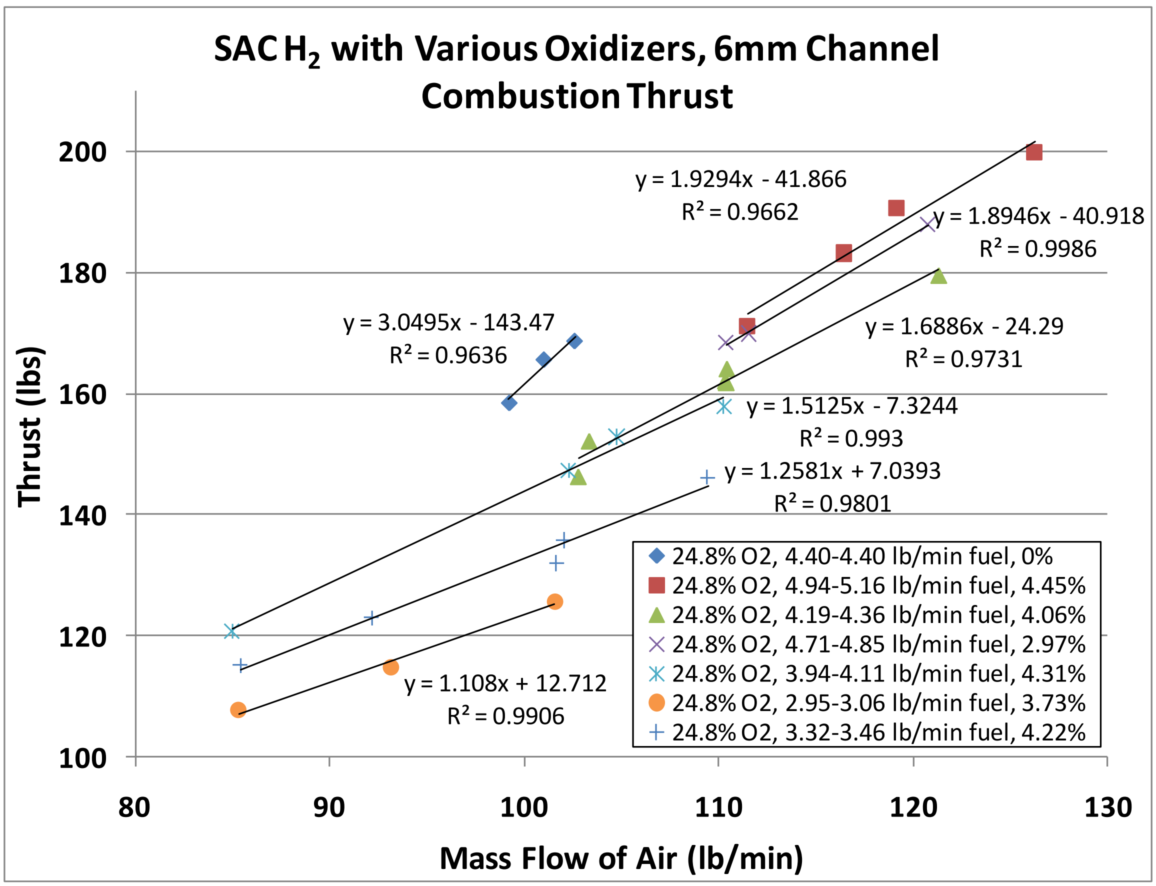

Figure 5.13: Thrust vs air mass flows greater than 70 lb/min at constant fuel mass flows

As was shown in Figure 4.1, the air and the fuel flow through the engine exerted a thrust reading on the load cell during the air and fuel establishing time prior to ignition and thrust from the combustion. This reading, the "Air and Fuel Flow Thrust", was a significant portion of the thrust output of the engine at lower air mass flows, contributing to 70% or more of the gross thrust. The flow thrust increased in magnitude with increases in air mass flow, but at a slower rate than the thrust generated by the combustion process.

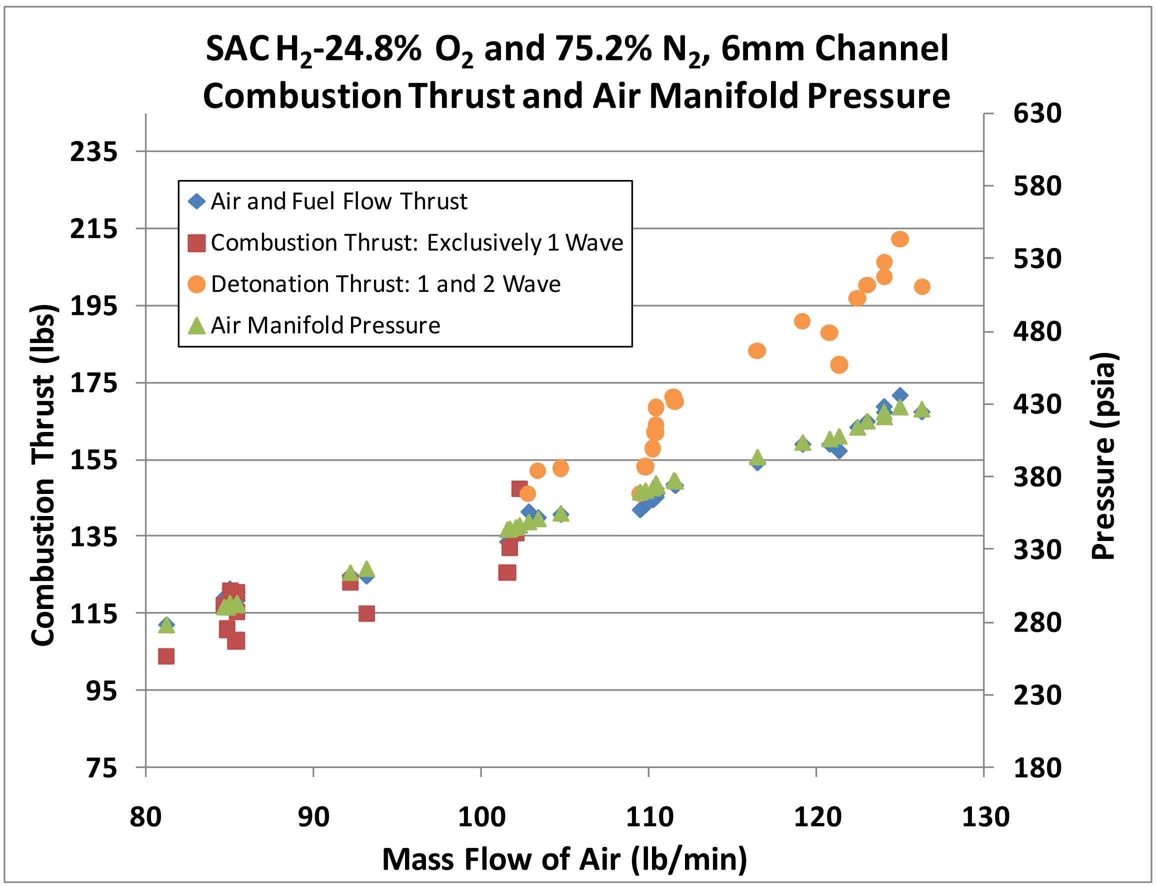

Figure 5.14: Combustion thrust for one and two detonation wave regions

The plot shown in Figure 5.14 of thrust in pounds on the left y-axis and pressure in absolute pounds per square inch on the right y-axis as a function of air mass flow in pounds per minute show that the flow thrust was not overtaken by the thrust generated by the combustion process until the engine began containing two detonation waves in the engine.

5.3: Specific Impulse

One of the most important quantities describing the operation of an engine since it has efficiency implications. The specific impulse is defined as the gross thrust generated by the engine divided by the weight of fuel being consumed by the engine to produce the thrust (Equation (5.1)). Since this equation is the ratio of what the engine is designed to do (create thrust) divided by what must be supplied to operate the engine (fuel), the larger the ratio between the engine output and the fuel used, the greater the efficiency of the engine.

$$SI = \frac{Gross\ Thrust}{\dot{m}_{Fuel}g} \tag{5.1}$$

Initially it may seem from the terms in Equation (5.1) that the best way to increase the specific impulse would be to find the point of engine operation where the fuel mass flow is at a minimum. However, when the plot of specific impulse versus mass flow of fuel is examined as in Figure 5.15, the lowest fuel flow rate of 0.93 lbs/min has a specific impulse of 2,376 s, which is 40% less than the highest specific impulse of 4,033 s. In addition, the point with the highest specific impulse had a fuel flow rate 270% higher at 3.45 lbs/min.

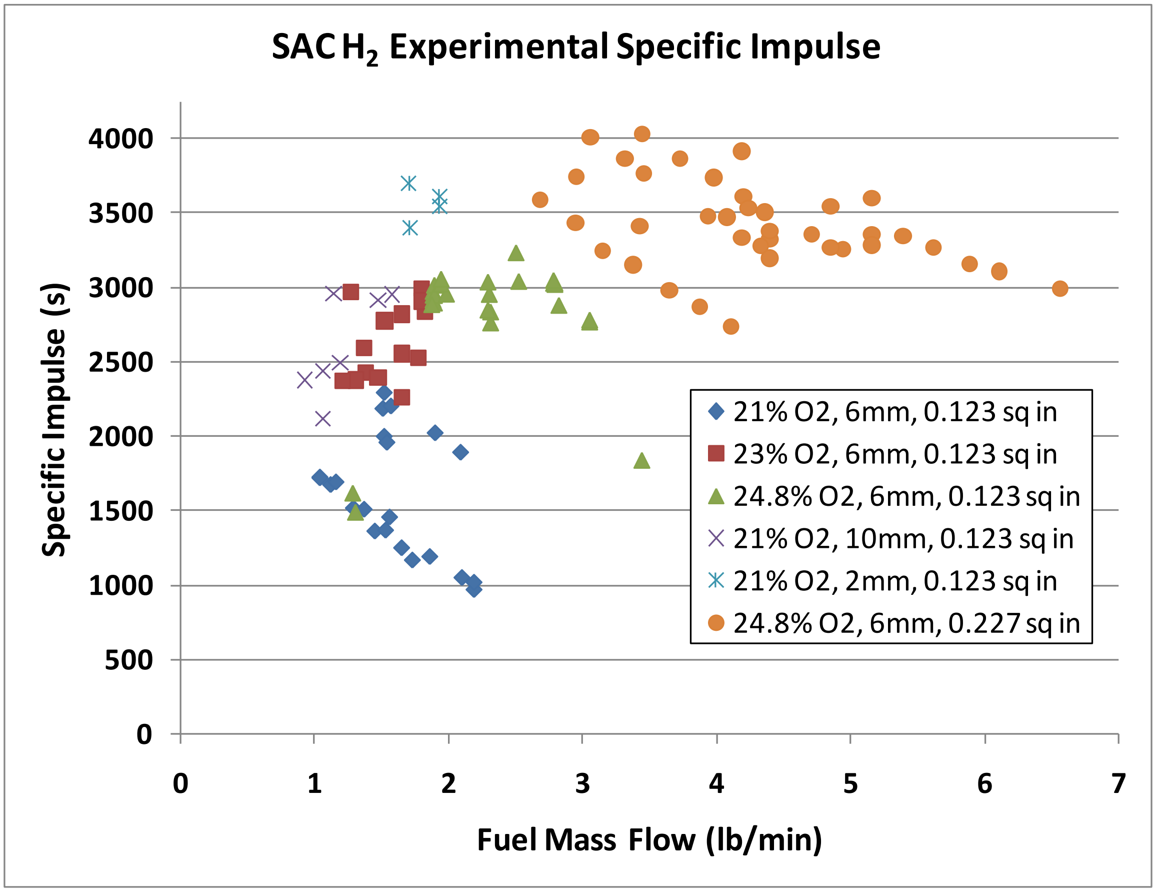

Figure 5.15: Specific impulse as a function of mass flow of fuel

The engine will maximize the value of the specific impulse when the ratio of thrust to fuel flow is at a maximum. Since the thrust generated by the engine increases as air flow increases, the greatest values of specific impulse occur when the ratio of air flow to fuel flow is at a maximum, or when the equivalence ratio is at a minimum. Figure 5.16 shows that for every engine configuration tested, the specific impulse increased as the global equivalence ratio of the reactants entering the engine decreased. This result is not surprising, as the engine will have the best thrust to fuel flow ratio when the equivalence ratio is at the lowest value where the engine operates properly.

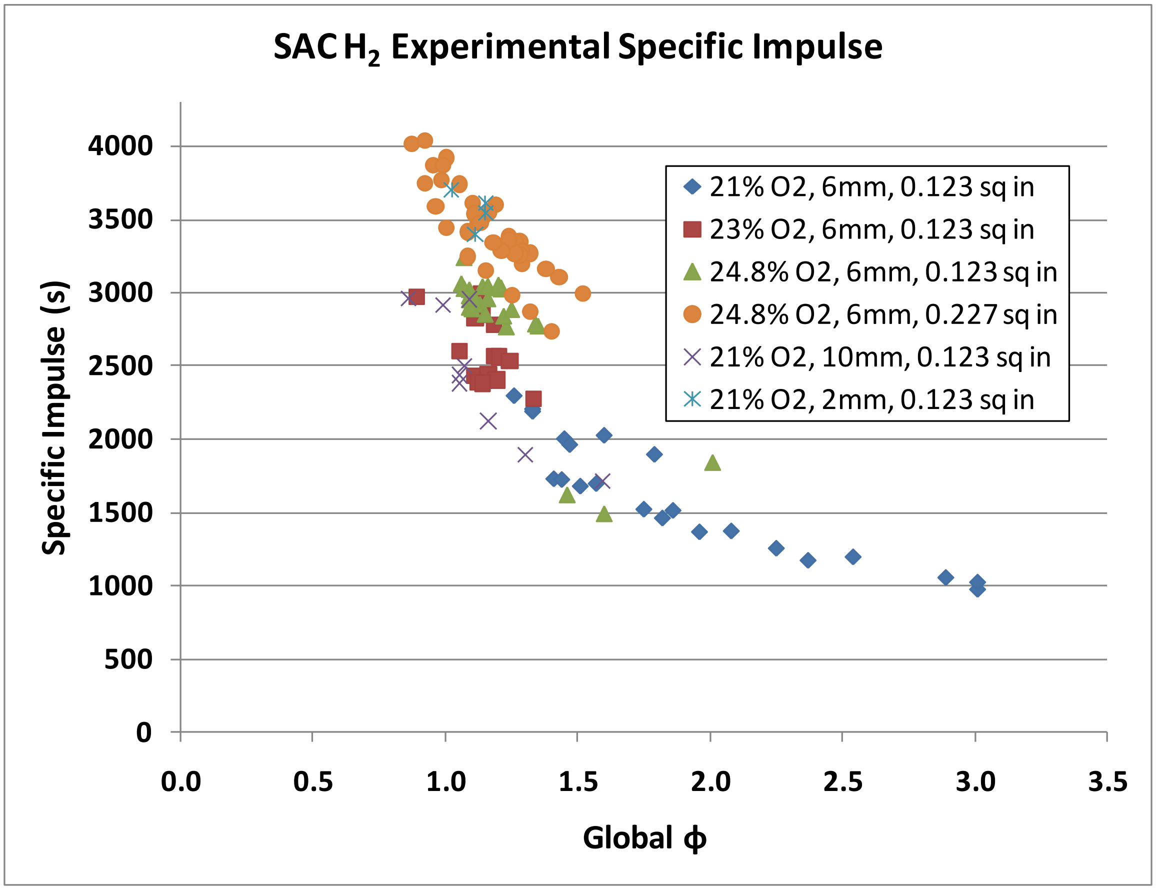

Figure 5.16: Specific impulse as a function of equivalence ratio

The properties behind Equation (5.1) and the results in Figure 5.16 show that the specific impulse is inversely proportional to the equivalence ratio of reactants entering the engine. Indeed, if the specific impulse is plotted as a function of the reciprocal of the equivalence ratio, the direct linear relationship between the two variables is immediately apparent. Although the specific impulse increases while the equivalence ratio decreases in Figure 5.16, a wide range of specific impulses occurs for similar equivalence ratios in the slightly rich region. This phenomenon was further investigated by plotting the specific impulse as a function of the air mass flow rate in pounds per minute in Figure 5.17 with the same test runs shown in Figure 5.16. Figure 5.17 shows that the specific impulse increases with the air mass flow rate in addition to its inverse relationship with the equivalence ratio shown in Figure 5.16.

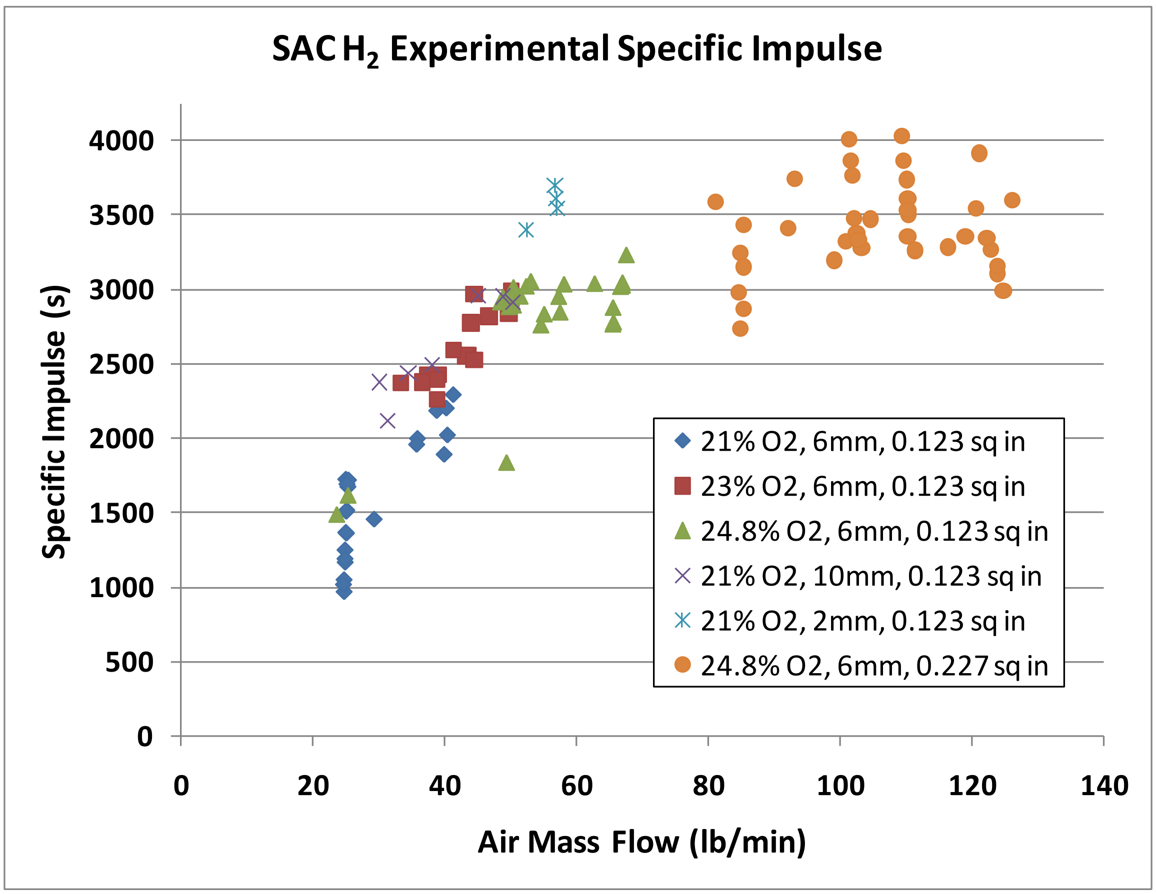

Figure 5.17: Specific impulse as a function of the air mass flow rate

The specific impulse results presented in Figure 5.16 were compared to the analytical calculations for a detonation engine performed by Joe Shepherd (Shepherd, 2000) in Figure 5.18. The original experimental data and the original analytical Shepherd calculation are shown in black, while a factor of 1.35 increase in the equivalence ratio of the experimental data and a factor of 0.75 decrease in the specific impulse of the analytical calculation are shown in gray.

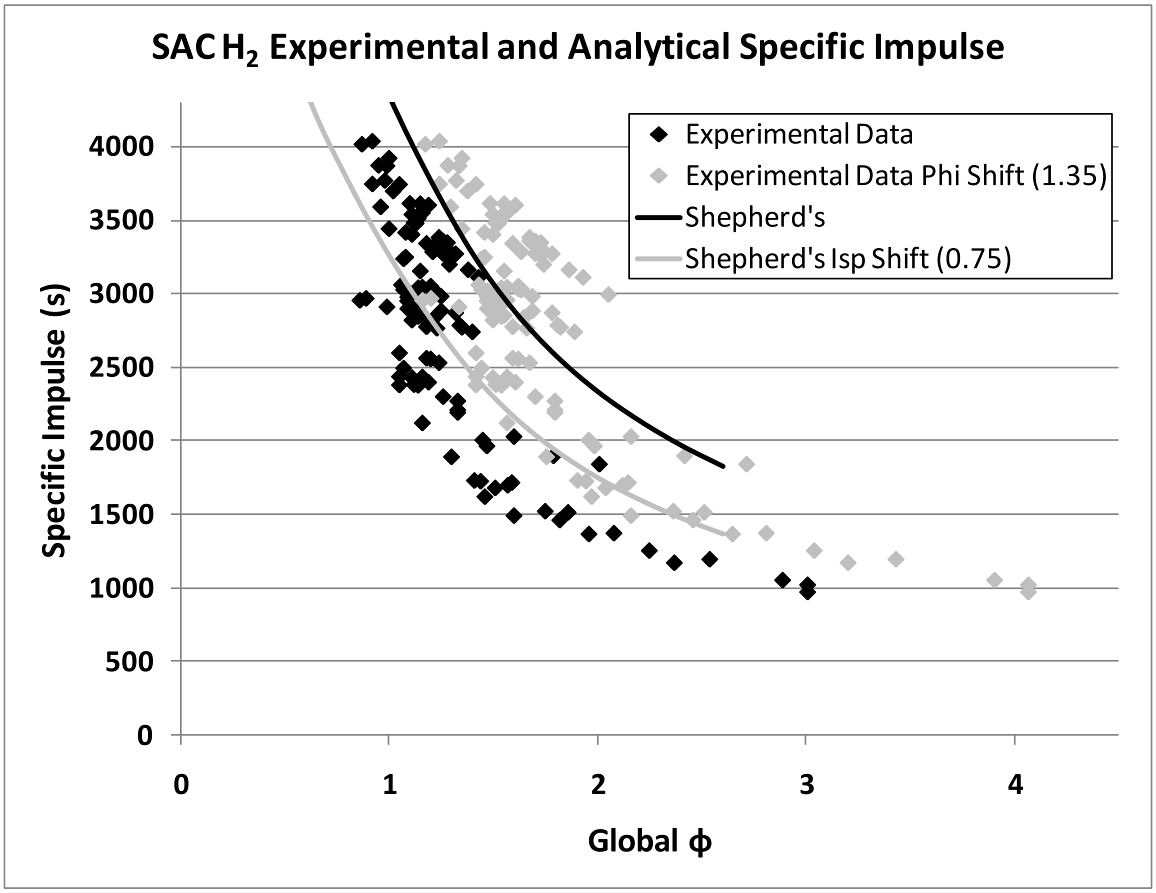

Figure 5.18: Comparison of experimental and analytical specific impulse results

These shifts in the experimental and analytical data show that the experimental data has about 75% of the specific impulse that is predicted by the numerical simulations at a given equivalence ratio and that the analytical data predicts an equivalence ratio at about 135% of the experimental equivalence ratio at a given specific impulse. The data presented in Figure 5.18 show that the engine is operating less efficiently than expected, that the thrust measurement is not capturing all of the thrust generated by the engine, or that the local equivalence ratio in the engine is leaner than the global equivalence ratio.

5.4: Specific Thrust

The specific thrust is another important metric for measuring engine performance. The specific thrust is the thrust output by the engine divided by the weight of air being consumed by the engine.

$$ST = \frac{Thrust}{\dot{m}_{Air} g} \tag{5.2}$$

When comparing Equation (5.1) and Equation (5.2), it is evident that the specific thrust is very similar to the specific impulse, with the only difference being the substitution of mass flow of fuel with mass flow of air. Since specific thrust and specific impulse are so similar, it might seem that the specific thrust will also have a strong relationship to the equivalence ratio. However, as Figure 5.19 shows, there is not a strong relationship between specific thrust and equivalence ratio.

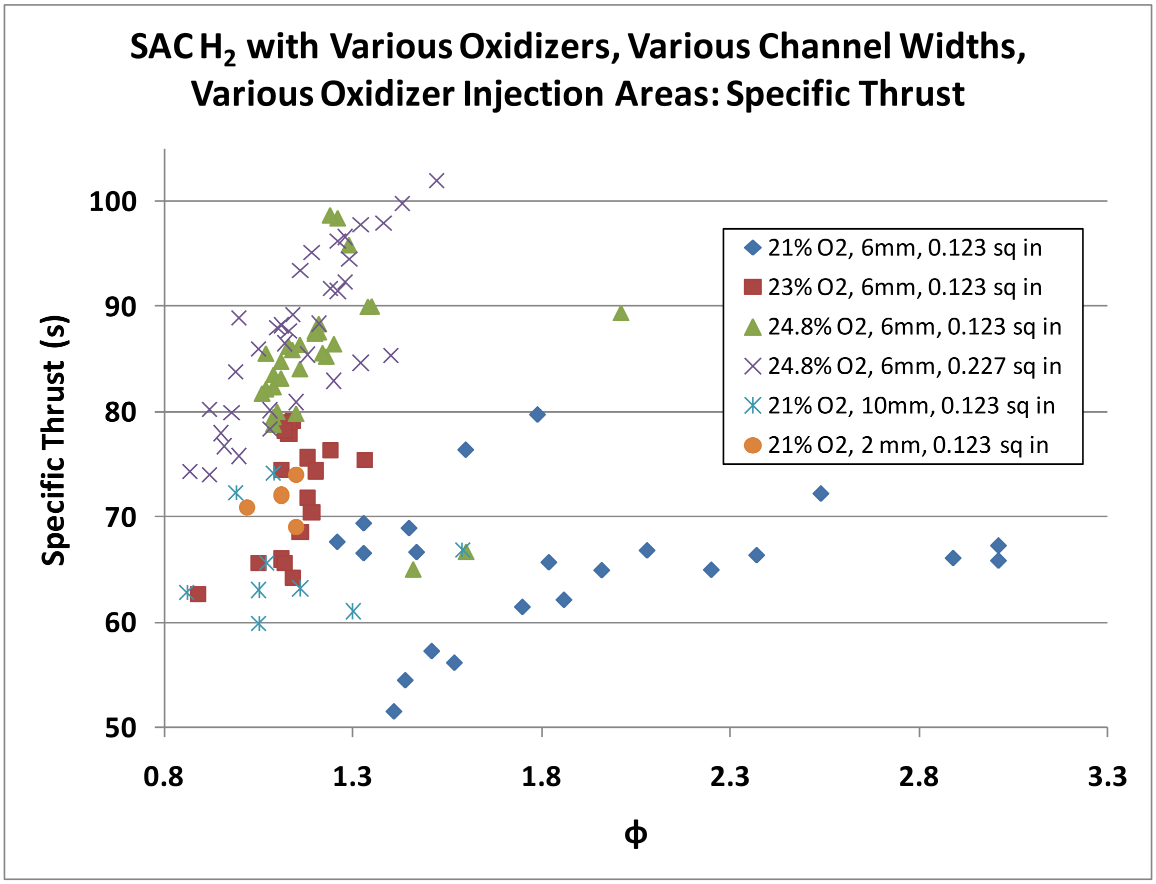

Figure 5.19: Specific thrust as a function of equivalence ratio

Unlike the specific impulse, the terms in the specific thrust equation do not form a ratio of the air mass flow to the fuel mass flow. An increase in the equivalence ratio does appear to cause a modest increase in the thrust output of the engine, but the effect is not large enough to drive the overall trend in Figure 5.19. The next comparison was the specific thrust as a function of the fuel mass flow rate, which is shown in Figure 5.20. This figure shows that an increase in the specific thrust is associated with higher fuel mass flow rates. However, the increase in specific thrust at higher fuel mass flows may be from the greater air mass flows that must be present at higher fuel mass flows in order to obtain air/fuel mixtures that are detonable.

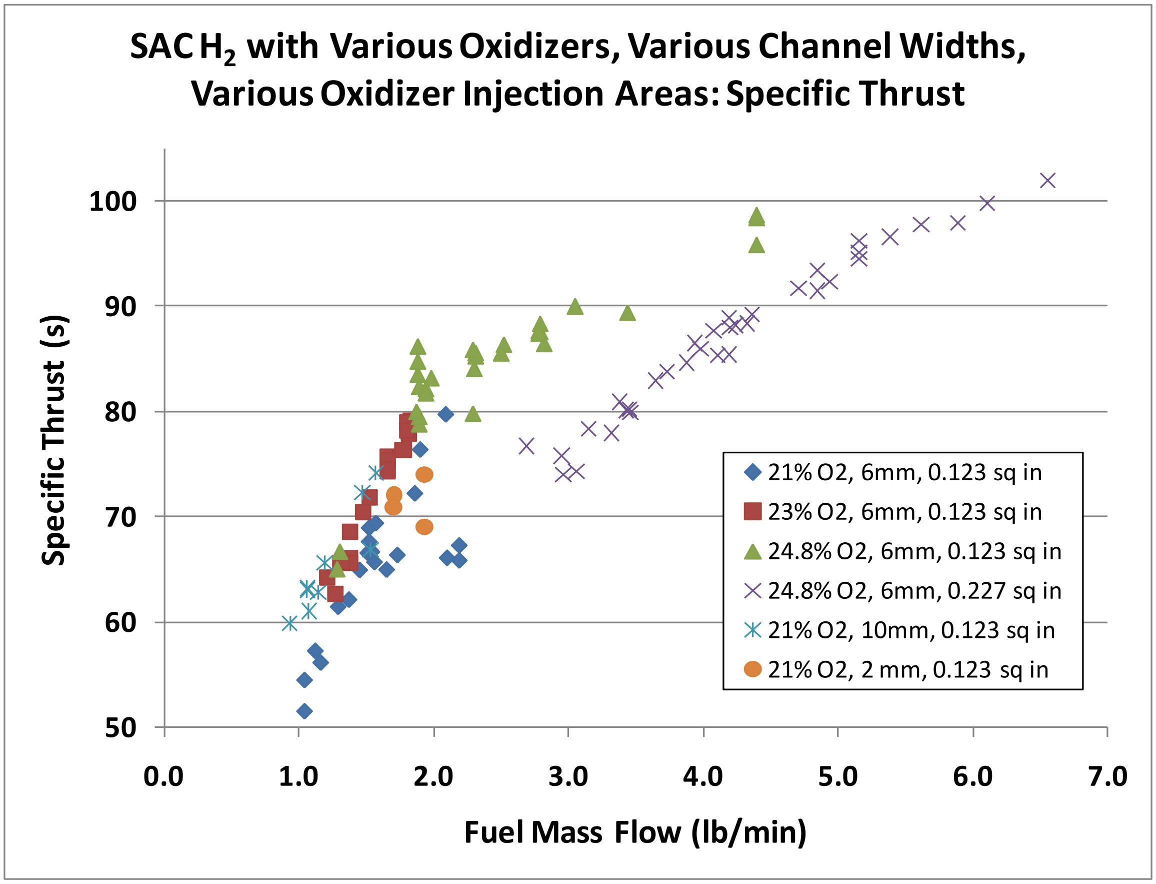

Figure 5.20: Specific thrust as a function of fuel mass flow

Lastly, the specific thrust of the engine was compared to the air mass flow in Figure 5.21. This plot shows if the thrust generated per pound of air flow into the engine varied with different air mass flows. If the engine keeps a constant ratio of thrust to air mass flow over all air mass flow values, then the slope of the points on the graph would be zero. If the engine outputs more thrust per pound of air flow at higher air mass flow values, then the slope of the points on the graph would be positive. Correspondingly, if the engine outputs less thrust per pound of air flow at higher air mass flow values, then the slope of the points on the graph would be negative.

All of the data sets in Figure 5.21 have a positive slope except for the exclusively one wave 0.227 in^2 data. The specific thrust increases linearly with air mass flow through the exclusively one wave 0.123 in^2 data before stagnating at the exclusively one wave 0.227 in^2 data. After the relatively constant specific thrust through the exclusively one wave 0.227 in^2 data, the specific thrust increased linearly with increases in air mass flow through the predominantly one wave 0.227 in^2 data and continued through the predominantly two wave 0.227 in^2 data. In addition, the predominantly one wave 0.123 in^2 data had greater specific thrust values than any of the one wave 0.227 in^2 data. The specific thrust of the two wave 0.123 in^2 data was about 15% greater than the two wave 0.227 in^2 data at similar air mass flows, which is similar to the thrust results of those two data sets that were presented in Figure 5.8. The greater specific thrust of the predominantly one wave 0.123 in^2 data shown in Figure 5.21 is most likely due to the nearly doubled injection pressure of the predominantly one wave 0.123 in^2 when compared to the predominantly one wave 0.227 in^2 data at similar mass flows.

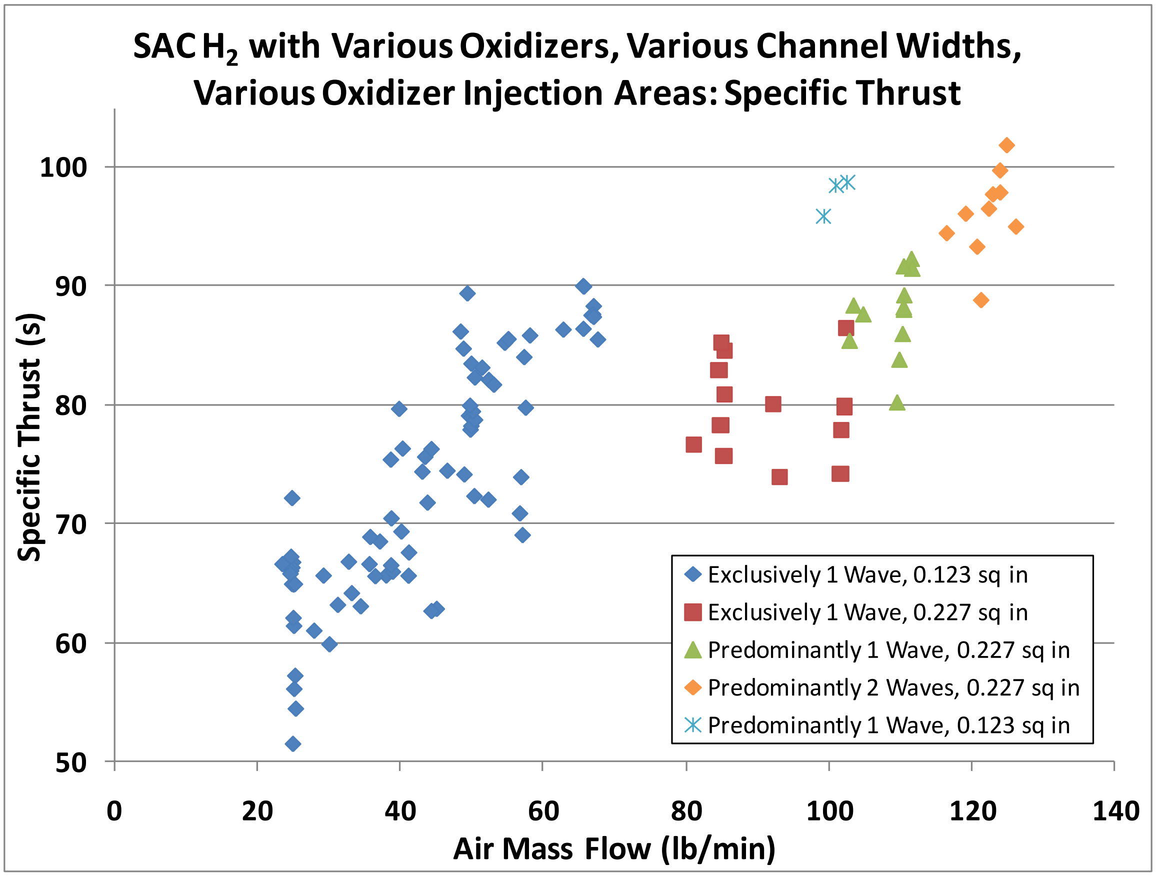

Figure 5.21: Specific thrust as a function of air mass flow

A different method of examining the specific thrust data is shown in Figure 5.22, which plots the specific combustion thrust and the specific gross thrust in seconds on the left y-axis and the percentage of the gross thrust from the combustion thrust on the right y-axis as a function of the air mass flow rate in pounds per minute. The specific combustion thrust is the same trend as the data in Figure 5.21. However, the specific gross thrust decreases as the air mass flow increases until the point where the engine begins two wave activity, where it beings to increase as the air mass flow increases. Due to this decrease in the specific gross thrust, the percentage of the gross thrust from the combustion thrust appears to grow to an asymptotic value until the onset of two wave activity, where it begins to increase again.

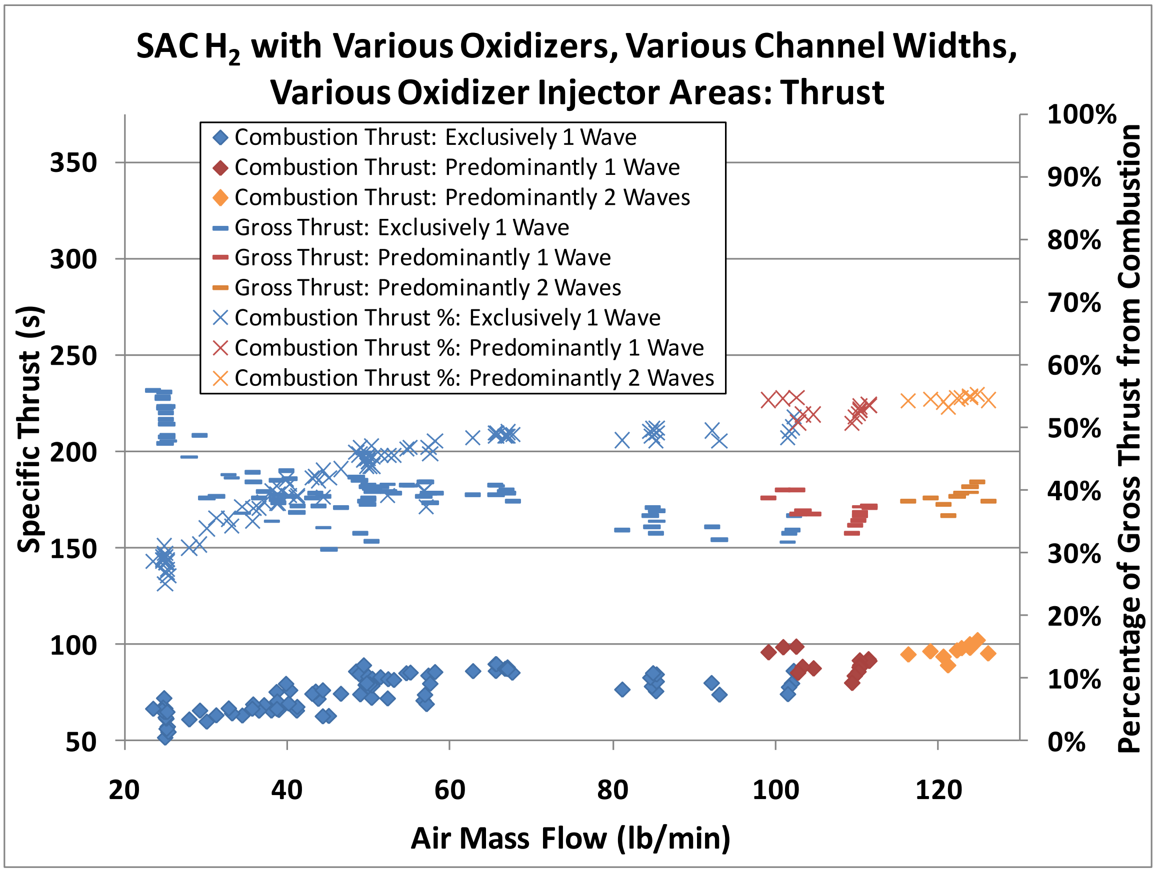

Figure 5.22: Specific detonation and gross thrusts as a function of air mass flow

These specific thrust results are extremely important as they show that the engine has regimes where the thrust output per pound of air input remains constant with increases in air mass flow, and regimes where the thrust output per pound of air input increases with increases in air mass flow. The different characteristics of these regimes have implications on how the engine would operate if it were employed in a practical application.

5.5: Average Combustion Wave Velocity

The velocity of the combustion wave propagating through the detonation channel in the RDE was an important metric for studying the quality of operation. One way the combustion wave velocity was examined was comparing it to the unsteadiness of the combustion wave. The average velocity obtained through a FFT analysis in meters per second is plotted as a function of the unsteadiness of the combustion wave in Figure 5.23. The Chapman-Jouget velocity and the minimum velocity of the detonation are both indicated on the plot.

This plot only contains the runs with air mass flows less than 75 pounds per minute in order to remain outside of one to two wave transition region. Figure 5.23 shows that as the average detonation wave velocity increased, then the unsteadiness of the detonation wave decreased. In addition to the overall relationship between detonation wave speed and unsteadiness of the wave, Figure 5.23 also shows variation among different oxidizers that were used. The runs that used lower percentages of oxygen in the oxidizer had lower velocities for the same value of wave unsteadiness.

The data in Figure 5.23 has an inverse relationship between average detonation wave velocity and unsteadiness of the wave. This is because the velocity of the wave is calculated by dividing the circumference of the detonation channel by the most common change in time between pressure peaks of the run, and the unsteadiness is calculated by taking the standard deviation of all peak to peak times. This analysis, while useful, creates a plot with time in the denominator on the vertical axis and time in the numerator on the horizontal axis.

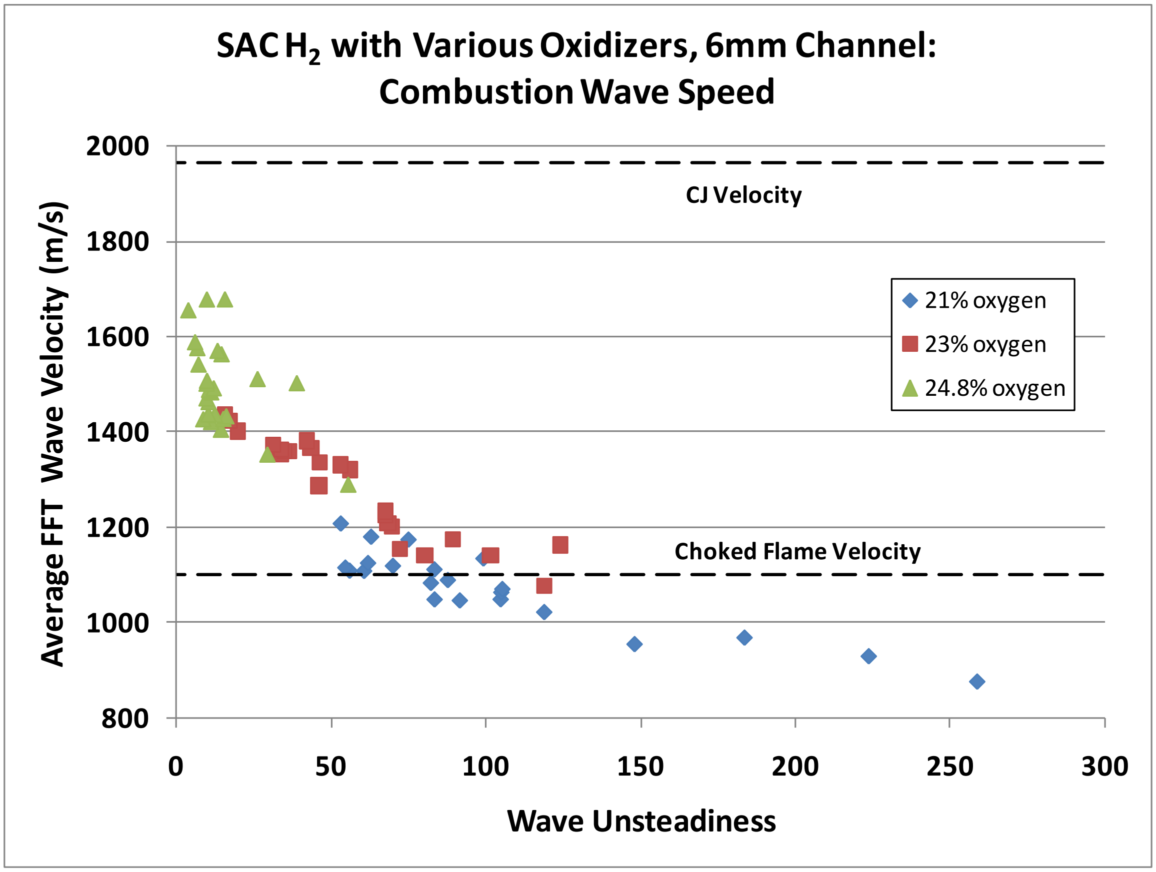

Figure 5.23: Detonation wave velocity for runs with less than 75 lb/min of air flow

Therefore, if the most common detonation lap time is plotted instead of the average detonation wave velocity, a linear trend between average period of the detonation and the unsteadiness of the detonation appears. This method was used to plot the data shown in Figure 5.24, which comprises of the same data used for Figure 5.23. This plot also contains the lap time for a wave travelling at the Chapman-Jouget velocity, as well as a wave travelling at the minimum velocity to be considered a detonation.

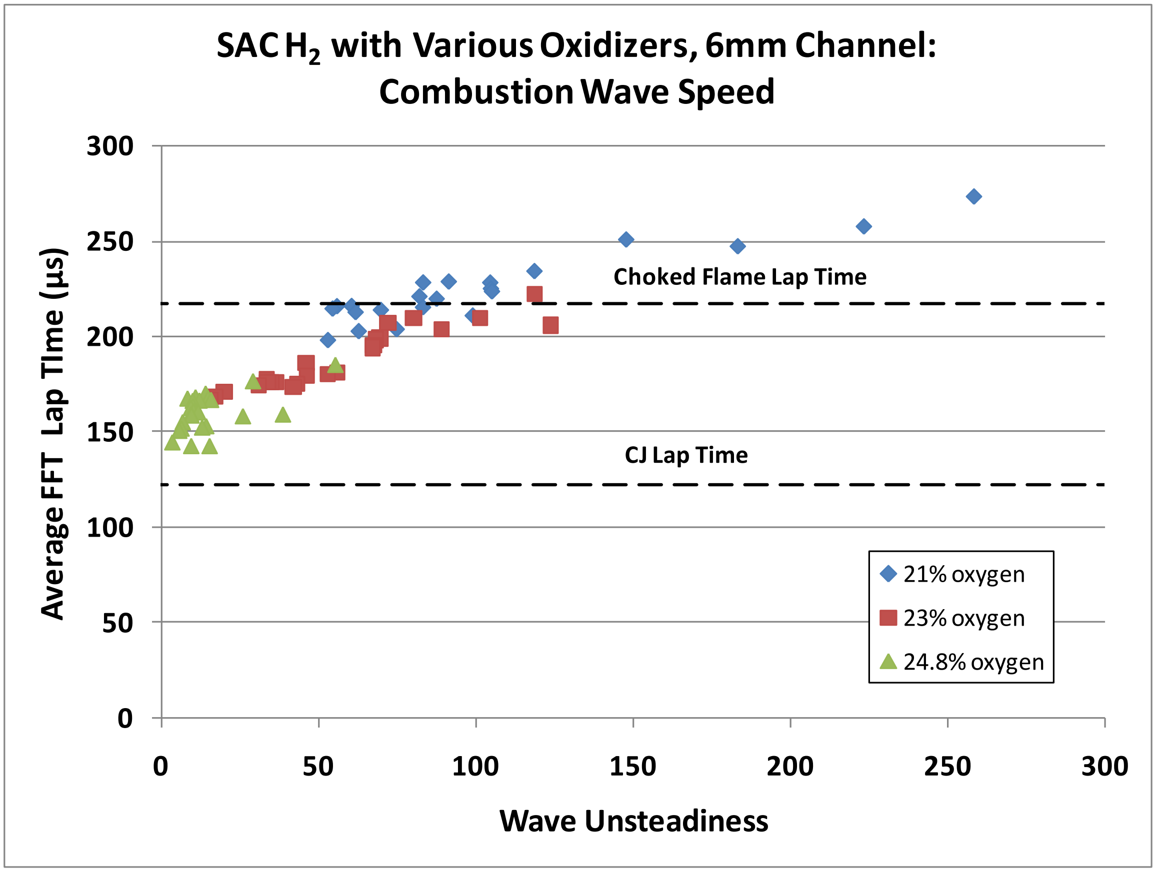

Figure 5.24: Average detonation wave period as a function of wave unsteadiness

Although there were slight differences in the data sets due to oxidizer, the points remained in a relatively uniform linear band. The next plot, Figure 5.25, consolidates all of the exclusively one wave data into a single data set of runs, then adds data points from when the engine operated with two detonation waves. Since none of the runs that had two detonation waves maintained two waves the entire run, the additional data is separated by the predominant wave mode of the run.

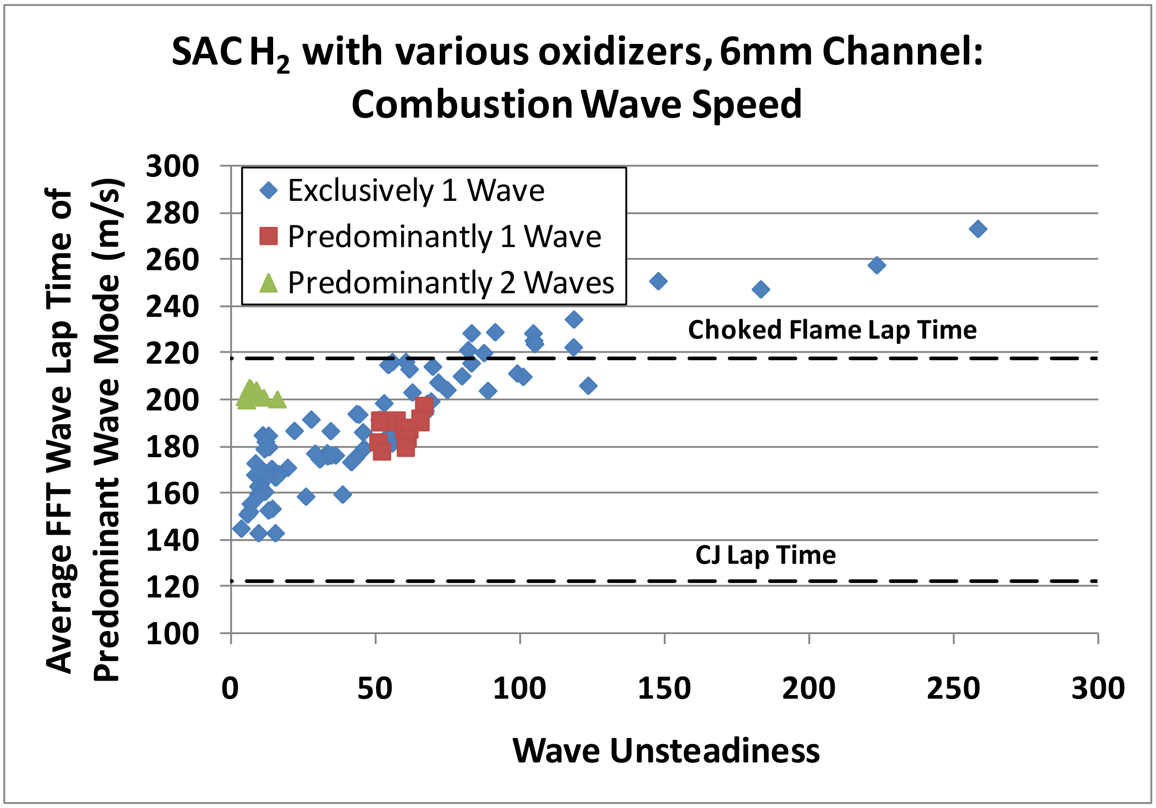

Figure 5.25: Average wave period for 1 and 2 wave modes versus wave unsteadiness

The most important feature of Figure 5.25 is the predominantly two wave runs are much longer lap time (a lower average detonation wave speed) than the exclusively one wave runs at the same wave unsteadiness values, and the predominantly one wave runs are on the shortest lap time section of the exclusively one wave runs at a given wave unsteadiness.

Another way to examine the average FFT wave velocity is to plot it as a function of the air or the air mass flow. The first data set that was examined was the exclusively one wave data with an air mass flow less than 75 pounds per minute. This average detonation wave speed data is plotted as a function of the air mass flow in Figure 5.26.

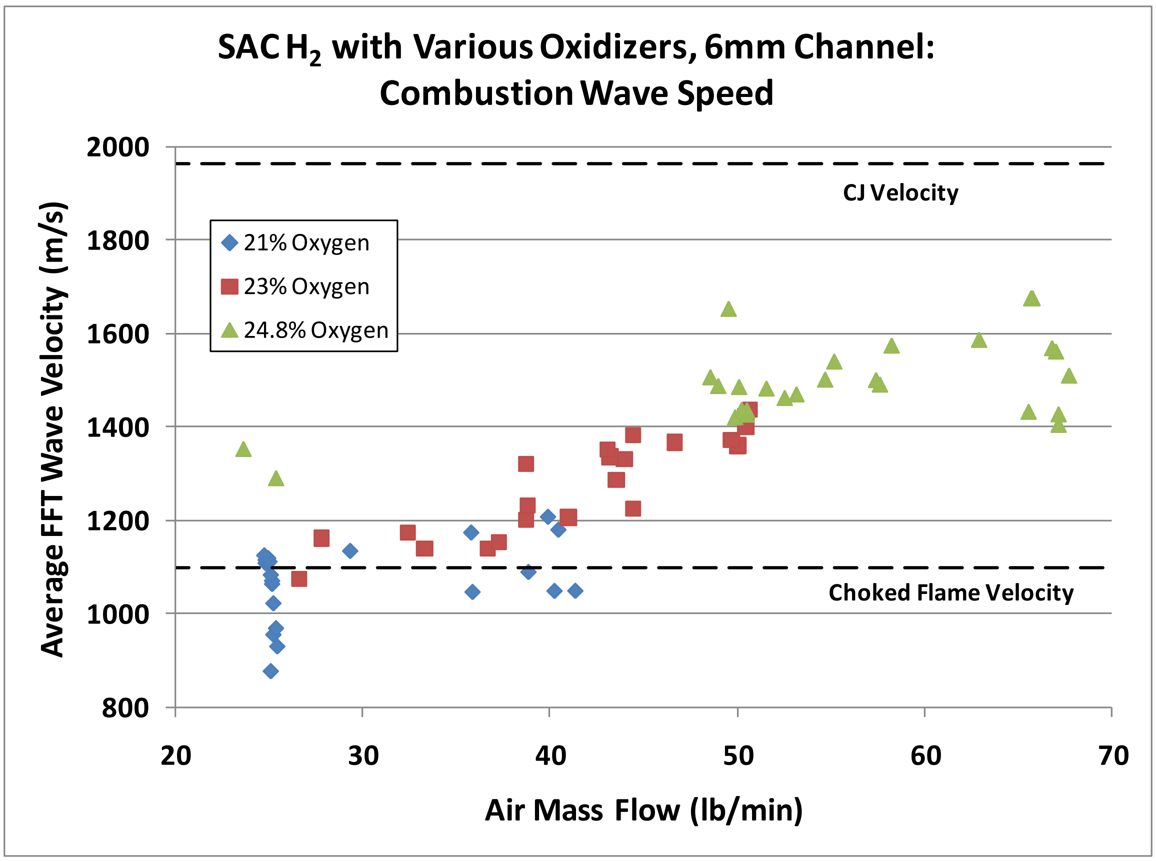

Figure 5.26: Average wave velocity vs air mass flow for exclusively one detonation wave runs with less than 75 pounds per minute of air mass flow

It is shown in Figure 5.26 that the average detonation wave velocity increases with an increase in the air mass flow. However, it appears that the air mass flow does not provide a definitive value for the average detonation wave velocity. This is most evident in the air mass flow range of 24.5 lb/min to 25.5 lb/min, where the detonation velocity varied from 875 m/s to 1124 m/s. This data region amounts to a 28% increase in detonation velocity over just a 4% change in mass flow. However, the fuel mass flow increased by 110% from 1.04 lb/min to 2.19 lb/min over this data region.

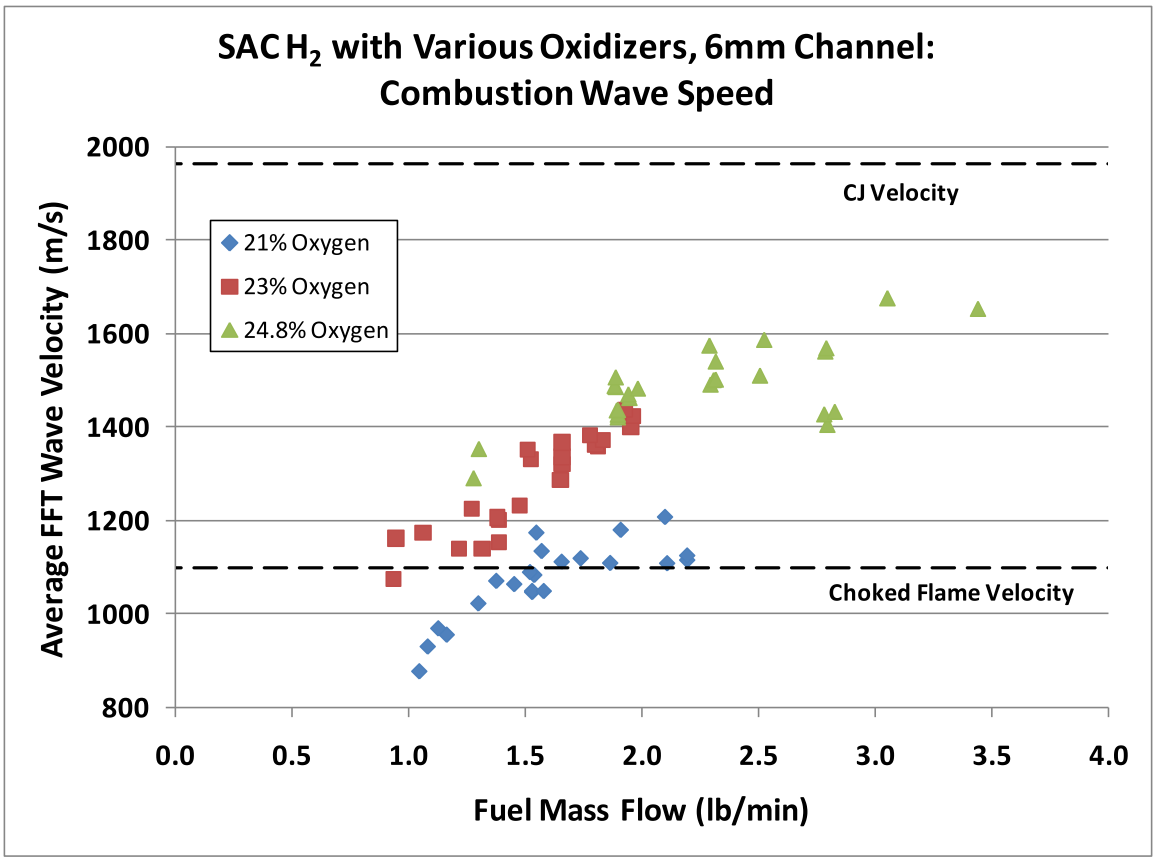

Figure 5.27: Average wave velocity vs fuel mass flow for exclusively one detonation wave runs with less than 75 pounds per minute of air flow

Due to the large increase in the average combustion wave velocity with an increase in fuel mass flow seen in Figure 5.26, the combustion wave velocity for exclusively one wave detonations with air mass flows less than 75 pounds per minute were plotted as a function of fuel mass flow for a constant channel width of 6mm in Figure 5.27. The average detonation wave velocities in Figure 5.27 are much more dependent on the fuel mass flow than the average detonation wave velocities are on the air mass flow in Figure 5.26. In addition, Figure 5.27 shows that the oxidizers with higher percentages of oxygen achieved greater average detonation wave velocities at the same fuel mass flow value.

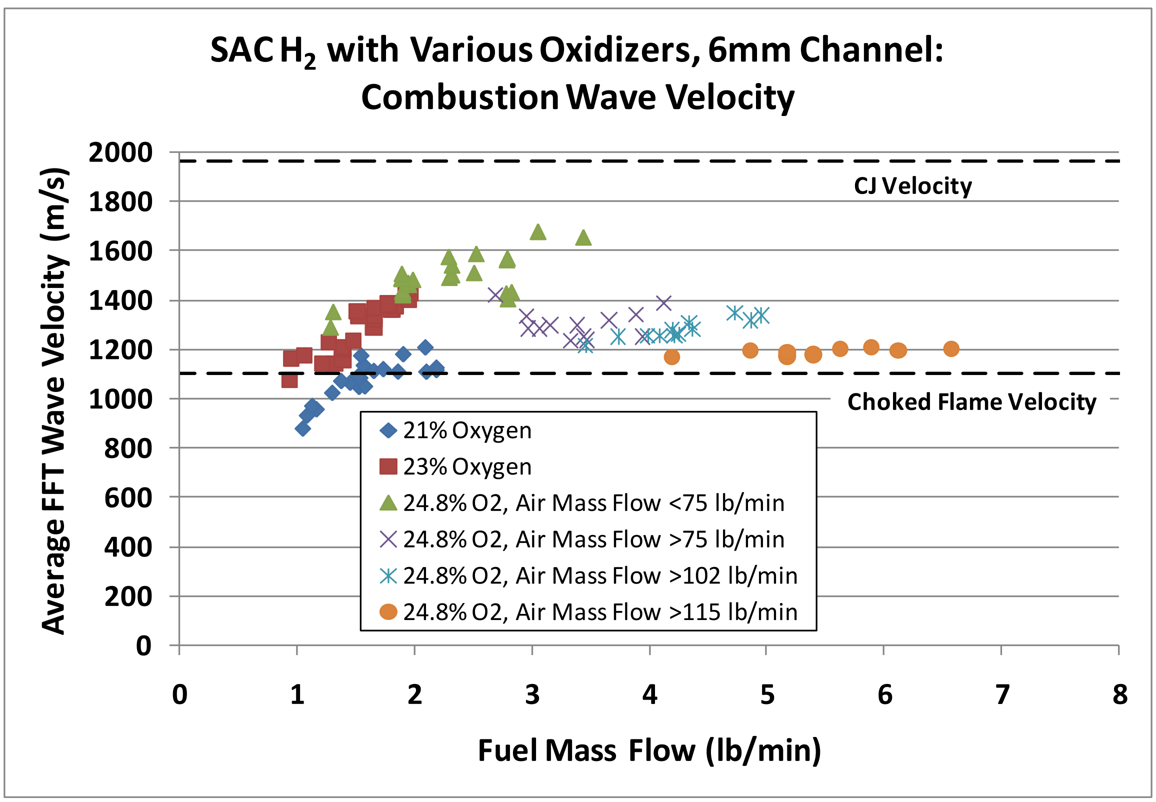

Figure 5.28: Average wave velocity vs fuel mass flow for one and two wave tests

Now that the relationship between average detonation wave velocity and fuel mass flow has been established for one wave operation, the next step is to investigate the relationship between average detonation wave velocity and fuel mass flow in the transition region from one to two detonation waves. All of the data presented in Figure 5.27 is also present in Figure 5.28, with the addition of the data in the one to two wave transition region.

The data in the one to two wave transition region did not experience as rapid an increase in the average detonation wave velocity as the exclusively one wave data when the fuel flow was increased. In addition, the average wave velocity of the predominant wave modes decreased with increases in air mass flow in the transition region. When the increases in the air mass flow progressed the operational mode from the unsteady exclusively one wave runs just prior to two wave activity (purple X's) to primarily one wave runs with some two wave activity (blue X's) to primarily two wave runs (orange circles), the average wave velocity of the predominant wave mode decreased.

5.6: Two Detonation Wave Transition

Both the onset of two wave activity and the transition from predominantly one wave to predominantly two wave activity occurred over small regions of air mass flow. Both transition phenomena are shown in Figure 5.29.

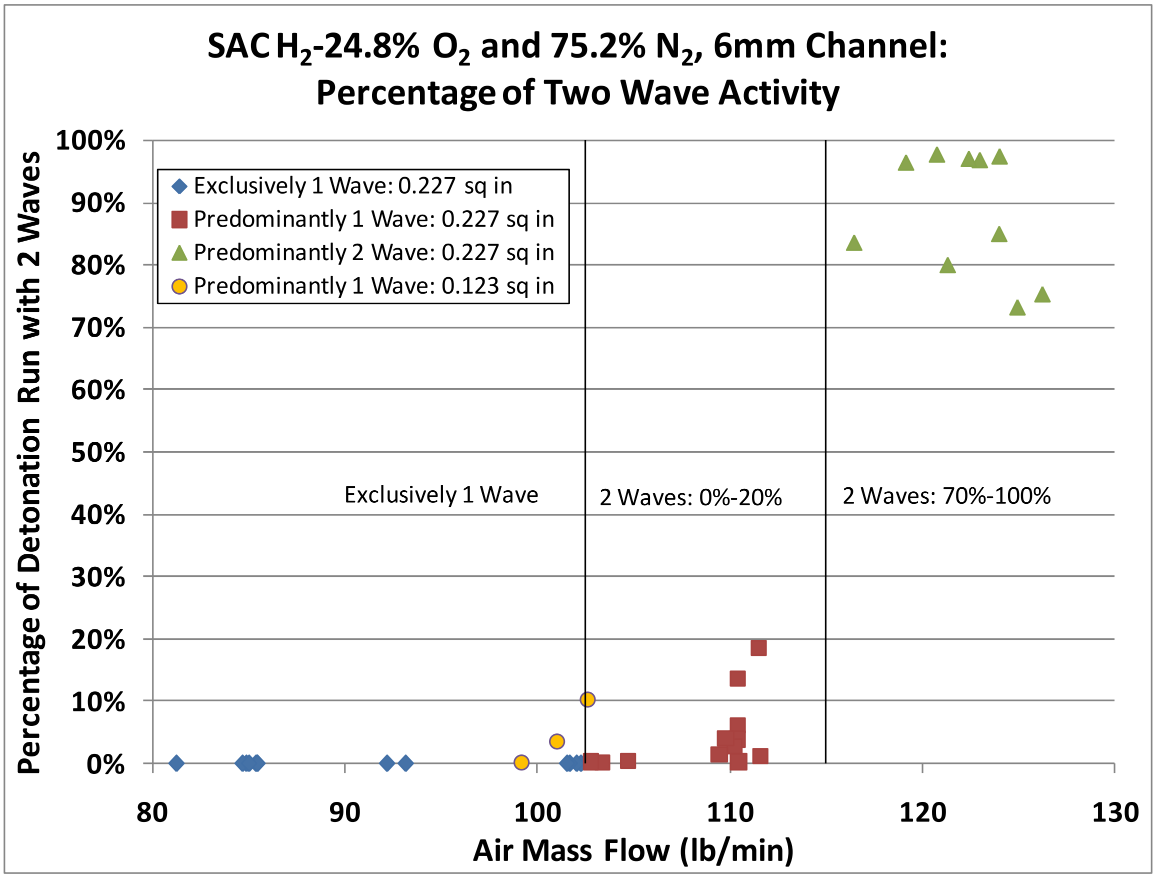

Figure 5.29: Transition to two wave and predominantly two wave activity

As is seen in Figure 5.29, the transition from exclusively one wave activity to quasi-two wave activity for the gross oxidizer injector area of 0.227 in^2 occurs over the very narrow air mass flow region of 102.3 and 102.8 lb/min. However, the transition occurs at a lower air flow rate for the smaller gross oxidizer injector area of 0.123 in^2. The transition from the predominantly one wave region to the predominantly two wave region is not over as small of an air mass flow range as the transition from exclusively one was to quasi-two wave activity, but it is still a sudden change in engine operation as it occurs over only 5 lb/min of air flow from 111.5 to 116.5 lb/min. It is possible that some property of the engine makes it averse to sustaining two wave activity around 50% of the run time, or that the increase in two wave activity as a percentage of the run is much more rapid between 111.5 to 116.5 lb/min of air flow than in the predominantly one wave and predominantly two wave sections of Figure 5.29. If the more rapid transition were the case and the percentage of two wave behavior formed an S-curve through the 111.5-116.5 lb/min of air flow region, then the average rate of increased two wave activity would have to increase from a 2% increase per pound of air added in the predominantly one wave region to an 11% increase per pound of air added in the transition region between 111.5-116.5 lb/min.

Another interesting phenomenon is the way the unsteadiness of the wave changed as the air mass flow into the engine was increased. Figure 5.30 contains a plot of the wave unsteadiness as a function of the air mass flow in pounds per minute. The figure shows tests that were exclusively one detonation wave runs with air mass flows less than 75 pounds per minute in order to remain out of the one to two wave transition region. Each series of data, although different in their specific values, had steadier waves as the mass flow increased from the minimum air mass flow that produced a detonation to around 60 lb/min. The exception to this trend is the lowest air mass flow runs, which were run at a great variety of equivalence ratios. When the amount of fuel flow for these runs on the edge of operation was increased, the unsteadiness of the wave dropped more precipitously than what was seen for the runs with higher air mass flows.

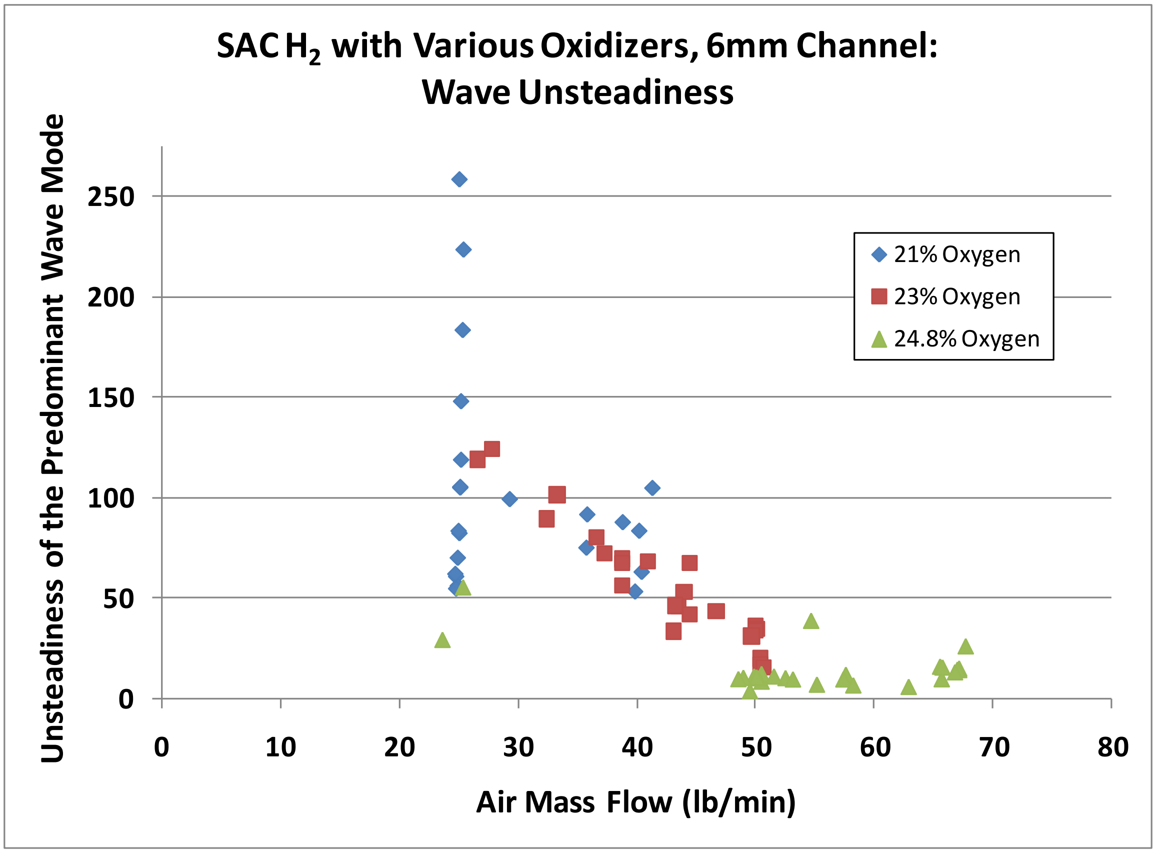

Figure 5.30: Wave unsteadiness vs air mass flow for one detonation wave

The next step is to examine the wave unsteadiness as a function of air mass flow in the one to two wave transition region. In order to understand the wave unsteadiness at a more basic level, Figure 5.31 shows four plots of the time between each pair of pressure peaks on a logarithmic scale as a function of the average of the times when each pressure peak occurred. The first plot (A) at 85.0 lb/min of air flow depicts a very steady single detonation wave since the lap time for the detonation wave varied very slightly from lap to lap.

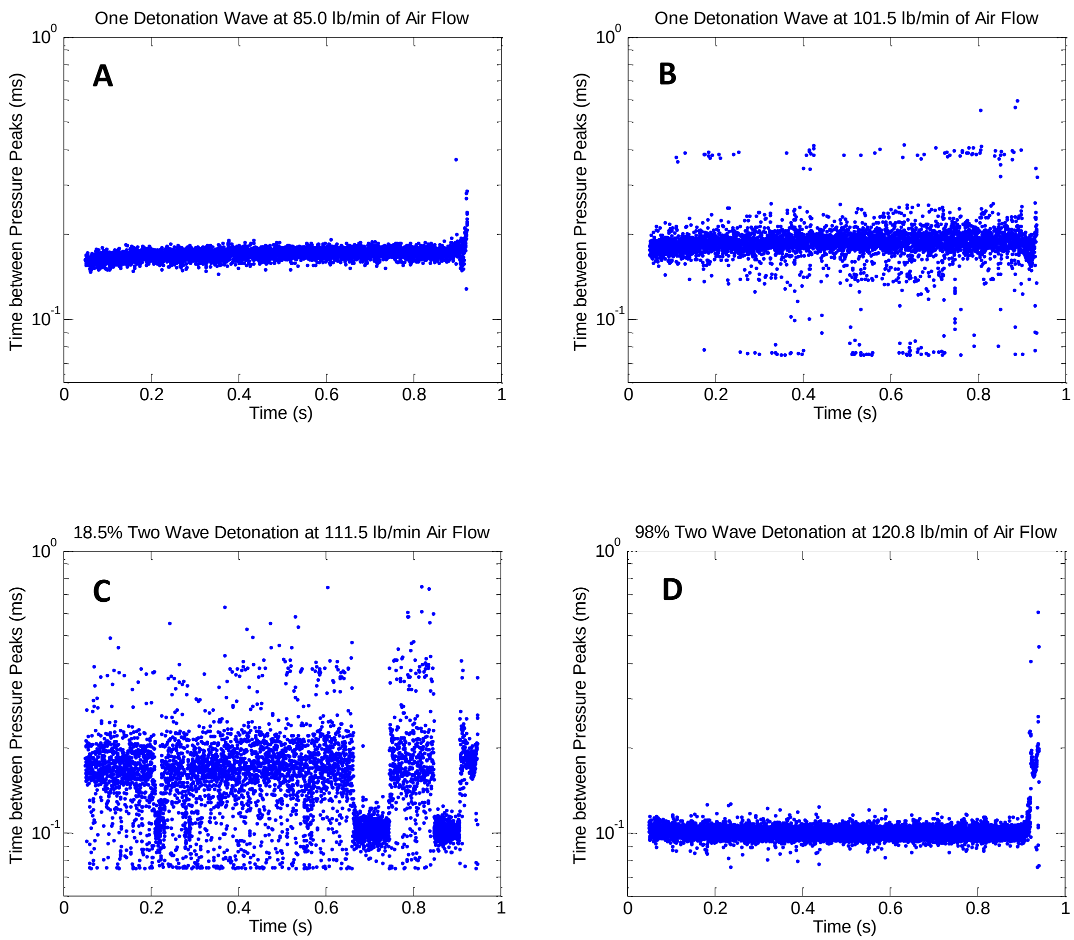

Figure 5.31: Lap times during the one to two wave transition

The second plot (B) at 101.5 lb/min of air flow shows a single detonation wave at an average lap time (and therefore wave speed) very near to the 85.0 lb/min run, but with much greater variation in the lap times. The third plot (C) at 111.5 lb/min of air flow shows one wave operation near the same average velocity as plots A and B for 81.5% of the run, but with even greater variation in the lap times. The other 18.5% of the run in the plot C contains two detonation waves, which were present during the time periods where the average time between the pressure peaks was nearly cut in half. The fourth plot (D) at 120.8 lb/min of air flow shows very steady two wave detonation with an average lap time very similar to the portion of the plot C containing two detonation waves.

An interesting result of this testing was the fact that none of the test runs sustained two detonation waves for the entire run. This result was due to the fact that every run, even the runs that predominantly contained two steady detonation waves, concluded with a period of one wave operation. The ending of the run always contained one wave because the flow of fuel and air into the engine was not stopped instantaneously, creating a period of time where the mass flow into the engine was decreased but had not completely shutoff. This lower mass flow caused the combustion reaction to degrade from two detonation waves to one detonation wave. For runs that were predominantly two wave operation before the shutdown sequence, the one wave activity was relatively brief as it only occurred during the last 10 to 30 ms of the run. The one wave activity during the shutdown of a predominantly two wave run can be easily seen in plot D of Figure 5.31.

The plots in Figure 5.31 are individual snapshots of the transition process from one to two detonation wave operation in the RDE with an increase in air mass flow. Although these plots provide an effective visual description of the wave transition region, the transition is more rigorously described by quantifying the wave unsteadiness of the plots in Figure 5.31 and other test runs in the transition region by computing the standard deviation of the lap times. The unsteadiness of the predominant wave form in the run in microseconds was plotted as a function of the air mass flow in pounds per minute in Figure 5.32. The data in this figure is separated into three groups based on the wave activity that occurred during the test. The blue diamonds are the runs that contained only one detonation wave. The red squares are the runs that contained both one and two detonation waves, but predominantly contained one detonation wave. The green triangles are the runs that contained both one and two detonation waves, but predominantly contained two detonation waves. The points in Figure 5.32 that were shown in greater detail in Figure 5.31 are labeled accordingly.

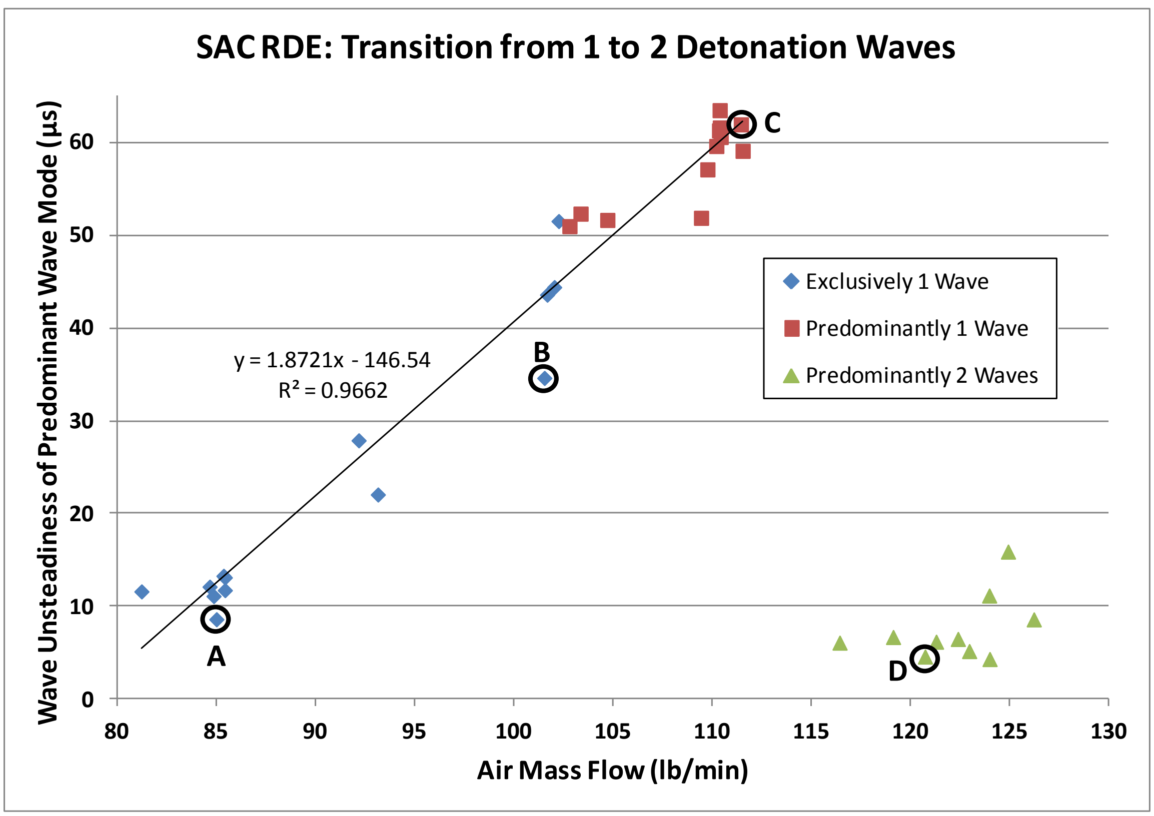

Figure 5.32: Wave unsteadiness versus air flow for two detonation waves

The tests in Figure 5.32 show that the increasing unsteadiness of the single detonation wave with increases in air mass flow shown in plots A, B, and C of Figure 5.31 have a linear relationship. Although some variation occurred in this linear trend, the high R^2 value indicates that the fit is quite accurate. The transition region from one to two detonation waves is comprised of all the tests that fell into this linear trend between the unsteadiness of the predominant detonation wave form and the air mass flow into the engine. After the engine transitions to predominantly two detonation wave operation above 115 lb/min of air flow, the unsteadiness of the two wave detonation is very similar to the unsteadiness of the most steady single detonation wave runs. This sharp drop in the unsteadiness of the predominant wave form in the engine at air mass flows above 115 lb/min shows that the engine is capable of steady operation at higher air mass flows by establishing additional detonation

The data in Figure 5.30 was combined with the data in Figure 5.32 in order to show the unsteadiness of the primary detonation wave mode for the entire air mass flow test range in Figure 5.33. The data in Figure 5.33 clearly shows the trend of the unsteadiness of the wave as the air mass flow increased. The unsteadiness of the detonation wave was the greatest at the lowest air mass flows that the engine could maintain a combustion wave inside of the detonation channel. As the air mass flow increased, the unsteadiness of the detonation decreased until about 60 lb/min. The runs performed with about 60 lb/min of air had the highest average detonation wave velocities and were the most steady of the one wave runs. As the air flow increased past 60 lb/min, the detonation wave became progressively less steady until an air mass flow rate of 115 lb/min was reached, where the engine established two detonation waves as the predominant operating mode. The steadiness of the two wave mode of the predominantly two detonation wave runs was very high, with some runs as steady as the most steady exclusively one detonation wave runs.

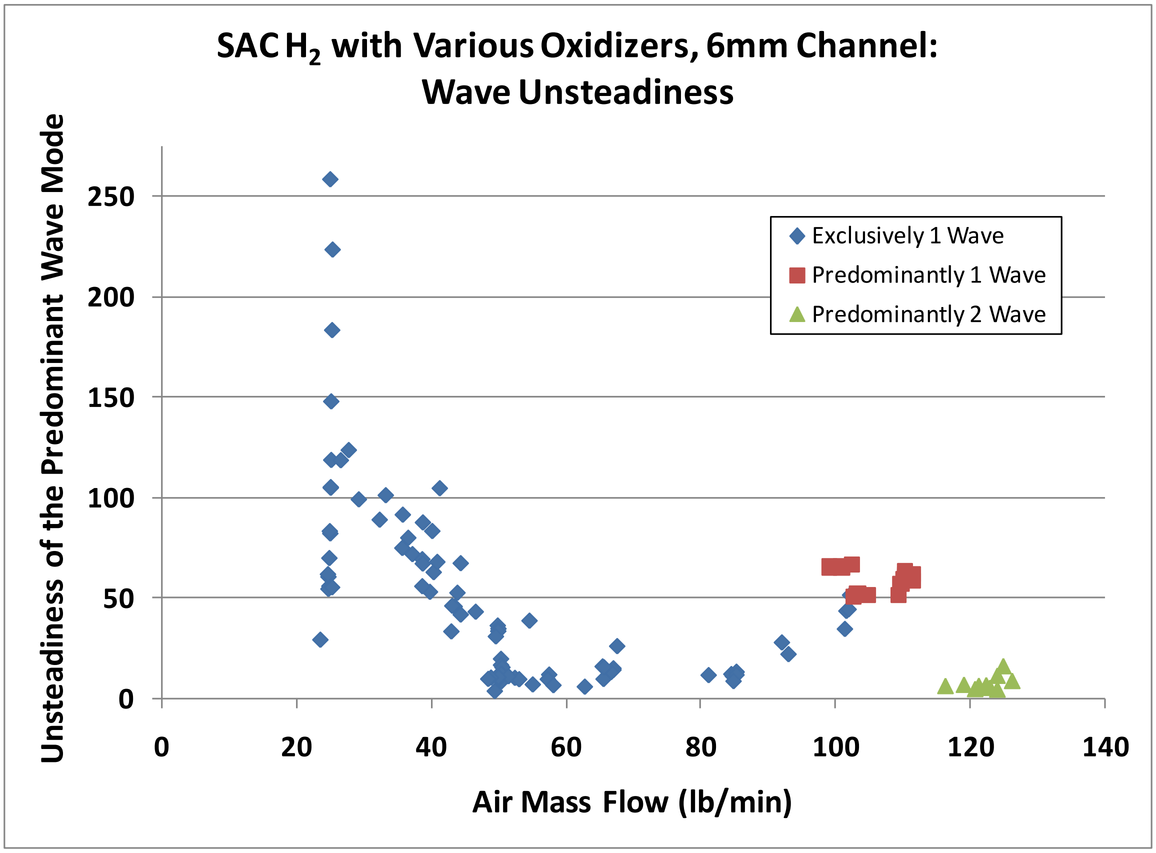

Figure 5.33: Wave unsteadiness of the predominant wave mode as a function of air mass flow for the entire air mass flow test range

It was established in Figure 5.23 that there was an inverse relationship between the average detonation wave speed and the steadiness of the detonation wave. This relationship is presented through an alternative method in Figure 5.34. This figure shows all the unsteadiness points with diamonds and all the velocity points with X's. The exclusively one wave points are blue, the predominantly one wave runs are red, and the predominantly two wave runs are green. The unsteadiness points are plotted with the vertical scale on the left and the velocity points are plotted with the vertical scale on the right.

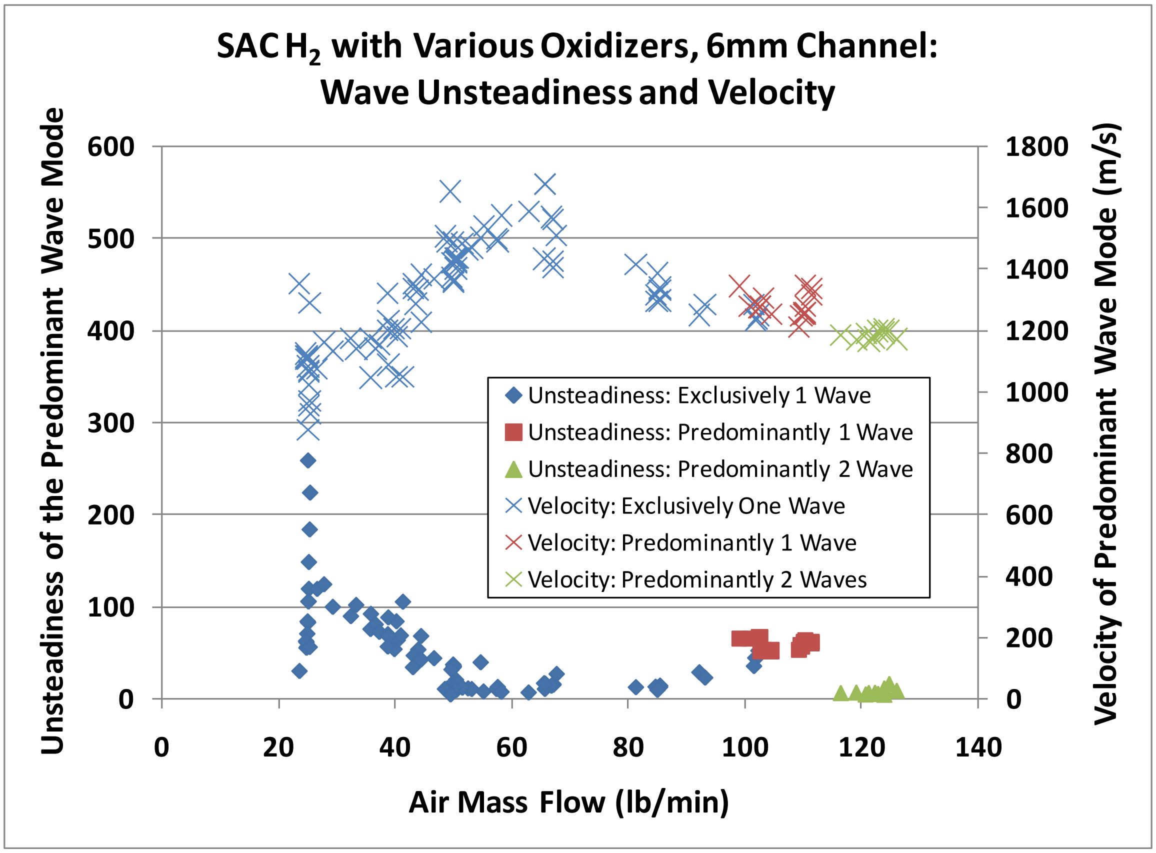

Figure 5.34: Wave unsteadiness and average wave velocity as a function of air flow

Figure 5.34 shows that as the unsteadiness of the detonation wave decreases, the velocity of the detonation wave increases for all of the exclusively one wave data. However, there are not enough data points for the multimodal runs to determine if they also adhere to the same relationship between wave unsteadiness and wave velocity. Once again, it is very evident in this plot that the predominantly one wave runs have greater unsteadiness than exclusively one wave runs at the same velocity, and the predominantly two wave runs is at a lower unsteadiness than exclusively one wave runs at the same velocity. These results are in excellent agreement with the data shown in Figure 5.25.

5.7: Channel Pressure at Ignition

In order to determine the pressure inside the channel during testing, a static pressure transducer was attached to a 12” long ¼” diameter piece of tubing and inserted into one of the pressure ports on the outer shell of the engine. The pressure sensor was used to determine the average pressure in the channel when the fuel and air were flowing into the channel before ignition, and when the detonation was propagating in the channel. A plot of the pressure in the channel in absolute pounds per square inch with fuel and air flow is shown as a function of the air flow in pounds per minute in Figure 5.35.

The data in Figure 5.35 shows that the pressure in the channel at the time of ignition fell precipitously as the air mass flow was increased from 43.3 lb/min to 50.5 lb/min after modest increases in pressure as the air mass flow increased from 26.6 lb/min to 43.3 lb/min. The pressure rose just over 1 psi as the air mass flow increased by 16.7 lb/min, before falling over 8 psi after an air mass flow increase of just 7.2 lb/min.

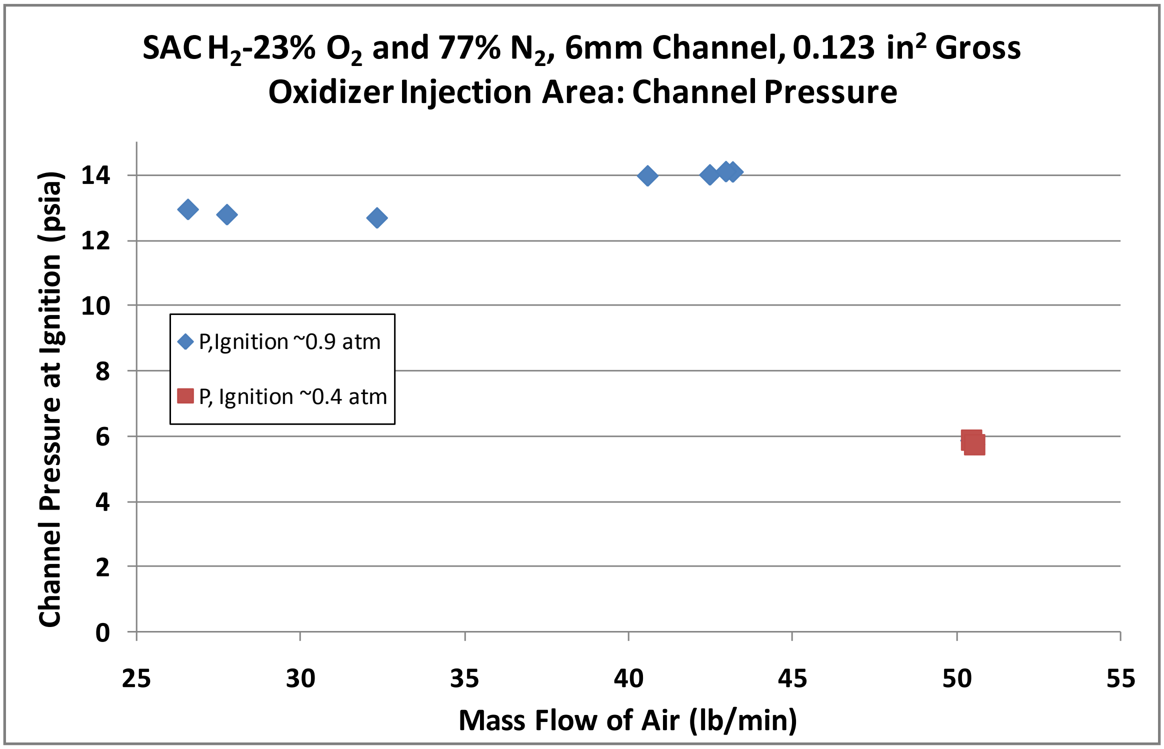

Figure 5.35: Channel pressure at ignition as a function of air mass flow

After this large decrease in pressure in the detonation channel at the time of ignition was discovered, the pressure of the channel while the engine was detonating was investigated for the tests examined in Figure 5.35 to determine how the change in ignition pressure affected the performance of the engine. The first quantity examined was the average pressure in the channel as the detonation was propagating through it. Figure 5.36 shows the average channel pressure with the propagating detonation is absolute pounds per square inch as a function of the mass flow of air in pounds per minute. Also included in the figure is a linear trend line obtained by the series with ignition channel pressures of about 0.9 atm. This trend line provides an estimation of how near the 0.4 atm data was to the trend established by the 0.9 atm data.

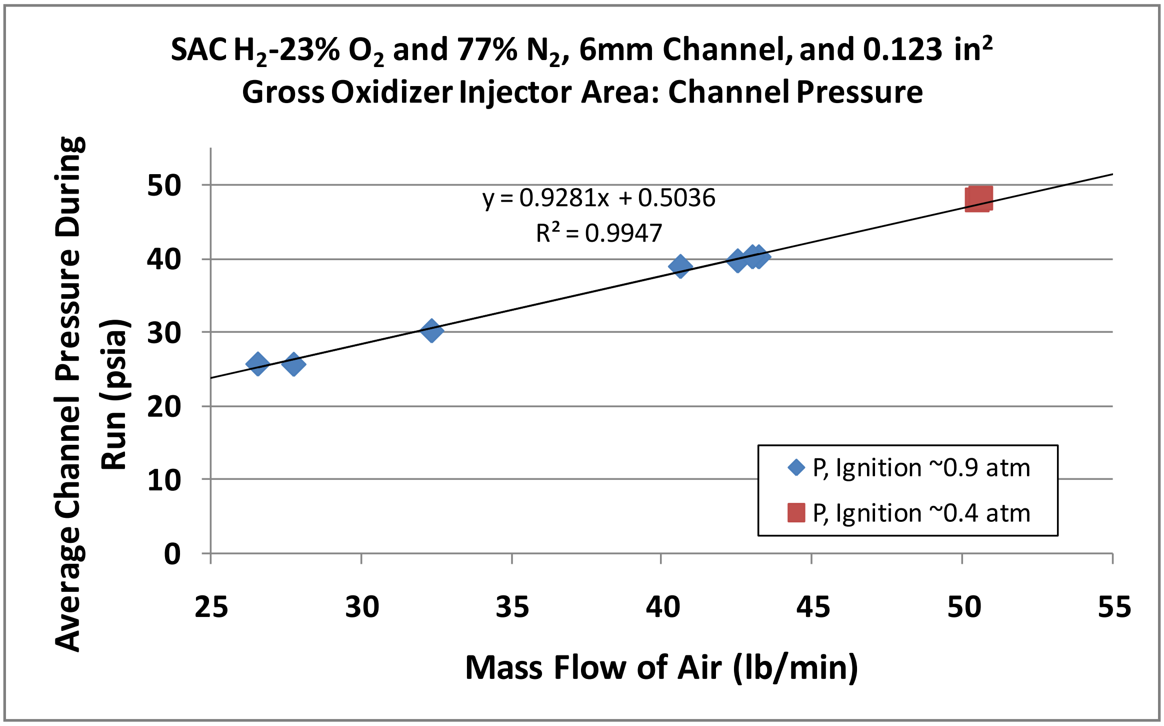

Figure 5.36: Average channel pressure during detonation as a function of air mass flow

This data in Figure 5.36 show that although the pressure at ignition varied greatly from the two series of data, all of the points strictly followed a direct linear relationship for the average channel pressure during detonation and the air mass flow. The average channel pressure during detonation of the 0.4 psia points were within 2% of the pressure expected by the trend line at each air flow rate. This accordance with the higher ignition pressure data suggests that the channel pressure just prior to ignition does not have an effect on the pressure caused by the detonation. If the ignition pressure does not affect the pressure of the detonation, then the ignition pressure most likely does not affect the thrust output of the engine either since the average pressure in the channel drives the amount of thrust generated by the engine.

Since the relationship between average channel pressure during detonation and air mass flow did not change when the ignition pressure fell considerably for the highest air mass flow runs, the amount of pressure increase from the detonation would not follow a direct linear trend similar to the average channel pressure during detonation and air mass flow. This is because the channel pressure at ignition and the increase in channel pressure from ignition must add up to the average channel pressure during detonation.

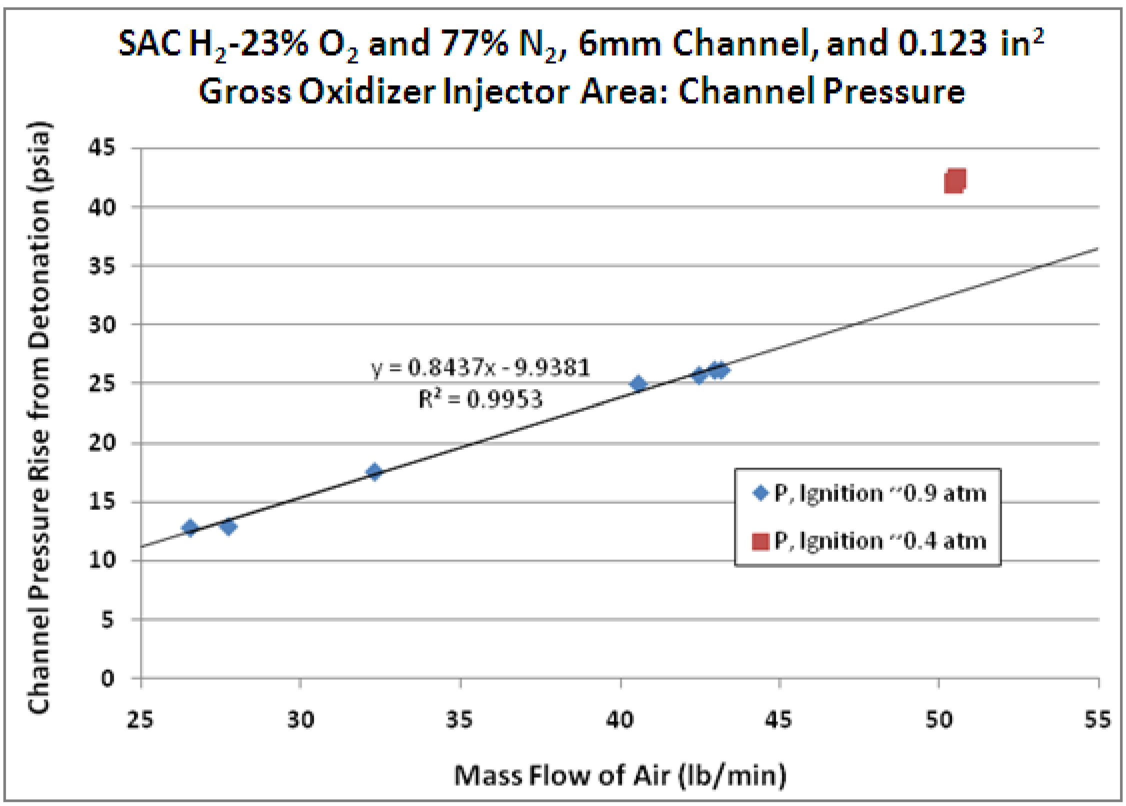

Figure 5.37: Channel pressure rise from the detonation as a function of air mass flow

This relationship is shown in Figure 5.37, where the channel pressure increase from the detonation in absolute pounds per square inch is plotted as a function of air mass flow in pounds per minute. Unlike Figure 5.36, the linear trend line from the 0.9 atm data does not accurately predict the value of the 0.4 atm data. In fact, the estimated channel pressure from the trend line of the 0.9 atm data is more than 30% lower than the channel pressure rise of the experimental data.

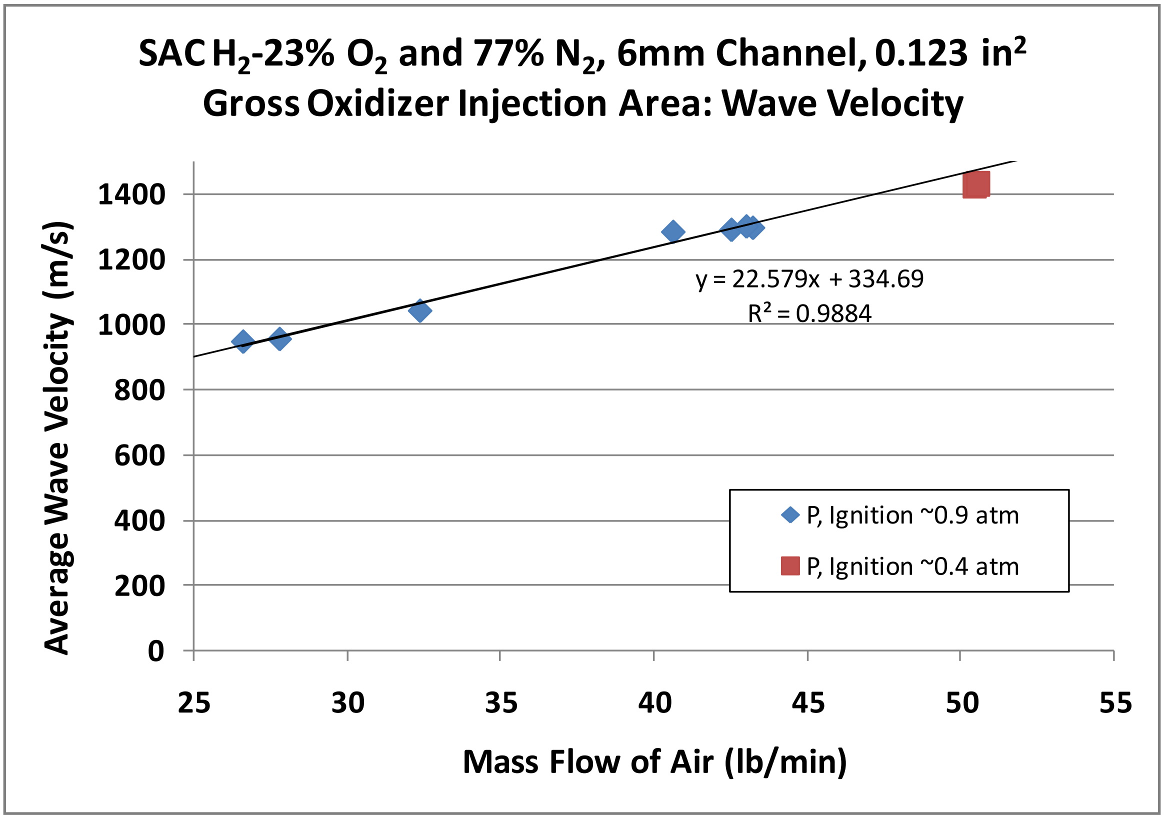

Figure 5.38: Average detonation wave velocity as a function of air mass flow

The last measurement of the engine that was analyzed is the average detonation wave speed. This average detonation wave speed in m/s was plotted as a function of the mass air flow in lb/min in Figure 5.38. This figure shows that the average detonation velocity also appears to be independent of the ignition pressure since the runs that had an ignition pressure around 0.9 atm and the points that had ignition pressures around 0.4 atm followed the same direct linear trend for average detonation wave velocity versus air mass flow. The linear trend line obtained from the points with ignition pressures near 0.9 atm overestimated the average detonation wave velocity of the 0.4 atm points by less than 4%.

5.8: Channel Pressure during Detonation

Although the PCB pressure sensors were proficient at determining when the detonation wave passed the sensor, the actual pressure readings recorded by the PCBs were inaccurate. In order to obtain the pressure of the detonation wave and the pressure of the detonation channel, a Kulite pressure sensor was placed in one of the pressure ports previously occupied by a PCB. The resulting pressure trace shown in Figure 5.39 is very similar in appearance to the PCB pressure trace shown in Figure 4.3.

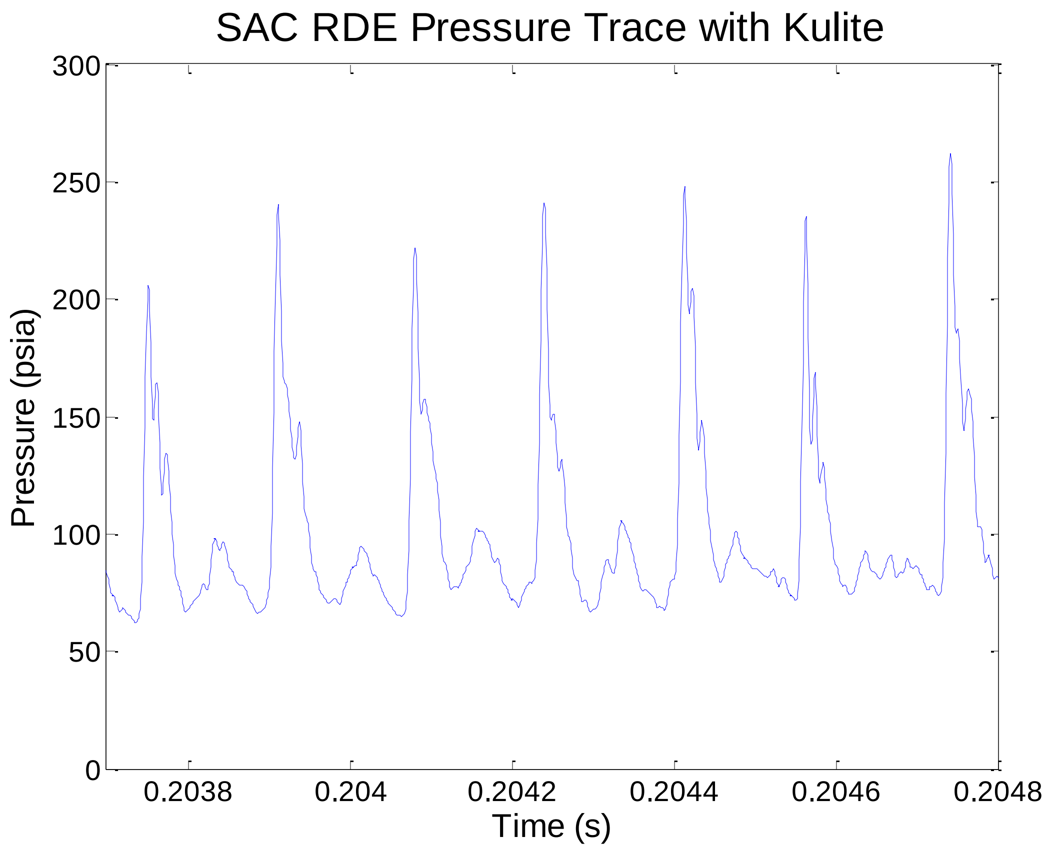

Figure 5.39: Pressure trace of a rotating detonation wave with a kulite pressure sensor

The Kulite pressure trace provides the magnitude of the pressure increase from the detonation wave, as well as the baseline pressure in the detonation channel. The baseline pressure in the detonation channel was determined by finding the mode of the pressure data in 0.01second intervals, then averaging the values of each mode point. In order to avoid any of the transient effects of ignition and shutdown, the mode analysis began 0.05 seconds after ignition and ended 0.05 seconds before shutdown. Figure 5.40 shows a short window of the Kulite pressure data from a detonating run along with the value of the mode of three adjacent 0.01 second intervals.

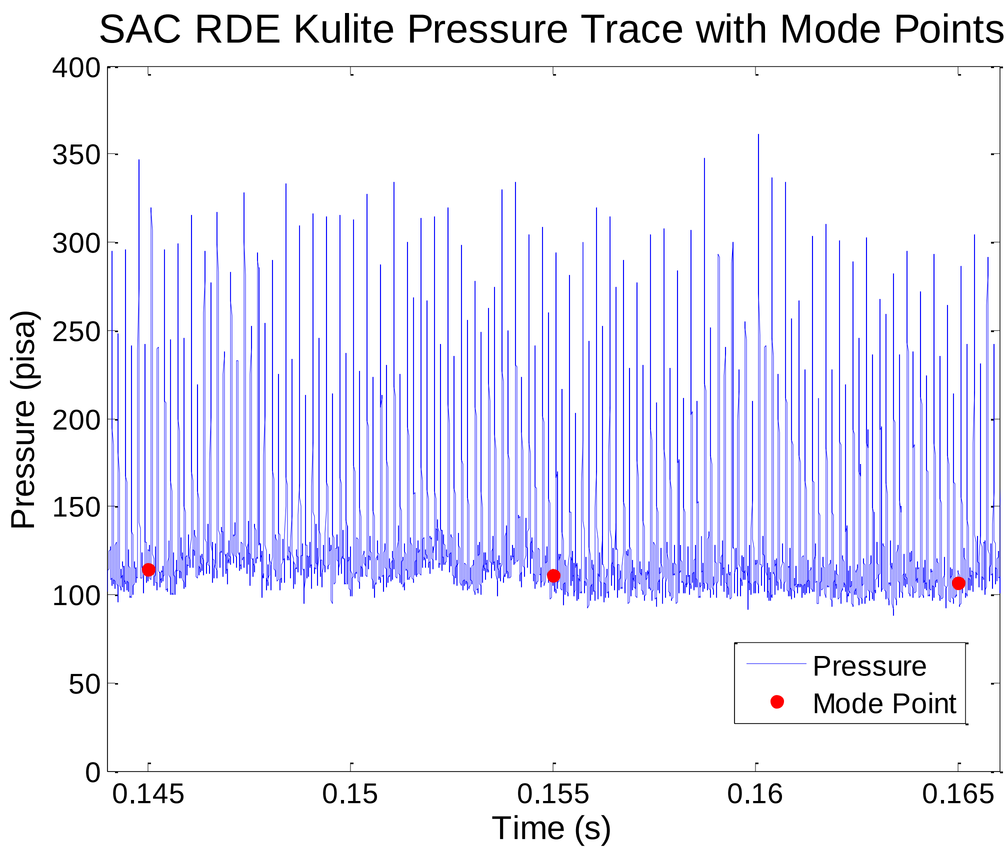

Figure 5.40: Kulite pressure trace with calculated mode points

The average of the modes of every 0.01 second interval provided the average pressure of the detonation channel during operation when the detonation wave was not near the pressure transducer. This channel pressure had a linear relationship to the air mass flow into the engine, as shown in Figure 5.41. This plot indicates that as the air mass flow into the engine increased, the channel pressure during the detonation combustion process increased as well.

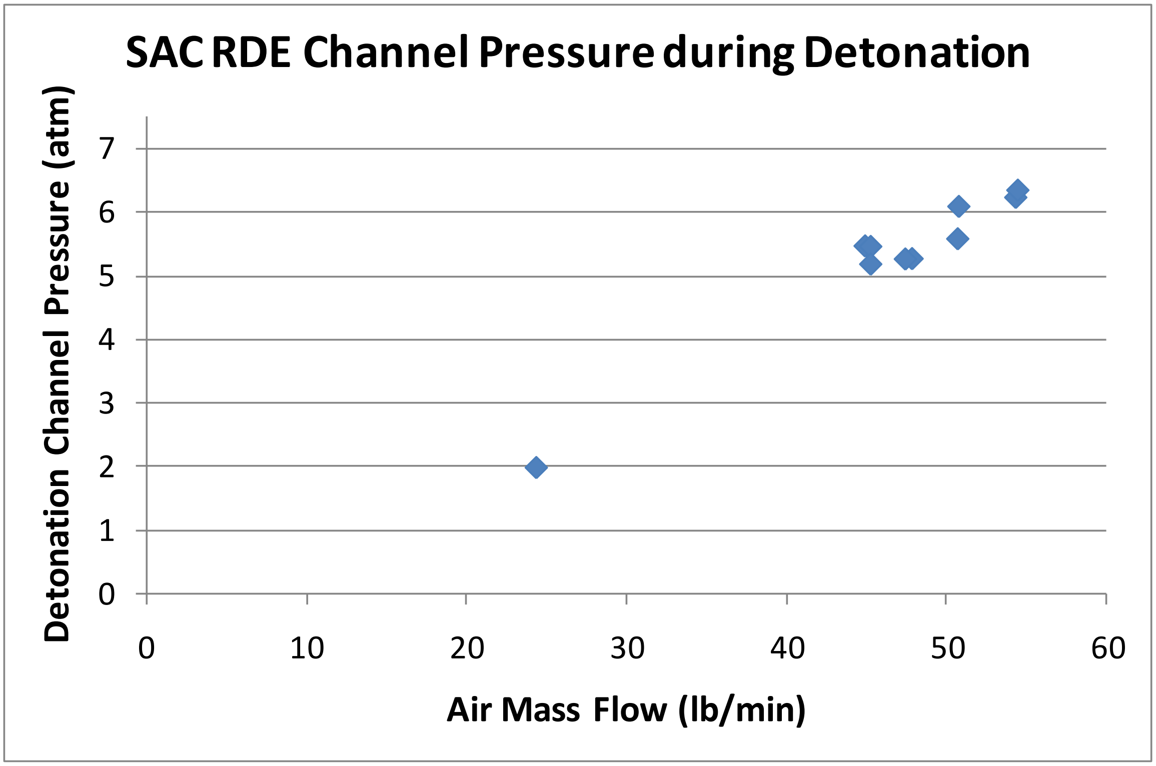

Figure 5.41: Relationship between the detonation channel pressure and the air mass flow into the engine

The channel pressure during the detonation combustion was subtracted from the channel pressure just prior to ignition in order to determine the pressure rise caused by the detonation. Unlike the baseline channel pressure discussed previously, the pressure rise caused by the detonation was an average of the channel pressure from 0.05 seconds after ignition to 0.05 seconds before shutdown minus the average pressure before ignition. This average pressure rise was used in order to determine how much axial pressure thrust could be generated by the engine based on the average pressure rise from the detonation and the axial area of the detonation channel. Since all of these tests were performed with an outer detonation channel diameter of 3 inches and a channel width of 6mm, the axial area of the detonation channel was 2.05 in^2.

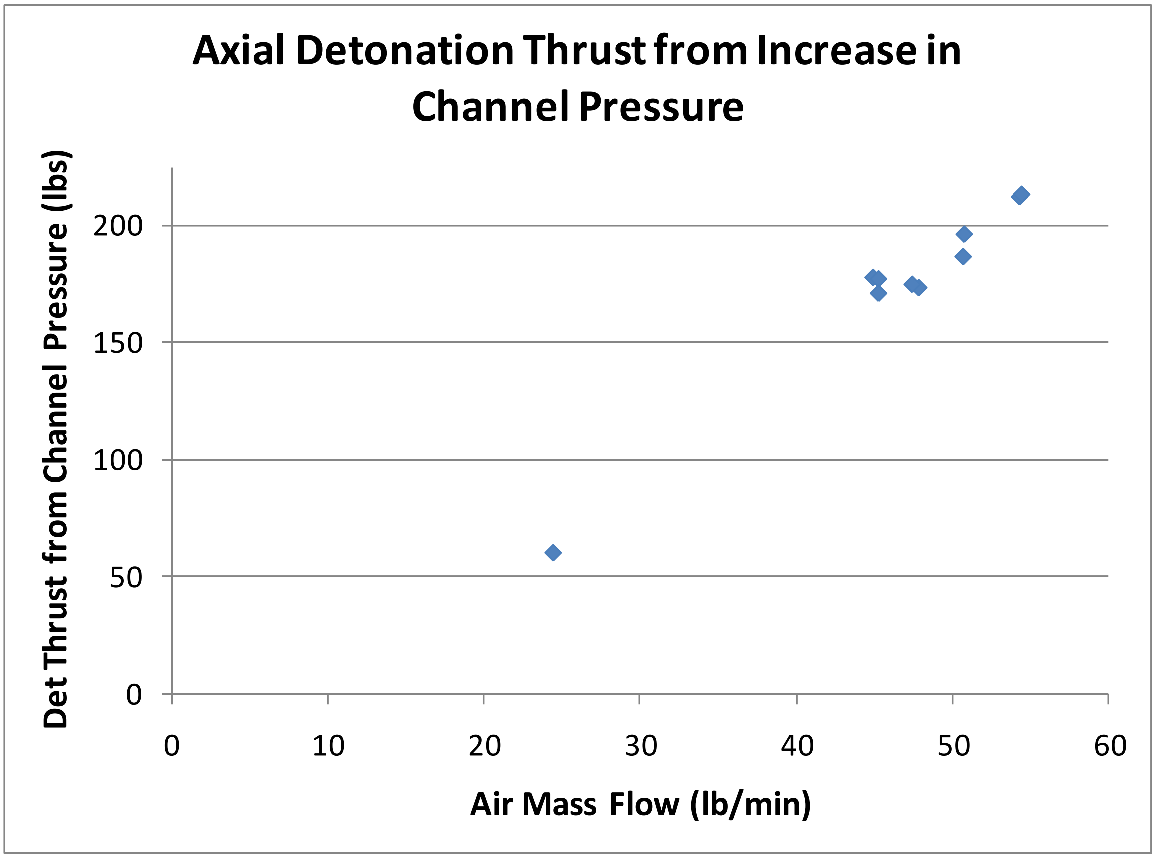

Figure 5.42: Axial detonation thrust as a function of air mass flow calculated from the average channel pressure rise from the detonation

This area was multiplied by the average rise in the channel pressure from the detonation in order to calculate the amount of available axial thrust generated by the detonation. The results of these calculations are shown in Figure 5.42. The results in Figure 5.42 show a much higher detonation thrust a given air mass flow than the previous experiments reported when the thrust was measured with a load cell.

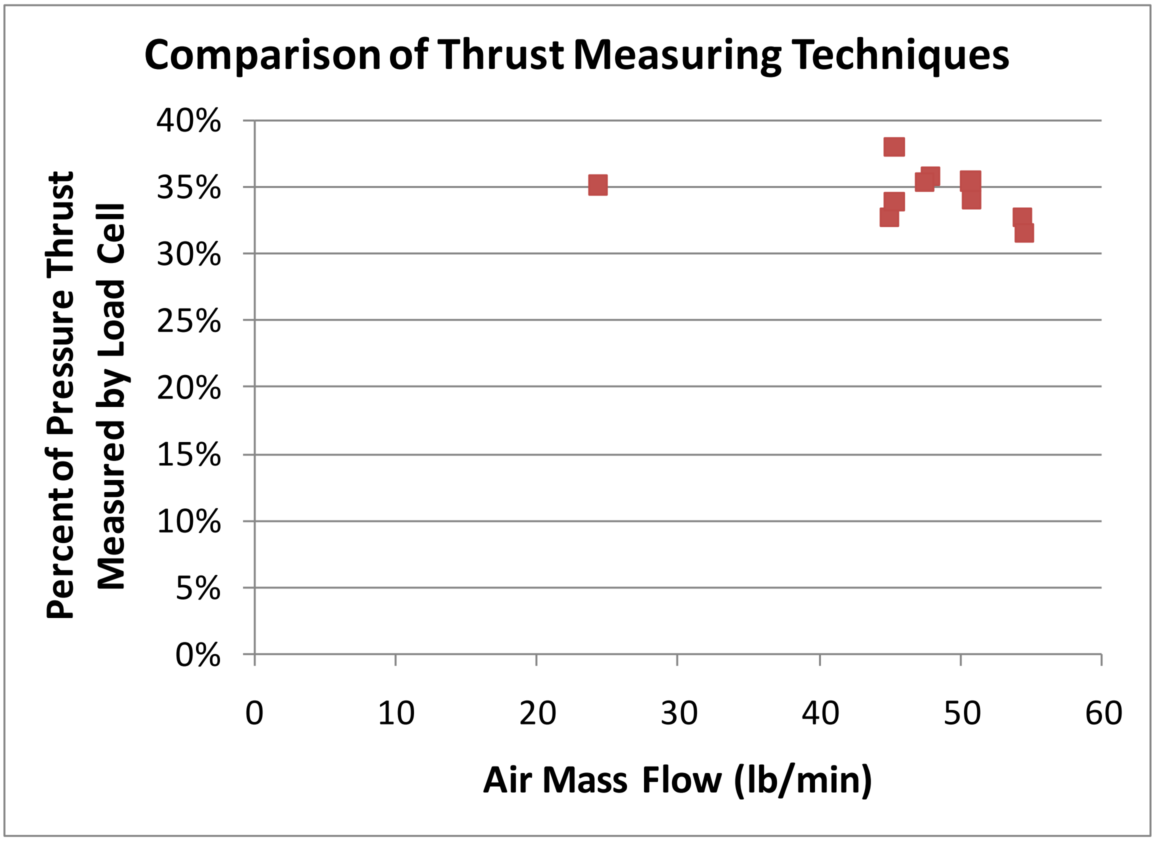

Figure 5.43: Comparison of the axial detonation thrust measured by the channel pressure and by the load cell

The thrust values obtained from the increase in average channel pressure were about three times greater than the increase in thrust detected by the load cell during detonation for these tests. The percentage of the thrust obtained from the channel pressure that was measured by the load cell as a function of air mass flow is shown in

Figure 5.43. The results of Figure 5.43 imply that the amount of thrust generated by the engine is not being fully measured by the load cell. One possible thrust loss mechanism is that some of the thrust is being used to deflect the supply lines to the engine instead of the diaphragm in the load cell, resulting in lower detonation thrust measurements, as well as the specific impulse and the specific thrust.

Chapter 6: Conclusions

6.1: Engine Operation

The tests performed on the engine showed that the best region of engine operation occurred in the rich operating regime, particularly at lower percentages of oxygen in the air. The addition of extra oxygen to the air had a great effect on the operating range of the engine, especially in the upper air mass flow limit. As the oxygen content in the air was increased, the engine was able to sustain detonations at much higher mass flows. The ability to detonate at greater air mass flows greatly increased the maximum thrust output of the engine as well.   These effects of greater oxygen content of the air on the upper air mass flow limit and the maximum thrust are summarized in Table 6.1.

	Percentage of Oxygen in Air, mole basis		
	21%	**23%**	**24.8%**
Maximum Thrust (lb)	50	65	>200
Upper Air Mass Flow Limit (lb/min)	40	50	130

Table 6.1: Upper air mass flow and maximum thrust produced from various oxidizers

Although the greatest detonable air mass flow and the maximum thrust were the operating parameters affected the most by the changes in the oxidizer, greater amounts of oxygen in the oxidizer also allowed the engine to detonate at lower air mass flow rates and leaner equivalence ratios. The increasing range of operation at lower air mass flow rates and leaner operation caused by the more reactive enriched air mixtures were apparent and significant, but paled in comparison to the effect on the upper air mass flow limit.

6.2: Engine Characterization

One of the measurements taken during RDE testing was the amount of thrust generated by the combustion wave inside of the engine. This thrust increased in a relatively linear trend with the air mass flow into the engine throughout the operating range of the RDE. This trend was consistent even when the velocity of the combustion wave was not high enough to be considered a detonation. The only tests that did not conform to this trend was the slight decrease in the thrust for air mass flows just below the onset of two detonation wave activity in the engine. Since the runs just prior to two wave activity were quite unstable, it is likely that the instability in the combustion caused the slight decrease in thrust output.

The gross thrust generated by the engine was used to determine the specific impulse. The numerous tests performed with the engine showed a consistent trend of greater specific impulse with leaner equivalence ratios. This trend held true for every engine configuration and oxidizer that was tested, although the specific impulse was greater for runs at higher air mass flows than runs at lower air mass flows at the same equivalence ratio. The specific impulse was as high as 4,033 s at an equivalence ratio of

0.92 and as low as 969 s at an equivalence ratio of 3.01. The thrust generated by the combustion was used to calculate the specific thrust, which had a similar trend as the thrust output of the engine. The specific thrust increased linearly with air mass flow for all of the steady runs with exclusively one detonation wave before leveling off during the unsteady exclusively one detonation wave runs just prior to the onset of two wave activity. Once the air mass flow was high enough to generate two detonation waves, the specific thrust reestablished a linearly increasing trend with air mass flow. The specific thrust was as high as 104 s at an air mass flow of 125 pounds per minute, and as low as 25 s at an air mass flow of 25 pounds per minute.

6.3: Detonation Characteristics

Lastly, the characteristics of the detonation wave itself were examined during testing. Two of the characteristics, the average velocity of the propagating combustion wave and the unsteadiness of the propagating combustion wave, had an inverse relationship. The greater the velocity of the combustion wave in the engine, the lower the unsteadiness of the combustion wave, and vice versa. This trend held true for all of the tests performed with the same operating mode. The one wave portions of the multimodal runs had a higher unsteadiness than the exclusively one wave runs at the same average combustion wave velocity. On the other hand, the two wave portions of the multimodal runs had a lower unsteadiness than the exclusively one wave runs at the same average combustion wave velocity. Although the values of velocity and unsteadiness varied between operating modes of the engine, the overall trend of an inverse relationship between average velocity and unsteadiness applied to all of the tests that were performed.

The transition between different operating modes of the engine was studied as well. As the engine was tested at greater and greater air mass flows with the more detonable mixture of hydrogen and air with 24.8% oxygen, the single detonation wave in the engine became less steady, and then began to split into two detonation waves during a portion of the run. As the air mass flow was increased further, the runs began to contain primarily two detonation waves. The instability of the predominant wave mode of the run grew as the air mass flow entered the transition region from one to two detonation waves, but then fell sharply after the engine began to operate with predominantly two detonation waves. The steadiness of the two detonation waves during predominantly two detonation wave runs was as steady as the steadiest exclusively one wave runs

The transition between exclusively one wave operation and primarily one wave operation with some two wave operation occurred between 102.3 and 102.8 pounds per minute of air mass flow, and the transition between primarily one wave operation with some two wave operation and primarily two wave operation occurred between 101.5 and 106.5 pounds per minute of air mass flow. In addition, all of the tests that were predominantly one wave runs contained less than 20% of two wave activity, while all of the test that were predominantly two wave runs contained more than 70% of two wave activity.

Another testing procedure that was performed was the pressure in the channel pressure prior to the ignition of the detonable mixture. The channel pressure showed a linear increase with air mass flow into the engine before a critical air mass flow between 45 and 50 pounds per minute caused the pressure to decrease by more than 50% on an absolute scale. However, this drop in pressure at ignition did not change the established trends of channel pressure during ignition and average velocity of the detonation wave. Since changes in the pressure of the channel at ignition did not have an effect on the established trends of channel pressure during the run and detonation wave speed as function of air mass flow, it appears that the properties of the detonation did not seem to be affected by the pressure in the channel at ignition.

After this channel pressure test, a Kulite pressure transducer was used to measure the pressure at a much higher frequency during the run in order to obtain the pressure of the channel when the detonation wave was propagating around the channel but was not in the immediate vicinity of the pressure transducer. The channel pressure during the detonation propagation increased linearly from 2 atmospheres at 24 pounds per minute of air mass flow to slightly greater than 6 atmospheres at 54 pounds per minute of air mass flow. The average pressure of the Kulite was also used to calculate the amount of thrust exerted axially on the engine. The thrust obtained from the load cell data was only 30-40% of the pressure thrust measured by the Kulite pressure transducer.

References

Anderson, J. D. Modern Compressible Flow: With Historical Perspective: McGraw-Hill, 2003.

Braun, E., Dunn, N., and Lu F., “Testing of a Continuous Detonation Wave Engine with Swirled Injection.” AIAA 2010-146, 48th AIAA Aerospace Sciences Meeting, Orlando, Florida 2010.

Bykovskii, F. A., Mitrofanov, V. V., and Vedernikov, E. F. "Continuous Detonation Combustion of Fuel-Air Mixtures." *Combustion, Explosion, and Shock Waves*, Volume 33, Number 3, 1997.

Bykovskii, F. A., Zhdan, S. A., and Vedernikov, E. F. "Continuous Spin Detonation of Fuel-Air Mixtures." *Combustion, Explosion, and Shock Waves*, Volume 42, Number 4, 2006, pp. 463-471.

Davidenko, Dmitry M., Eude, Y., Gokalp, I., and Falempin, F. "Theoretical and Numerical Studies on Continuous Detonation Wave Engines." AIAA Paper 2011-2334. Paper presented at the 17th AIAA International Space Planes and Hypersonic Technologies Conference, San Francisco, California 2011.

Dyer, R., Naples, A., Kaemming, T., Hoke, J., and Schauer, F. "Parametric Testing of a Unique Rotating Detonation Engine Design." AIAA Paper 2012-0121. Paper presented at the 50th AIAA Aerospace Sciences Meeting, Nashville, Tennessee 2012.

Falempin, F., and La Naour, B. "R&T Effort on Pulsed and Continuous Detonation Wave Engines." AIAA Paper 2009-7284. Paper presented at the 16th AIAA/DLR/DGLR International Space Planes and Hypersonic Systems and Technology Conference, Bremen, Germany 2009.

Figliola, Richard S. and Beasley, Donald E. *Theory and Design for Mechanical Measurements.* Fourth edition: John Wiley and Sons, Inc., 2006.

Flowmaxx Engineering. *Sonic Nozzles*. [cited October 18 2011]. Available from http://www.flowmaxx.com/sonic.htm.

Folusiak, M., Kobiera, A., and Wolanski, P. "Rotating Detonation Engine Simulations In-House Code - REFloPS." *Transactions of the Institute of Aviation*. May, 2010.

Glassman, Irvin and Richard Yetter. *Combustion*. Fourth edition: Academic Press, 2008.

Hayashi, A., Kimura, Y., Yamada, T., Yamada, E., Kindracki, J., Dzieminska, E., Wolanski, P., Tsuboi N., Tangirala, V., and Fujiwara, T. "Sensitivity Analysis of Rotating Detonation Engine with a Detailed Reaction Model." AIAA Paper 2009-0633. Paper presented at the 47th AIAA Aerospace Sciences Meeting, Orlando, Florida 2009.

Hishinda, M., Fujiwara, T., and Wolanski, P. "Fundamentals of rotating detonations." *Shock Waves*, Volume 19, 2009, pp. 1-12.

Honeywell International Inc. *Precision Low Profile Load Cell.* [cited October 25 2011]. Available from https://measurementsensors.honeywell.com/ProductDocuments /Load/Model_41_Datasheet.pdf.

Kailasanath, K. "Review of Propulsion Applications of Detonation Waves." AIAA Journal, Volume 38, Number 9, September 2000.

Kailasanath, K. "The Rotating-Detonation-Wave Engine Concept: A Brief Status report." AIAA Paper 2011-580. Paper presented at the 49th AIAA Aerospace Sciences Meeting, Orlando, Florida 2011.

Kindracki, J., Wolanski, P., and Gut, Z. "Experimental research on the rotating detonation in gaseous fuels-oxygen mixtures." *Shock Waves*, Volume 21, 2011, pp.75-84.

Kuo, K. K. Principles of Combustion: Wiley-Interscience, 1986.

Liu, Shi-Jie, Lin, Zhi-Yong, Sun, Ming-Bo, and Liu, Wei-Dong, “Thrust Vectoring of a Continuous Rotating Detonation Engine by Changing the Local Injection Pressure,” *Chinese Physical Society*, Volume 28, Number 9, 094704 (2011).

Omega Engineering, Inc. *High Performance Pressure Transmitter, PX309/PX319/PX329/PX359 4 to 20 mA Output Series.* [cited October 24 2011]. Available from http://www.omega.com/ppt/pptsc.asp?ref=PX309_mA&nav=.

Schauer, F., J. Stutrud, and R. Bradley. "Detonation Initiation Studies and Performance Results for Pulsed Detonation Engine Applications." AIAA Paper 2001-1129. Paper presented at the 39th AIAA Aerospace Sciences Meeting and Exhibit, Reno, Nevada 2001.

Schwer, Douglas A. and Kailasanath, Kalias. "Feedback into Mixture Plenums in Rotating Detonation Engines." AIAA Paper 2012-0617. Paper presented at the 50th AIAA Aerospace Sciences Meeting, Nashville, Tennessee 2012.

Shank, J., King, P., Karnesky, J., Schauer, F., and Hoke, J. "Development and Testing of a Modular Rotating Detonation Engine." AIAA Paper 2012-0120. Paper presented at the 50th AIAA Aerospace Sciences Meeting, Nashville, Tennessee 2012.

Shao, Y. T., Liu, M., and Wang, J. P. “Numerical Investigation of Rotating Detonation Engine Propulsive Performance.” *Combustion Science and Technology*, Volume 182, 2010, pp. 1586–1597.

Shao, Y. T., Liu, M., and Wang, J. P. “Continuous Detonation Engine and Effects of Different Types of Nozzle on its Propulsion Performance.” *Chinese Journal of Aeronautics*, Volume 23, 2010, pp. 647-652.

Shepherd, J., Personal Communication, California Institute of Technology, 24 August 2000.

Suchocki, J., Yu, T-S., Hoke, J., Naples, A., Schauer, F., and Russo, R. "Rotating Detonation Engine Operation." AIAA Paper 2012-0119. Paper presented at the 50th AIAA Aerospace Sciences Meeting, Nashville, Tennessee 2012.

Turns, Stephen R. *An Introduction to Combustion: Concepts and Applications*. Second edition: McGraw-Hill High Education, 2006.

Wolanski, Piotr. “Rotating Detonation Wave Stability.” 23rd ICDERS, Irvine, California 2011.

Yamada, T., Hayashi, A., Yamada, E., Tsuboi, N., Tangirala, V., and Fujiwara, T. "Numerical Analysis of Threshold of Limit Detonation in Rotating Detonation Engine." AIAA Paper 2010-153. Paper presented at the 48th AIAA Aerospace Sciences Meeting, Orlando, Florida 2010.

Yi, T., Turangan, C., Lou, J., Wolanski, P., and Kindracki, J. "A Three-Dimensional Numerical Study of Rotating Detonation in an Annular Chamber." AIAA Paper 2009-634. Paper presented at the 47th AIAA Aerospace Sciences Meeting, Orlando, Florida 2009.

Yi, T., Lou, J., Turangan, C., Khoo, B., and Wolanski, P. "Effect of Nozzle Shapes on the Performance of Continuously Rotating Detonation Engine." AIAA Paper 2010-152. Paper presented at the 48th AIAA Aerospace Sciences Meeting, Orlando, Florida 2010.